ELSEVIER

Contents lists available at ScienceDirect

Earth-Science Reviews

journal homepage: www.elsevier.com/locate/earscirev





Tsunami excitation in the outer wedge of global subduction zones

Qiang Qiu a,b,c,d,*, Sylvain Barbot b

- ^a Key Laboratory of Ocean and Marginal Sea Geology, South China Sea Institute of Oceanology, Innovation Academy of South China Sea Ecology and Environmental Engineering, Chinese Academy of Sciences, Guangzhou 510301, China
- b Department of Earth Sciences, University of Southern California, USA
- ^c China-Pakistan Joint Research Center on Earth Sciences, CAS-HEC, Islamabad 45320. Pakistan
- ^d Southern Marine Science and Engineering Guangdong Laboratory, 511458 Guangzhou, China

ARTICLE INFO

Keywords: Subduction margins Accretionary prism Fold and thrust belt Tsunami excitation Shallow subduction earthquake

ABSTRACT

The world's most devastating local and ocean-wide tsunamis are generated by subduction zone earthquakes, but the mechanisms for powerful seafloor uplift and tsunami generation during seismic rupture propagation remain poorly understood. In particular, great earthquakes near the trench can generate outsize tsunamis that rival those produced by giant trench-breaking ruptures. Solving this conundrum is key to better assessing seismic and tsunami hazards at subduction zones. Here, we inspect high-resolution bathymetry, seismic reflection profiles, and tsunami-earthquake rupture models at global subduction zones to identify the structural control on tsunami excitation by coseismic seafloor uplift. We find that tsunami run-ups of trench-breaking ruptures correlate with the width of the outer wedge of the frontal accretionary prism, which consists of active imbricate or conjugate faults above the shallow megathrust. The prevalence of high-angle faults in the outer wedge provides the mechanism for more efficient seafloor uplift and thus tsunami wave excitation than coseismic slip on the shallow décollement. We calibrate a power-law relationship with outer-wedge width and seismic moment to estimate the maximum tsunami run-up along major subduction zones. The tsunami excitation potential is among the highest at the northern Sumatra (Indonesia), Hikurangi (New Zealand), and western Makran (Iran) accretionary margins, and the lowest at the Costa Rica and Valdivia (Chile) erosive margins. The structural control of tsunami excitation is important to characterize the rupture style and tsunami magnitude of future seismicity at subduction zones, offering crucial information for seismic and tsunami hazard preparedness and rapid run-up assessment during the early-warning stage, especially at well-identified seismic gaps.

1. Introduction

The recycling of oceanic plates at subduction zones is a key part of plate tectonics, enabling many geochemical cycles that make our planet inhabitable. The subduction of oceanic material occurs at a shallow angle in the lithosphere and is resisted by frictional forces. The wide area offered by subduction megathrusts releases more than 90% of global seismicity and powers Earth's largest earthquakes and tsunamis (Fig. 1a and Table S1). The Rim of Fire, which extends around the Pacific Rim to the Java-Sumatran arc in Southeast Asia, produced many of the largest earthquakes and tsunamis of the past century, including the 1960 moment magnitude (Mw) 9.5 Valdivia, Chile and the 1964 Mw 9.2 Alaska giant earthquakes. Seismically triggered tsunami waves cause great loss of life and property and have been described as the scourge of

the Pacific [Lockridge, 1985].

After several decades of relative quiescence, giant earthquakes reoccurred in the 21st century with the 2004 Mw 9.2 Sumatra-Andaman earthquake on the Sunda megathrust [Chlieh et al., 2007; Ammon et al., 2005; Lay et al., 2005], the 2010 Mw 8.7 Maule earthquake at the Chilean subduction zone [Moreno et al., 2010; Weiss et al., 2019], and the 2011 Mw 9.1 Tohoku-Oki megaquake along the Japan Trench [Lay and Kanamori, 2011; Wei et al., 2012; Simons et al., 2011]. More great and giant earthquakes are expected at many remaining seismic gaps of global subduction zones [McCann et al., 1979; Heaton and Kanamori, 1984; Thatcher, 1989] or at their boundary [Herman and Furlong, 2021] and they will be almost certainly be accompanied by transoceanic tsunami waves. Understanding the relationship between seismicity and tsunami-genesis is a major challenge in tectonophysics

^{*} Corresponding author at: Key Laboratory of Ocean and Marginal Sea Geology, South China Sea Institute of Oceanology, Innovation Academy of South China Sea Ecology and Environmental Engineering, Chinese Academy of Sciences, Guangzhou 510301, China.

E-mail address: qiu.qiang@scsio.ac.cn (Q. Qiu).

[Satake and Tanioka, 1999; Polet and Kanamori, 2000; Geersen, 2019]. This is exemplified by the conundrum of tsunami earthquakes that occur close to the trench and generate tsunami waves comparable to that of larger-magnitude earthquakes [Kanamori, 1972; Kanamori and Kikuchi, 1993; Kanamori et al., 2010]. Tsunami earthquakes have occurred in many sections of the Pacific Rim (Fig. 1a and Table S1) and represent a major category of subduction seismicity. Current models of subduction

seismicity suggest a depth-dependent rupture behavior controlled by chemical and geothermal gradients and structural boundaries [e.g., Hyndman et al., 1997; Song and Simons, 2003; Lay et al., 2012; Obara and Kato, 2016; Gao and Wang, 2017; Bilek and Lay, 2018; Shi et al., 2020; Barbot, 2020]. The seismogenic zone underlies the inner wedge and the arc or continental crust, bounded by the 100 and 350°C isotherms of unstable friction for quartz-rich gouge [Blanpied et al., 1991,

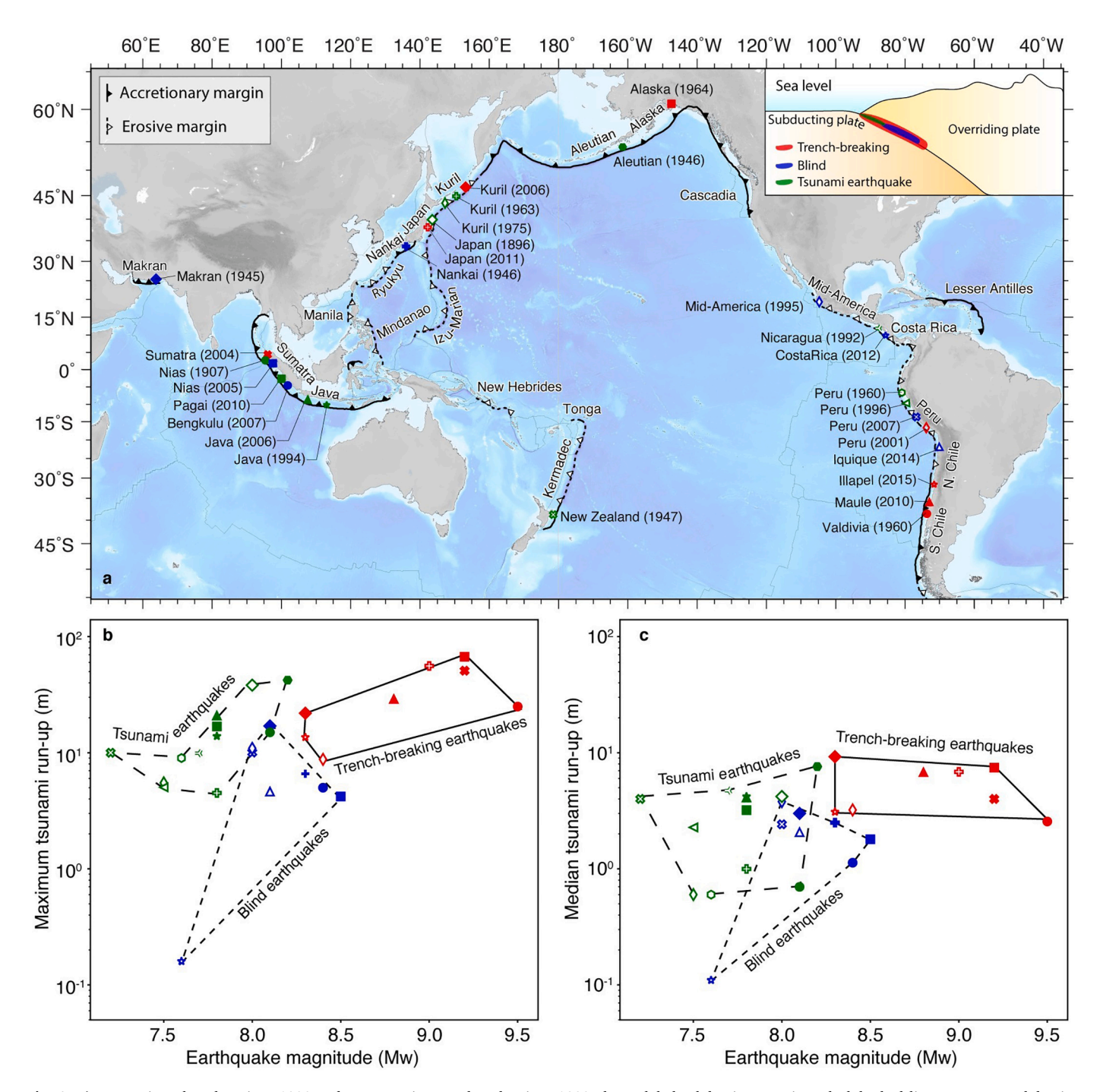


Fig. 1. a) Tsunami earthquakes since 1800 and great or giant earthquake since 1900 along global subduction margins. Black-barbed lines represent subducting boundaries (solid-accretionary; broken-erosive). Colored symbols show hypocenter location of each earthquake from the USGS catalog, with tsunami earthquakes (green), blind earthquakes (blue) and trenchbreaking ruptures (red), defined in the inset. Open symbols show events at erosive margins.

b) Maximum tsunami run-up measurements against seismic moment magnitude generated by tsunami earthquakes (green), blind ruptures (blue) and great or giant trench-breaking earthquakes (red). The colored symbols are the same as in a). c) Same as b) but for the median tsunami run-up. The global tsunami run-up dataset is from NOAA (National Geophysical Data Center / World Data Service: NCEI/WDS Global Historical Tsunami Database. NOAA National Centers for Environmental Information. doi:https://doi.org/10.7289/V5PN93H7 [access date on 18 June 2020]). See also Table S1. (For interpretation of the references to colour in this figure legend, the reader is referred to the web version of this article.)

1995; Scholz, 1998]. Long-term and short-term slow-slip events, whether or not associated with low-frequency earthquakes and tremors, occur in stable-weakening regions promoted by regional metamorphism, high temperature, and the presence of fluids [Bürgmann, 2018; Behr and Bürgmann, 2021; Condit et al., 2020; Kirkpatrick et al., 2021]. The brittle-ductile transition occurs below the cold nose, underneath the volcanic arc when it exists [Wada and Wang, 2009; Qiu et al., 2018; Weiss et al., 2019; Barbot, 2020; Luo and Wang, 2021]. The seismogenic and tsunamigenic potentials of the megathrust underneath the shallow accretionary prism is less well understood. Observations of trench-breaking slip during the 2004 Sumatra-Andaman [e.g., Singh

et al., 2008; Dean et al., 2010; Hüpers et al., 2017] and the 2011 Tohoku-Oki [Fujiwara et al., 2011; Ito et al., 2011; Kido et al., 2011; Kodaira et al., 2012] earthquakes, of shallow slow-slip events [Wallace et al., 2016; Todd et al., 2018; Saffer and Wallace, 2015; Araki et al., 2017] and low-frequency earthquakes [Ito and Obara, 2006; Obana and Kodaira, 2009; Nakano et al., 2018], and of tsunami earthquakes, provide direct evidence for unstable fault slip near the trench. The relative scarcity of shallow megathrust seismicity may be explained by distributed deformation in the thrust-and-fold belt of the outer wedge [Li et al., 2015; Sathiakumar et al., 2020; Shi et al., 2020] or by the complex evolution of the frictional properties of the overlying sediment, mostly

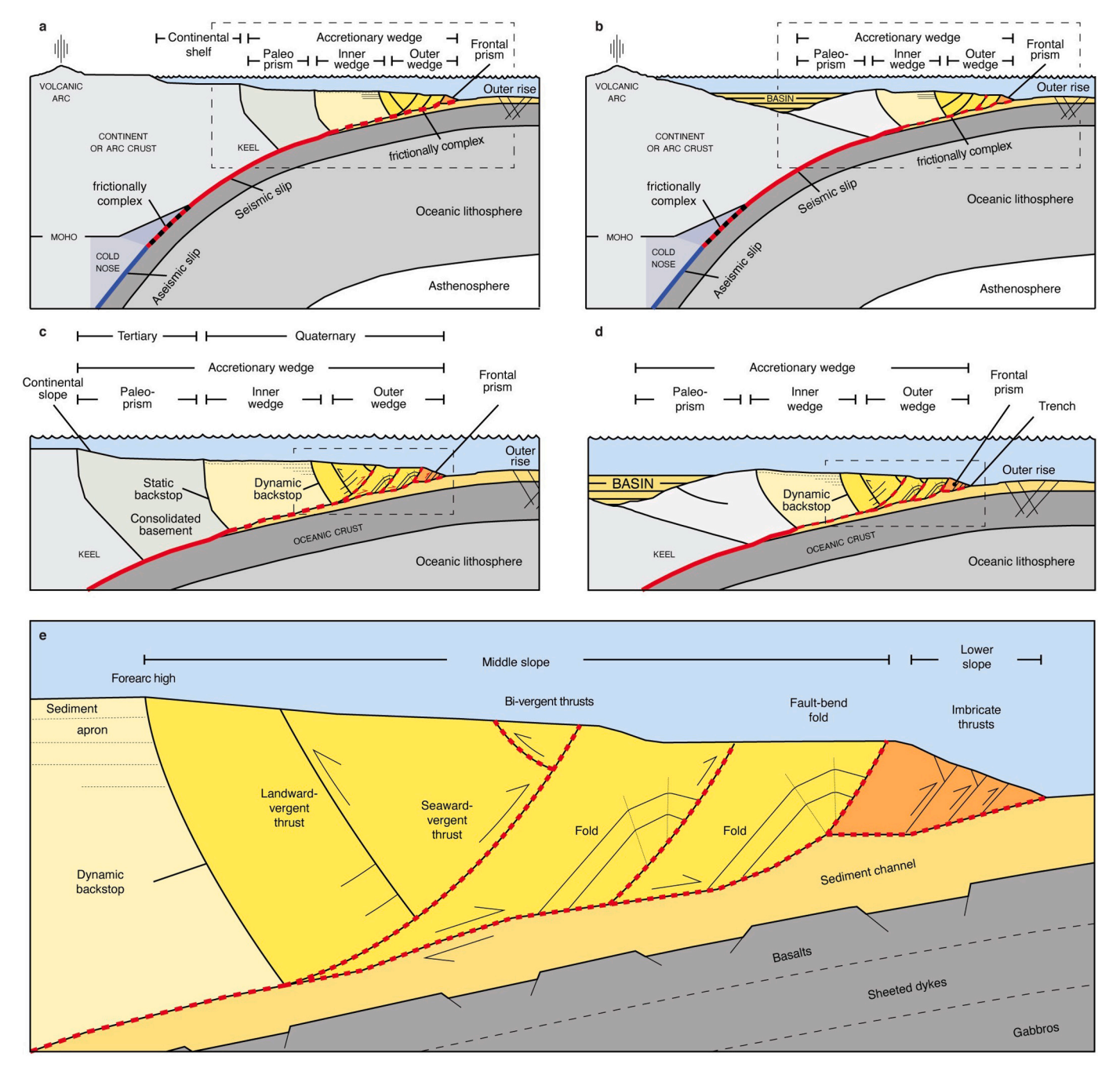


Fig. 2. Anatomy of a subduction zone in cross-section. a) Typical cross section of ocean-continent subduction zone with the accretionary prism abutting the continental shelf. The seismogenic zone extends from the paleo-prism to the top of the cold nose. The frictional properties of the inner- and outer-wedge is more complex and non-stationary. b) Typical cross-section for the Sunda and Java subduction zones, with a large basin separating the accretionary prism from the continent or arc crust. c) Accretionary prism decomposed into the paleo-, inner-, and outer-wedge. d) Similar section for the Sunda and Java subduction zones. e) Typical structure of the outer wedge from a forearc high to the trench, with landward- and seaward-vergent thrusts and folds.

clay [Brantut et al., 2008; Ujiie and Tsutsumi, 2010; Tsutsumi et al., 2011; Ikari and Kopf, 2017; Aretusini et al., 2021]. Several mechanisms have been proposed to explain large shallow slip on the décollement during trench-breaking ruptures, including thermal pressurization [Sibson, 1977; Wibberley and Shimamoto, 2005; Ishikawa et al., 2008; Noda and Lapusta, 2013], hydraulic lubrication [Brodsky and Kanamori, 2001; Di Toro et al., 2006], frictional heating [Hirono et al., 2008; Tanaka et al., 2006], and flash weakening [Beeler et al., 2008; Rice, 2006], but an explanation for the elevated tsunami potential of shallow ruptures is still elusive.

Various source mechanisms can be invoked to explain extreme tsunami wave heights. Efficient seafloor uplift can be explained by inelastic deformation within the outer wedge [Ma and Hirakawa, 2013; Kozdon and Dunham, 2014; Lotto et al., 2017; Ma and Nie, 2019], enhanced deformation due to low rigidity of the frontal wedge [Bilek and Lay, 1999; Polet and Kanamori, 2000; Sallares and Ranero, 2019], submarine slump failure [Kanamori and Kikuchi, 1993; Ward, 2001], hanging wall plasticity [Seno, 2000; Tanioka and Seno, 2001; Hill et al., 2012], structural control from seafloor roughness at sediment-starved trenches [Polet and Kanamori, 2000; Geersen, 2019], or exceptionally large shallow megathrust slip [Satake and Tanioka, 1999; Satake et al., 2017; Lay et al., 2011b]. Despite this progress, a simple explanatory framework for the generation of earthquakes and exceptionally large tsunamis at the shallow portion of subduction zones is still missing.

To shed new light on the problem, we draw insights from a global catalog of run-up of seismically triggered tsunamis comprising a wide range of tectonic settings spanning different plate age, geometry, convergence rates, and sediment fluxes (Fig. 1b). The distribution of maximum and median tsunami run-up as a function of earthquake magnitude can be grouped into three earthquakes categories based solely on the location and extent of the rupture: First, the blind ruptures that do not extend to the trench, e.g., the 2005 Mw 8.6 Nias-Simeulue and the 2014 Mw 8.1 Iquique events, and that generate only moderate or minor tsunami waves; second, the trench-breaking ruptures of great and giant earthquakes that generate substantial tsunamis; and third, the tsunami earthquakes that are confined to the frontal portion of the accretionary prism and break to the trench, which generate similar-sized tsunamis to that of category-two events. These results highlight that tsunami-genesis is not only controlled by earthquake size, but also by the proximity of earthquake ruptures to the trench and the structural fabric of the hanging wall.

Seismic imaging of active margins over the past decades has increased our understanding of the structure and mechanical properties of accretionary wedges (Fig. 2), illuminating at least three mechanically distinct segments [von Huene et al., 2009; Wang et al., 2006; Wang and Hu, 2006; Kimura et al., 2007; Wang et al., 2010; Watt and Brothers, 2020]. The actively deforming outer wedge is a thrust-and-fold belt, characterized by the presence of numerous parallel or conjugate faults overlain by folds, that sits under steep seafloor topographic slopes [Mandal et al., 1997; Seno, 2000; Wang et al., 2006; Singh et al., 2008; Kopp et al., 2009; Kamei et al., 2012; Zhu et al., 2013]. The outer wedge includes a frontal prism near the trench, which is often the most intensely deforming segment. The inner wedge encompasses a thicker pile of sediment under mild seafloor slopes and undergoes little internal deformation contemporaneously. The basal layer of the inner wedge includes more lithified sediment due to higher temperature and pressure. The third offshore segment of subduction margins lies under the continental or arc shelf or under forearc basins and represents the frontal keel of the crust from the overriding plate. The inner and outer wedges are separated by a dynamic backstop while a static backstop bounds the inner wedge and the continental or arc crust [Watt and Brothers, 2020]. In this study, we argue that tsunami-genesis is largely controlled by the overlap of seismic ruptures with the outer wedge of the accretionary prism (Fig. 2e). The high-angle splay faults of the outer wedge provide an efficient mechanism to transfer sub-horizontal slip on the megathrust to seafloor uplift and tsunami excitation. The down-dip width of the

outer wedge controls the number of splay faults involved during rupture, individual fault slip, and the resulting coseismic seafloor uplift.

To investigate the structural control of tsunami excitation, we review multiple geophysical, seismo-geodetic, and high-resolution bathymetric datasets. We delineate the inner and outer wedges of accretionary prisms by interpretation of seismic horizons in vertical cross-sections and by mapping surface faults and folds. In the following section, we analyze the morphology surrounding the rupture areas of historical and more recent tsunami earthquakes. We find that the rupture width, moment magnitude, and tsunami run-up of tsunami earthquakes are positively correlated with the width of the outer wedge. This relationship allows us to discuss tsunami hazards at other subduction zones based on morphological data. In a subsequent section, we calibrate an empirical model of maximum tsunami run-up of trench-breaking ruptures based on the width of the outer wedge and the earthquake moment magnitude using data from historical great and giant earthquakes. We conclude by making predictions of maximum tsunami run-up for hypothesized trench-breaking ruptures at global subduction zones based on the morphology of the outer wedge. Our model indicates the highest tsunami run-up for tsunami earthquakes at the Western Makran (Iran), Western Aleutian, Lesser Antilles, Hikurangi (New Zealand), and Cascadia subduction zones, although there is notable trench-parallel variability. Detailed seismic imaging of the outer wedge at megathrust seismic gaps will be key to better mitigate the tsunami risks induced by subduction seismicity.

2. Relationship between tsunami earthquakes and the outer wedge

We start by describing the structural setting of well-documented tsunami earthquakes to delineate their relationship with the outer wedge. We assemble high-resolution bathymetric data and multichannel seismic profiles and use slip distribution models to constrain the rupture location. The bathymetric data is from high-resolution multi-beam surveys or coarser datasets [Ryan et al., 2009]. For each case, we consider several bathymetric and topographic profiles going through the maximum coseismic slip region and we identify a representative trench-perpendicular seismic profile that may be offset along strike from the rupture area in some cases. Considering the bathymetry and the subsurface horizons, we map the faults and folds in the accretionary prism. For each case, we define the outer wedge in the accretionary prism as the region spanning from the trench to a bathymetric slope break or outer ridge that encompasses multiple active faults and folds above the megathrust (e.g., Fig. 3). In the following subsections, we present our seismic and structural analyses for each subduction margin where a tsunami earthquake occurred. We start the analysis in Northern Sumatra, Mentawai, and Java in Southeast Asia. We then examine events around the Pacific Ocean, starting in New Zealand, Northern Japan, Kuril, and the Aleutian, continuing with the Nicaragua and Peru subduction zones (Fig. 1a).

2.1. 1907 Mw 7.8 Nias tsunami earthquake at the Sunda Trench

On January 4, 1907, the Simeulue and Nias Islands were rattled by a shallow megathrust rupture with a surface wave magnitude (Ms) between 7.5 and 8.0. The rupture triggered a tsunami with a 20 m maximum tsunami run-up that killed hundreds of people [Kanamori et al., 2010; Martin et al., 2019]. The shaking came from two ruptures separated by an hour that generated different levels of ground shaking. The first event to the south was characterized by low levels of ground shaking, which is typical for a tsunami earthquake. The later Ms. 7 event to the north was responsible for the strong shaking on the Nias island [Martin et al., 2019]. Similar slow and fast two-stages ruptures have also been reported in the 2006 Java [Fan et al., 2017] and the 1963 and 1975 Kuril tsunami earthquakes [Fukao, 1979]. Combining the near- and farfield tsunami observations with forward tsunami modeling, Martin et al.

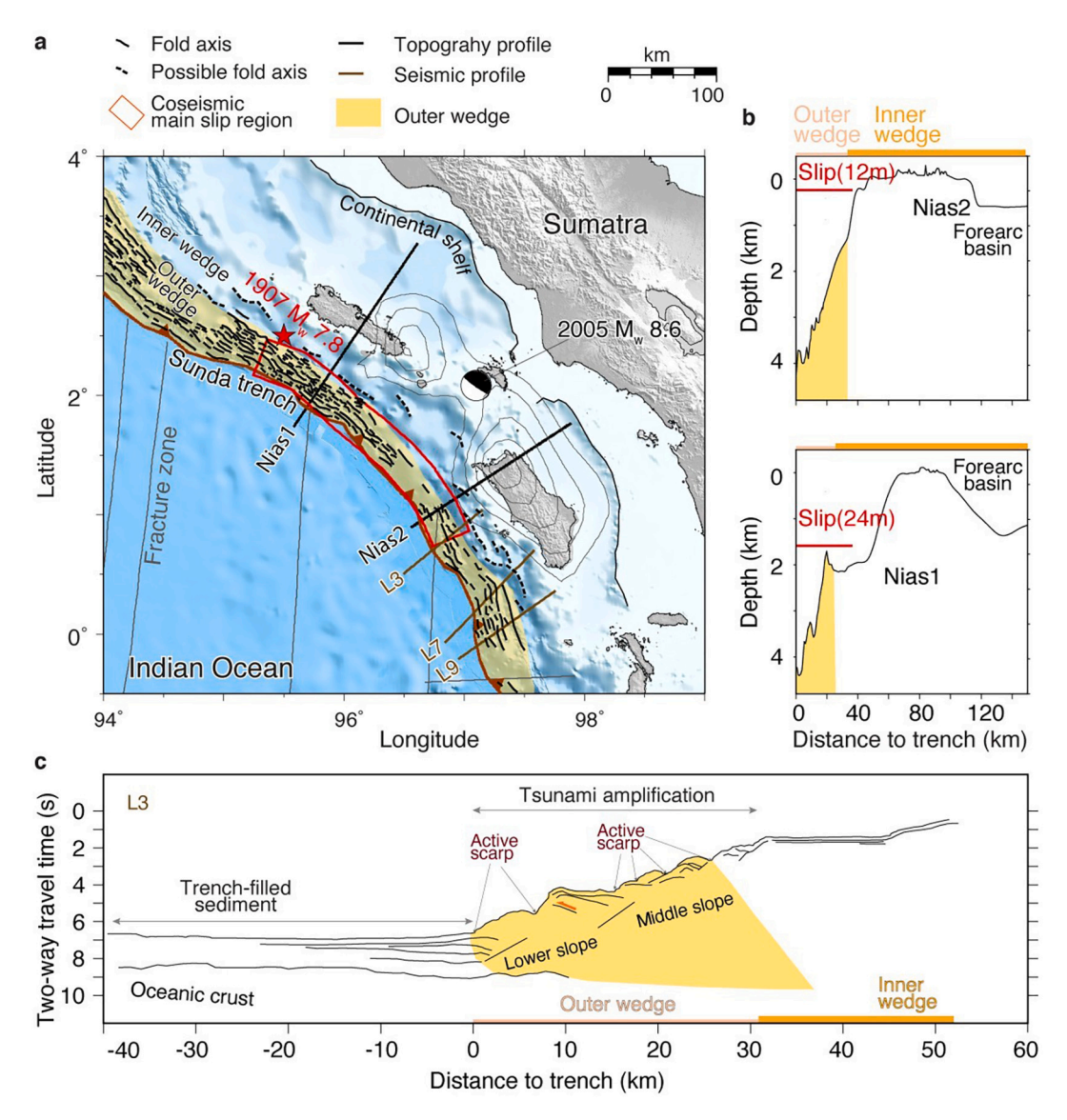


Fig. 3. Structural and tectonic setting of the 1907 Mw 7.8 Nias tsunami earthquake, Sumatra, Indonesia. a) Slip distribution of the 2005 Mw 8.6 Simeulue-Nias earthquake (black contours) [Hsu et al., 2006] and location of seismic profiles. Scarps and fold axes (bold black lines, broken if more uncertain) are highlighted in the map. The dark-red barbed line represents trench axis. The red contour delineates the estimated 1907 Mw 8.2 effective rupture patch from Martin et al. [2019]. b) Bathymetry along profiles Nias1 and Nias2 outlined in a). The red horizontal bars show the estimated slip within the outer wedge [Martin et al., 2019]. c) Interpretation of representative seismic profile L3 Moore and Curray [1980] showing the outer wedge in relation to the lower and middle slopes. Additional profiles for the Nias region include L7 and L9 [Moore and Curray, 1980]. Figs. 3-11 follow the same layout. (For interpretation of the references to colour in this figure legend, the reader is referred to the web version of this article.)

[2019] estimated a \sim 220 km rupture extending along the shallow Sunda megathrust with \sim 21 m of maximum slip offshore the Simeulue and Nias islands (Fig. 3).

The Sunda-Andaman Trench that delineates the boundary between the India-Australian plate and the Sunda peninsula of the Eurasian plate is an accretionary margin [Clift and Vannucchi, 2004] accumulating thick sediment from the Bengal Fan, a sink of Himalayan erosion. Along the northern half of the Sunda Trench, these sediments form a wide accretionary prism characterized by a plateau separating a forearc basin from the frontal section. Among various seismic profiles available in the region [e.g., Dean et al., 2010; Moore and Curray, 1980; Singh et al., 2008], the one from Moore and Curray [1980] may be the most representative of the Nias section. The seismic profile reveals the horizontal bedding planes of incoming sediment followed by accretion and underplating within the accretionary prism. Near the frontal prism, the tilted seismic horizons and fault scarps suggest active deformation. The outer wedge can be recognized from its steep slopes, fault scarps, and

internal deformation. The inner boundary of the outer wedge is marked by a slope break bounding the virtually undisturbed sub-horizontal sediment layers of the inner wedge. Considering these structural boundaries, we estimate an outer wedge horizontal width of 30 km.

The high-slip region of the 1907 tsunami earthquake overlaps with many surficial ridges and fold axes, and is largely confined within the outer wedge (Fig. 3). The location of the rupture suggests that some internal structures of the outer wedge may be involved with the anomalously large tsunami waves. The maximum slip region offshore Simeulue Island to the north is associated with a much denser and wider distribution of ridges and fold axes than that of the first, more moderate slip region to the south. The strong shaking of the second event in the 1907 tsunami earthquake sequence may have been caused by the activation of more splay faults within the outer wedge. These observations suggest that the structure of the outer wedge exerted some control on tsunami excitation during the 1907 tsunami earthquake doublet.

2.2. 2010 Mw 7.8 Mentawai tsunami earthquake at the Sunda Trench

Farther south along the Sunda megathrust, a tsunami earthquake ruptured the shallowest section of the megathrust on October 25, 2010 offshore Pagai (Fig. 4). The 2010 Mw 7.8 Mentawai earthquake was characterized by a very slow (1~1.5 km/s) and long-duration (100~150 s) rupture depleted in high-frequency seismic radiation [Lay et al., 2011a; Yue et al., 2014]. The rupture generated an anomalously large tsunami with >16 m of maximum run-up that claimed 509 deaths on the Pagai Islands [Hill et al., 2012]. Seismo-geodetic models place large coseismic slip (about 8 m) close to the trench [Yue et al., 2014; Hill et al., 2012; Li et al., 2016]. The rupture generated a localized tsunami wave that was reported mainly on Pagai and Sipora Islands, with a maximum tsunami runup >16 m reported on Sibigau Island, offshore the southern Pagai Island [Hill et al., 2012].

Moderate and minor tsunamis were also reported on the Mentawai Islands, Sumatra, and other parts of the Indian Ocean.

The morphology of the Sunda Trench varies along strike with a major

structural boundary at the Investigator Fracture Zone, where a fossil ridge is subducting obliquely. The fossil ridge is a topographic high that impedes sediment transport farther south [Whittaker et al., 2013; Pasyanos et al., 2014]. North of this basin boundary, the sediment pileup above the oceanic crust is about 1.5 km thick or higher. Southeast of 98°, the sediment thickness drops to half a kilometer, affecting the sediment flux on the Sunda Trench. The high-quality seismic profile CGGV020 [Hananto et al., 2020] that crosses the rupture area of the 2010 Mw 7.8 Mentawai tsunami earthquake reveals a severely deformed outer wedge with numerous faults, folds, and high-angle splay faults branching from the megathrust, forming shallow pop-up structures, i.e., bi-vergent thrusts (Fig. 4c). Considering the bathymetric change of slope bounded by an outer arc high, the density of surface fold axes, and the seismically imaged internal deformation, we estimate an outer-wedge horizontal width of 35 km. As the large coseismic slip of 8 m on the shallow megathrust is not sufficient to generate the tsunami run-up observed on Pagai Island [Hananto et al., 2020], the uplift of extra volume of water close to the trench from plastic deformation was

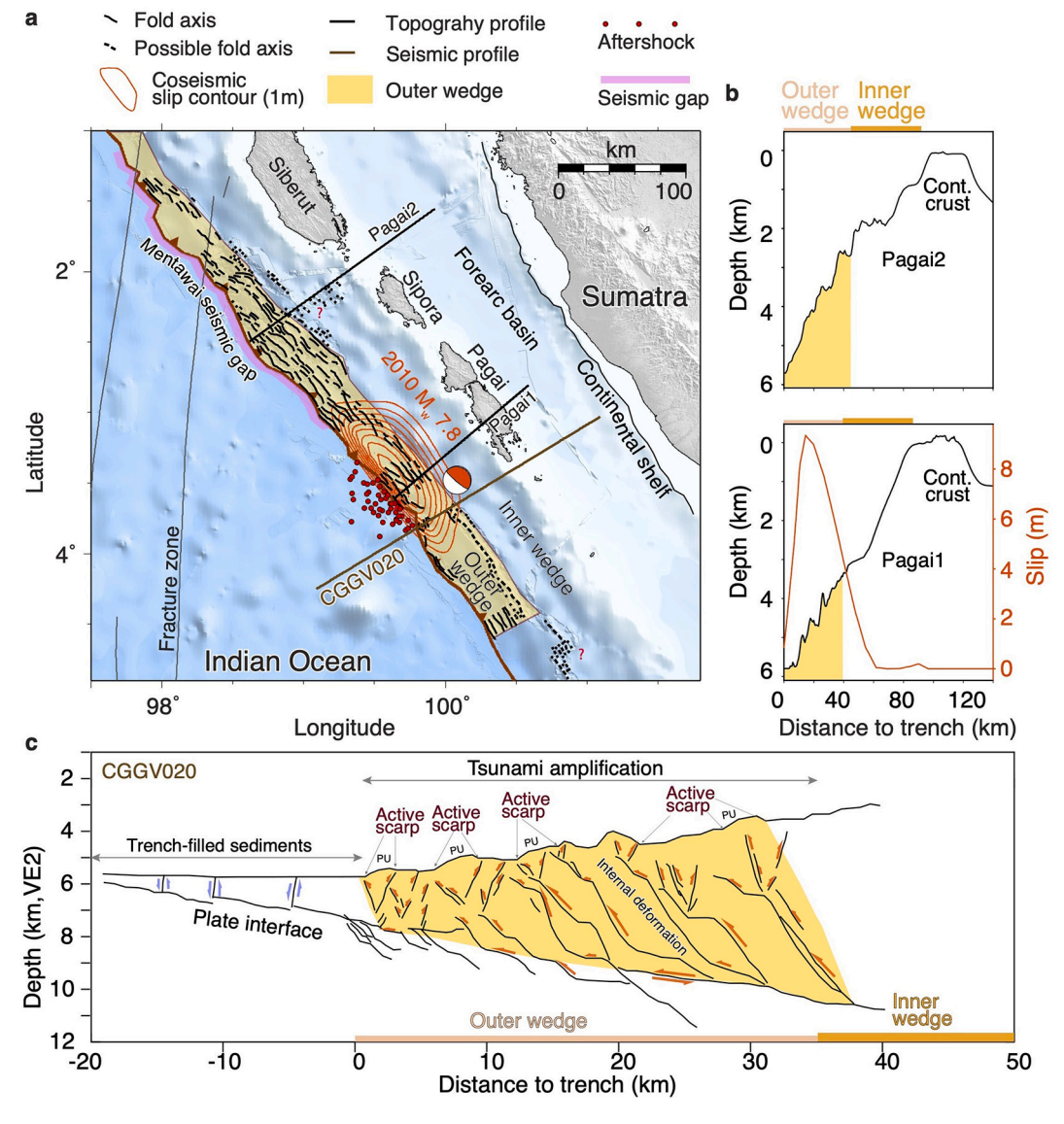


Fig. 4. Structural and tectonic setting of the 2010 Mw 7.8 Mentawai tsunami earthquake, Sumatra, Indonesia. a) Slip distribution (red contours) of the 2010 Mentawai tsunami earthquake [Hill et al., 2012] and location of seismic and bathymetric profiles. b) Bathymetry along profiles Pagai1 and Pagai2. c) Interpretation of representative seismic profile CGGV020 [Hananto et al., 2020] showing the structure and extent of the outer wedge. PU represents a pop-up block bounded by conjugate bi-vergent thrusts. For other definitions, see the caption of Fig. 3. (For interpretation of the references to colour in this figure legend, the reader is referred to the web version of this article.)

proposed to fit the coastal waves observed on nearby islands [Hill et al., 2012]. Detailed seismological, morphological, and tsunami waveform analyses suggest that the rupture of bi-vergent frontal thrusts likely controlled the outsize tsunami of the Mentawai event [Yue et al., 2014; Li et al., 2016; Bradley et al., 2019; Hananto et al., 2020].

The combination of seismic profiles and bathymetry data indicates that most of the 2010 Mw 7.8 Mentawai tsunami earthquake rupture patch was confined within the frontal accretionary wedge, and presumably activated forward and backward-vergent faults of the outer wedge. While the details of the rupture propagation within these bivergent splay faults remain poorly constrained in the absence of seafloor observations, the spatial overlap of the Mentawai tsunami earthquake rupture with the outer wedge of the Sunda megathrust and

disproportional large run-up indicate a structural control of tsunami excitation.

2.3. 1994 Mw 7.8 and 2006 Mw 7.7 tsunami earthquakes at the Java Trench

A large thrust earthquake with a local magnitude (Ms) of 7.2 occurred near the Java Trench on June 2, 1994 [Abercrombie et al., 2001; Bilek and Engdahl, 2007]. Detailed broadband body-wave analysis suggests that it was a Mw 7.6 rupture dipping $\sim 12^{\circ}$ to the north and located at depth of ~ 16 km [Abercrombie et al., 2001]. The rupture generated a devastating tsunami that caused severe damage and a large death toll in Southern Java [Maramai and Tinti, 1997]. The tsunami was

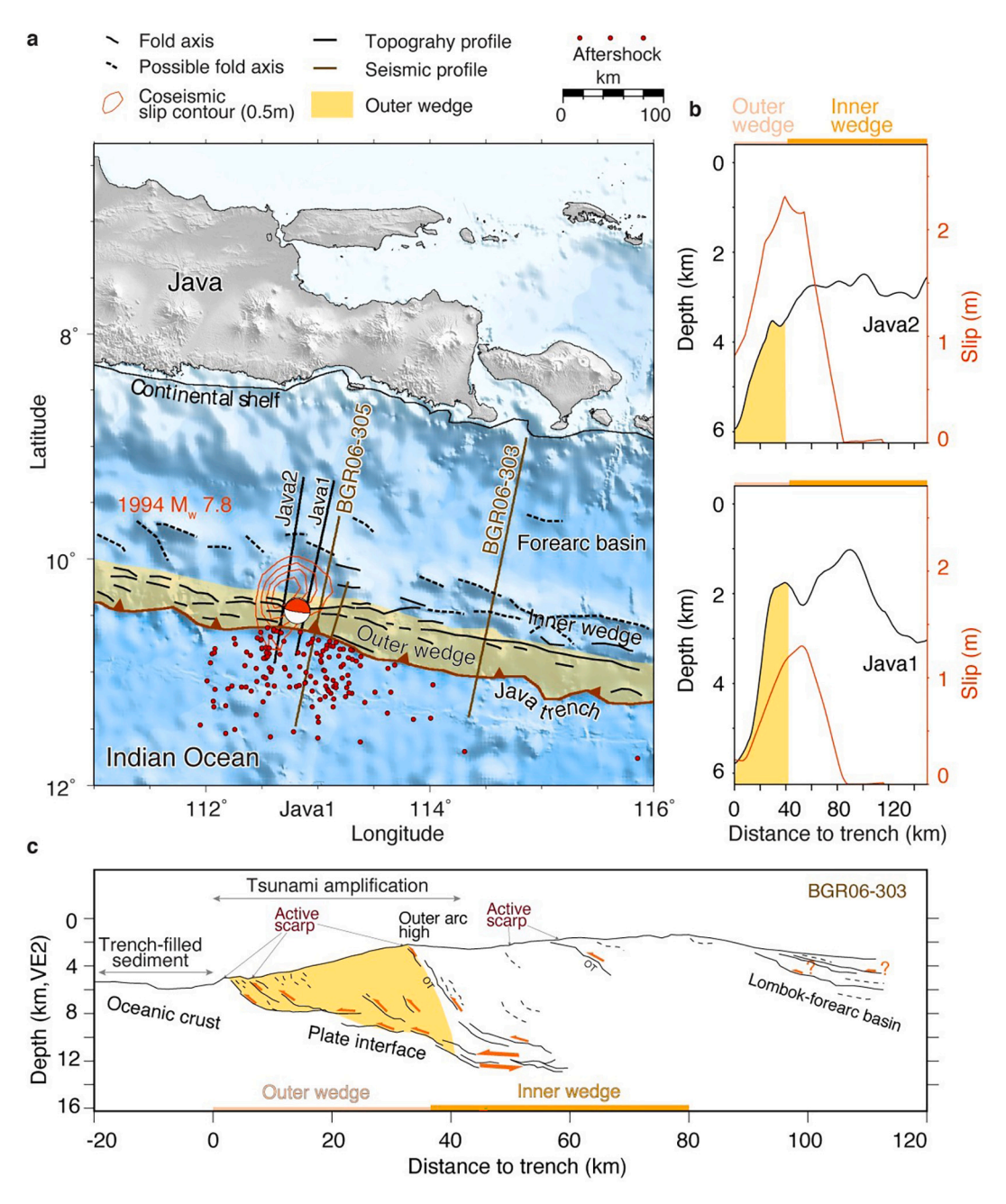


Fig. 5. Structural and tectonic setting of the 1994 Mw 7.8 Java tsunami earthquake, Java, Indonesia. a) Slip (red contours) distribution of the 1994 Java tsunami earthquake from the USGS FFM database [Hayes, 2017] and location of seismic profiles [Lüschen et al., 2011]. b) Bathymetry along profiles Java1 and Java2. c) Interpretation of representative seismic profile BGR06–303 Lüschen et al. [2011], which offers a better resolution than nearby profile BGR06–305. OT represents an out-of-sequence thrust. For similar definitions, see the caption of Fig. 3. (For interpretation of the references to colour in this figure legend, the reader is referred to the web version of this article.)

characterized by wave heights greater than 5 m along the coastline and a maximum run-up of \sim 9.5 m at Rajekwesi [Maramai and Tinti, 1997]. The seismic rupture may have propagated slowly (\sim 80-90 s) to the trench, with a deficiency in high-frequency seismic radiation and a maximum slip area located northeast of the hypocenter [Abercrombie et al., 2001]. A more recent model [Hayes, 2017] suggests a rather more compact slip distribution concentrated near the hypocenter (Fig. 5). The earthquake triggered many normal-faulting aftershocks in the subducting plate [Abercrombie et al., 2001], indicating that the rupture reached the trench and brought the outer-rise to failure [Sladen and Trevisan, 2018]. These observations imply that a majority of the coseismic slip of the 1994 Java rupture took place near the frontal prism of the Java Trench (Fig. 5c).

The Java arc forms the southern boundary of the Sundaland where an older section of the Indo-Australian plate subducts beneath the Eurasian plate. The subduction margin is also characterized by a plateau separating the forearc basin from the frontal accretionary wedge, but the bathymetric highs are not prominent enough to form forearc islands, as offshore Sumatra. The seismic profiles offshore eastern Java and Bali illuminate several high-angle faults branching from the basal megathrust [Lüschen et al., 2011]. Based on the presence of oblique seismic reflectors and the steep topography, we estimate a 40 km wide outer wedge (Fig. 5c). The 1994 rupture was almost entirely confined within the outer wedge, with large coseismic slip coinciding with the location of a high-angle mega-splay fault in the BGR06–305 profile [Lüschen et al., 2011]. This wide fault may have produced an efficient pathway to convert slip on the megathrust to vertical seafloor displacement, contributing to the devastating tsunami waves along the Java coastline. The sub-horizontal décollement underlying the outer wedge would require more coseismic slip to uplift the seafloor without activating any

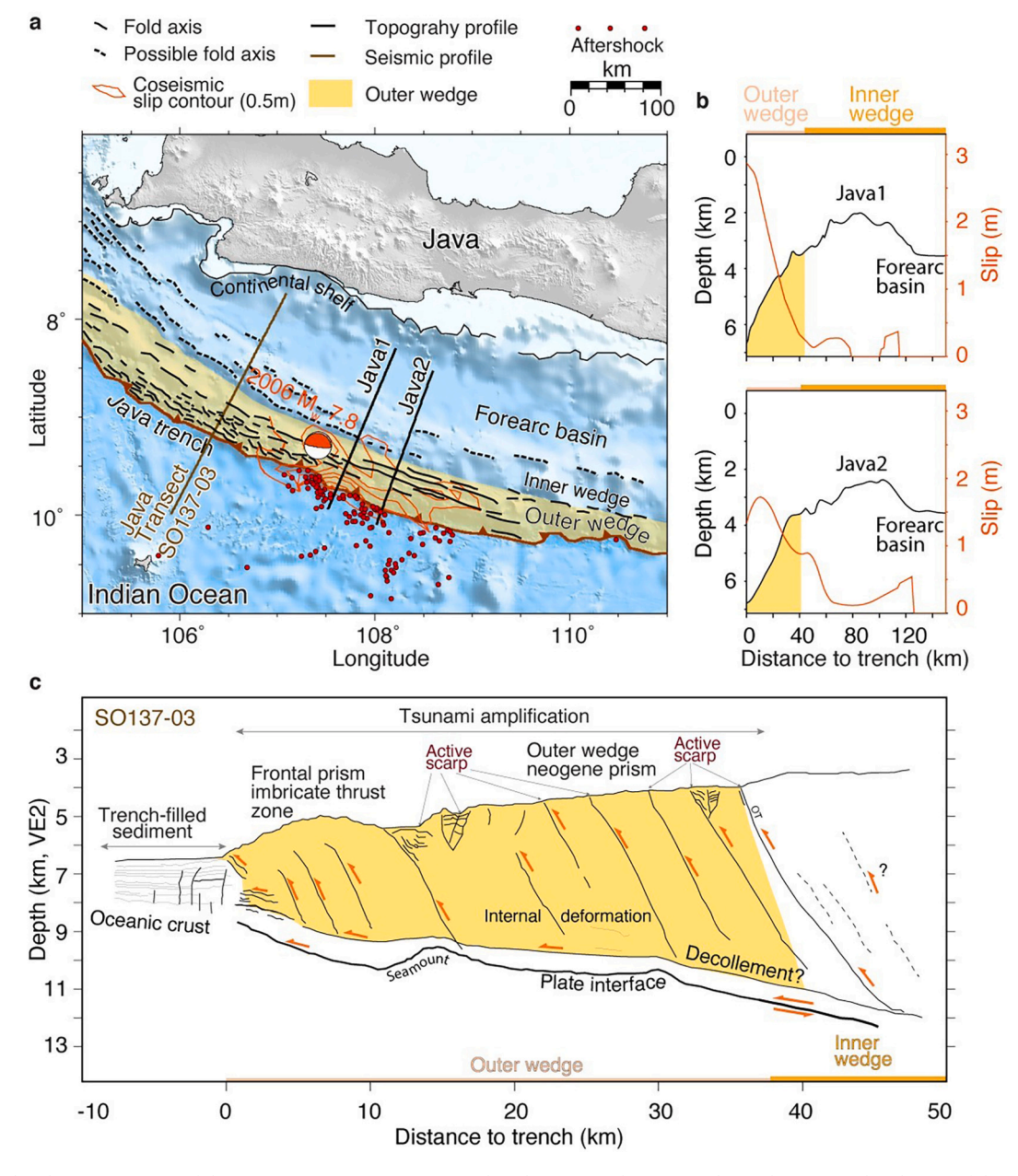


Fig. 6. Structural and tectonic setting of the 2006 Mw 7.7 Java tsunami earthquake, Java, Indonesia. a) Slip (red contours) distribution of the 2006 Java tsunami earthquake from the USGS FFM database [Hayes, 2017] and location of seismic profiles [Kopp et al., 2009]. b) Bathymetry along profiles Java1 and Java2. c) Interpretation of representative seismic profile SO137–03 [Kopp et al., 2009]. OT stands for the out-of-sequence thrust. For similar definitions, see the caption of Fig. 3. (For interpretation of the references to colour in this figure legend, the reader is referred to the web version of this article.)

hanging wall structure [Geist and Oglesby, 2014].

Northwest of the 1994 event on the Java Trench, another Mw 7.7 tsunami earthquake ruptured the shallow megathrust in 2006 [Ammon et al., 2006; Fujii and Satake, 2006; Fritz et al., 2007; Bilek and Engdahl, 2007]. It generated a destructive regional tsunami that killed more than 600 people and affected more than 300 km of the southern coastline of Java (Fig. 6). The international tsunami survey team reported a peaky wave (\sim 21 m) at the southern coast of Nusa Kambangan, with \sim 5–7 m wave height fairly uniformly distributed along 200 km of the surrounding coastline [Fritz et al., 2007]. A recent slip model places the majority of the coseismic slip distribution on the shallow megathrust near the trench [Hayes, 2017], which is further supported by the

triggering of outer-rise aftershocks [Sladen and Trevisan, 2018]. Back-projection of the radiated seismic waves reveals a variable-speed rupture propagating at \sim 1 km/s in the first 60 s, then at 2.7 km/s in the remaining 100 s [Fan et al., 2017]. Furthermore, the back-projection of the tsunami wave indicates that the source of the wave crest coincides with the high-frequency radiation in the outer wedge, suggesting the activation of high-angle splay faults.

Taking the nearby seismic profile SO137–03 [Kopp et al., 2009] as a representative cross-section, the source of the 2006 rupture coincides with a well-developed thrust-and-fold belt within a 40 km-wide outer wedge (Fig. 6c). The internal structure of the outer wedge consists of parallel imbricate thrust faults splaying off the basal décollement. The

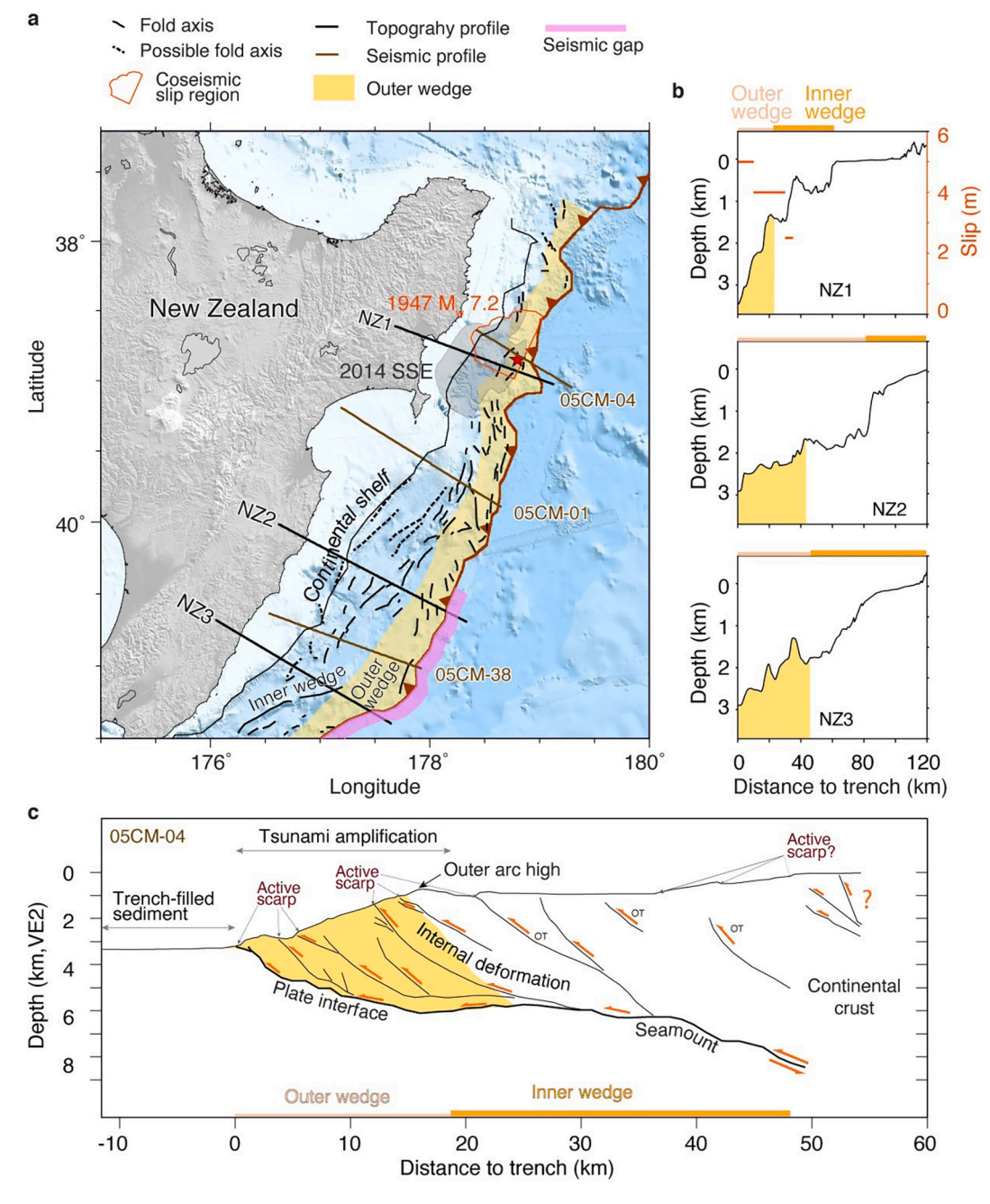


Fig. 7. Structural and tectonic setting of the 1947 Mw 7.1 Poverty Bay tsunami earthquake, New Zealand. a) Estimated rupture region (red box) [Bell et al., 2010] and location of seismic profiles (brown-solid lines) [Barker et al., 2009]. The shaded gray area shows the 2014 slow-slip event region [Wallace et al., 2016]. b) Bathymetry along profiles NZ1–3. c) Interpretation of representative seismic profile 05CM-4 [Barker et al., 2009]. Other profiles include 05CM-01, 38 [Barker et al., 2009]. See the caption of Fig. 3 for more details. (For interpretation of the references to colour in this figure legend, the reader is referred to the web version of this article.)

inner wedge is squeezed underneath the plateau that separates the forearc basin from the steep outer wedge. As evidenced by the coincidence between the source of the tsunami wave crest and high-frequency seismic radiations with the high-angle splay faults of the outer wedge, we conclude that the high-angle thrust faults likely slipped during the seismic rupture to generate the destructive tsunami waves that broke at Nusa Kambangan. The majority of high coseismic slip occurred within the frontal prism.

2.4. 1947 Mw 7.1 tsunami earthquake at the Hikurangi Trench

Two earthquakes with an estimated Mw <6 occurred on March 25 and May 17, 1947 offshore Poverty Bay and Tolaga Bay, New Zealand, respectively (Fig. 7). These two seismic events exhibited slow rupture, long duration, and low-frequency radiation, and took place in the weak sediment of the shallow accretionary prism [Eiby, 1982; Bell et al., 2010]. They generated abnormally large tsunami waves (\sim 10 m) that caused damage to coastal structures between Anaura Bay and Mahia Peninsula [Eiby, 1982]. Based on seismological, magnetic, and geodetic data and on tsunami modeling, two slip scenarios have been proposed for these events: a uniform 2.6 m coseismic slip and a variable slip distribution with a maximum slip reaching 5–6 m [Bell et al., 2010]. However, the proposed models require an extremely slow rupture \sim 150–300 m/s and the predicted tsunami heights underestimate the observations, suggesting the presence of another tsunami excitation mechanism.

The Hikurangi subduction zone offshore North Island, New Zealand is the southern termination of the Tonga-Kermadec intra-oceanic subduction zone where the over-thickened oceanic crust of the Hikurangi Plateau subducts obliquely underneath the eastern edge of the Indo-Australian plate [Nicol and Beavan, 2003; Wallace et al., 2009]. Contrarily to the Kermadec segment to the north, the Hikurangi margin is an accretionary margin. Seismic imaging offshore North Island illuminates many reverse faults that splay from the subduction interface [Barnes et al., 2002; Mountjoy and Barnes, 2011]. In particular, the seismic profile 05CM-04 [Barker et al., 2009] crosses the rupture area of the 1947 Mw 7.2 Poverty Bay tsunami earthquake and reveals a strongly deformed outer wedge with numerous high-angle splay faults that sole into the basal plate interface. Based on the distribution of active faults and bathymetric features, we estimate an outer-wedge width of 18 km (Fig. 7c). The separation of a steep frontal prism from a flatter inner wedge by the rest of the outer ridge is a distinctive feature of the Hikurangi accretionary prism that is imaged in other seismic profiles [Barker et al., 2009]. As the inferred coseismic slip area of the 1947 tsunami earthquakes is fully encompassed by the outer wedge, we suggest that some of the high-angle thrust faults may have slipped during the ruptures, resulting in anomalously high tsunami waves along the coast.

2.5. 1896 Mw 8.0 Sanriku tsunami earthquake at the Japan Trench

The June 15, 1896 Sanriku, Japan earthquake generated a large tsunami that claimed about 20,000 lives [Satake et al., 2017]. The earthquake was estimated by a local magnitude at Ms. 7.2 using global surface wave data [Abe, 1994], but was revised at Mw 8–8.2 based on aftershock activity [UTSU, 1994]. Although the shaking of the Sanriku earthquake was weak, it generated a disproportionately high tsunami of tsunami magnitude (Mt) 8.6 with maximum run-up of 38 m [Abe, 1979; Satake et al., 2017]. Early tsunami modeling constrains the rupture as a 50 x 210 km area located underneath the shallow accretionary prism [Tanioka and Sataka, 1996]. However, new tsunami wave height and tide gauge data analysis indicates that the slip distribution of the 1896 tsunami earthquake and the 2011 Mw 9.1 Tohoku earthquake may be complementary, with about 20 m of coseismic slip on a deeper portion in 1896 and 20–36 m of coseismic slip on the shallower section in 2011 [Satake et al., 2017]. Although the inferred slip of the 1896 and 2011

earthquakes differ remarkably at the same location, they produced a comparable tsunami run-up along the coast of Miyako and Kuji [Choi et al., 2012; Satake et al., 2017]. These observations suggest that other tsunami excitation mechanisms were involved during the shallow rupture.

The Japan Trench is an erosive margin that forms the boundary between the Okhotsk and Pacific plates where the subduction thickens the Japanese island arc [Takahashi et al., 2003; Miura et al., 2005]. The accretionary prism of the Japan Trench is conveniently decomposed into the lower, middle, and upper slopes [Kodaira et al., 2012; Nakamura et al., 2013; Boston et al., 2017; Kodaira et al., 2017]. The frontal prism is tucked below the lower slope and the outer wedge extends below the lower and middle slopes. The inner wedge sits below the upper slope and forms a dynamic backstop of Pliocene-Pleistocene and Miocene sediment [Kodaira et al., 2017]. The deformation style varies greatly along strike with a mega-splay normal fault bounding the outer wedge offshore Miyagi and a large thrust offshore Sanriku [Tsuji et al., 2013]. We take the seismic profile D19 of Kodaira et al. [2017] and the multibeam bathymetric profile SO251A [Fujiwara et al., 2017] as representative cross sections for the 1896 Mw 8 Sanriku tsumami earthquake (Fig. 8). The rough plate interface is cut by many normal faults inherited from bending of the outer rise. The outer wedge is split by two major high-angle thrust faults branching from the megathrust: one bounds the frontal prism and manifest itself by active scarps; the other is farther landward and is covered by a kilometer of sediment cut by normal faults near the slope break. Based on the extent of major splay faults and the steep bathymetry, we estimate a 35 km wide outer wedge. The rupture width of the 1896 Mw 8 Sanriku tsunami earthquake is consistent with the outer wedge, suggesting that the activation of thrust faults in the outer wedge contributed to the large tsunami that inundated the Sanriku coast in 1896.

2.6. 1963 Mw 7.8 and 1975 Mw 7.5 tsunami earthquakes at Kuril Trench

On October 20, 1963 an earthquake with Ms. 8.2 ruptured at shallow depth of the megathrust far offshore the Kuril Island [Fukao, 1979]. The full sequence included many low-angle thrust foreshocks and aftershocks [Fukao, 1979]. The slow rupture, shallow depth, low-frequency radiation, and long duration (~100 s) determined from long-period surface wave, along with the disproportional tsunami are hallmarks of a tsunami earthquake [Kanamori, 1972]. The largest aftershock occurred farther seaward, close to the trench, and generated a surprisingly large tsunami, but with a much shorter (~60 s) duration than that of the mainshock [Fukao, 1979]. Due to its slow rupture and large tsunami, this aftershock itself is characterized as a tsunami earthquake [Kanamori, 1972; Fukao, 1979]. This is the first observation of a trench-breaking earthquake triggering another tsunami earthquake.

Along the same trench, southwest of the 1963 tsunami rupture sequence, another shallow (\sim 15 km) Ms. 7.0 earthquake rattled the megathrust offshore east Hokkaido, Japan on June 10, 1975 (Fig. 8) [Fukao, 1979]. The rupture area is farther offshore of previous tsunami events, i.e., 11 August 1969 Ms. 7.9 and 17 June 1973 Ms. 7.7 [Fukao, 1979]. The relocated hypocenter depth is at \sim 3 km, indicating an extremely shallow rupture [Fukao, 1979]. A comparison of rupture characteristics, tsunami run-up, and spectral amplitude ratio at long period between these nearby events indicated that the shallow 1975 rupture was a tsunami earthquake with a dimension of \sim 100 \times 60 km [Fukao, 1979].

The 1963 and 1975 tsunami earthquakes share many commonalities in rupture characteristics. The initial rupture phase is characterized by thrust motion on a gently dipping megathrust $<5^{\circ}$ constrained by the first arrivals, but a large change in dipping angle from 20 to 45° is necessary to explain the polarity of seismic waves [Fukao, 1979], similar to the change in dipping angle revealed by the rupture speed and the back-projected tsunami waves during the 2006 Mw 7.8 Java tsunami

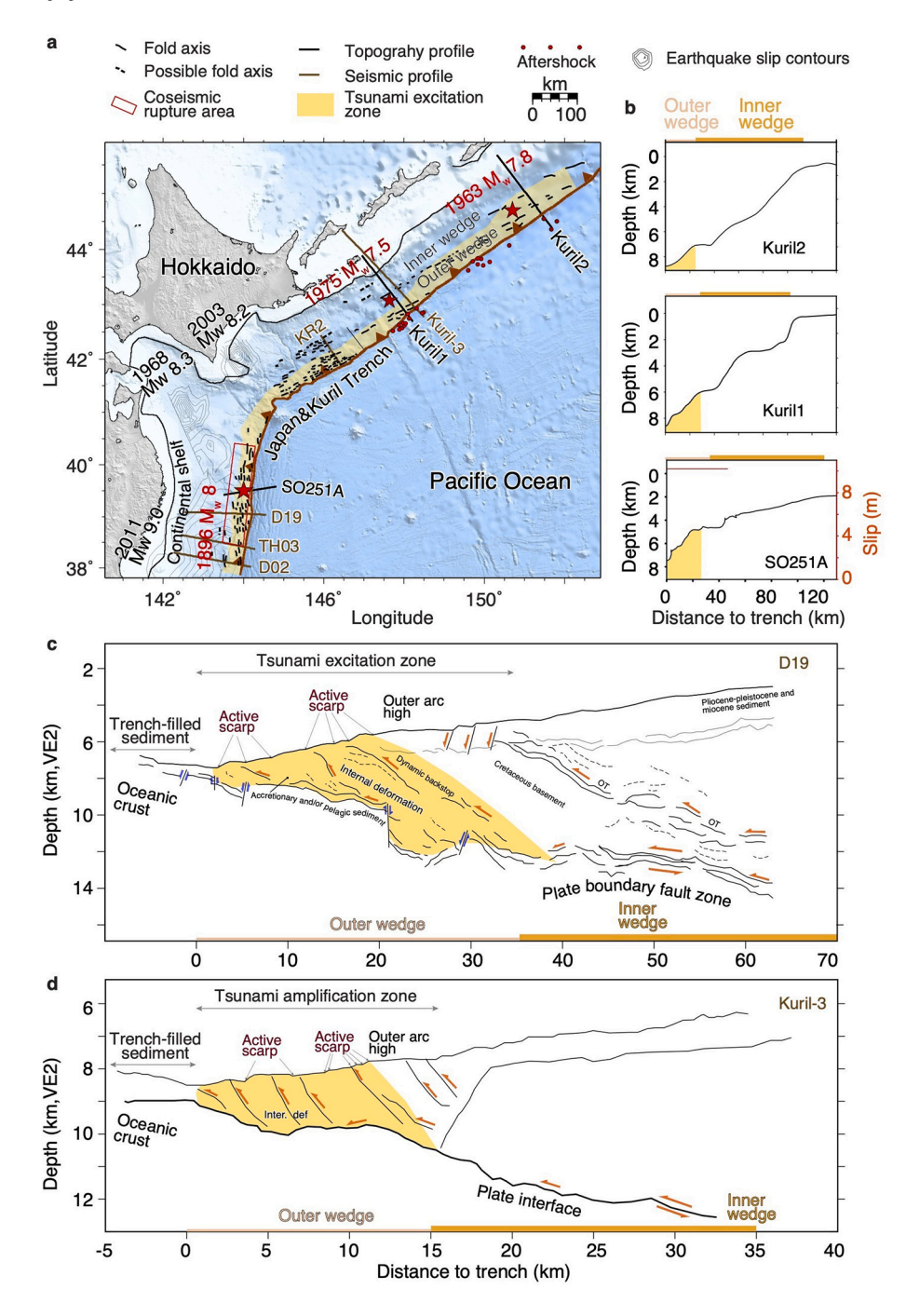


Fig. 8. Structural and tectonic setting of the 1896 Mw 8.0 Sanriku, 1963 Mw 7.8 and 1975 Mw 7.5 tsunami earthquakes, at Japan and Kuril subduction zones, respectively. a) Footprints of the 1896 (red box) [Satake and Tanioka, 1999], 2003 Mw 8.2 [Koketsu et al., 2004], 2011 Mw 9.0 [Wei et al., 2012] earthquake ruptures and location of seismic profiles [Kodaira et al., 2017; Klaeschen et al., 1994; Okamura et al., 2008]. b) Bathymetry along profiles SO251A [Tsuru et al., 2002], Kuril1, and Kuril2. c) and d) Interpretation of representative seismic profiles D19 in Japan [Kodaira et al., 2017] Kuril-3 [Klaeschen et al., 1994], respectively. Other profiles include TH03, D02 [Kodaira et al., 2017]. OT represents an out-of-sequence thrust. For additional information, see the caption of Fig. 3. (For interpretation of the references to colour in this figure legend, the reader is referred to the web version of this article.)

earthquake [Fan et al., 2017]. The change in dip angle and the efficient tsunami excitation suggest that the rupture of both 1963 and 1975 events initiated and propagated to the shallow megathrust and then activated the high-angle faults in the outer wedge [Fukao, 1979].

The accretionary wedge of the Kuril Trench follows a similar nomenclature as the Japan Trench with a middle terrace separating the lower and middle slopes [Okamura et al., 2008; Klaeschen et al., 1994]. While high-quality seismic data for the 1963 tsunami earthquake rupture region seem lacking, the seismic profile *Kuril line 3* [Klaeschen et al., 1994] crosses the 1975 tsunami earthquake rupture area (Fig. 8). The profile highlights numerous steep thrust faults branching from the megathrust at shallow depth and slope-break area in the 15 km wide outer wedge. The shallow hypocentral depth of the 1963 and 1975 events and the steep branching rupture proposed by Fukao [1979] coincide with the high-angle (18–48°) thrusts faults of the outer wedge

(Fig. 8). We suggest that some of these thrust faults ruptured during these two earthquakes, resulting in the unexpectedly large tsunami.

2.7. 1946 Mw 8.2 Unimak tsunami earthquake at the Aleutian Trench

On April 1st, 1946, a Ms. 7.4 seismic rupture unzipped the shallow megathrust offshore Unimak Island, Aleutian (Fig. 9), producing a Mt. 9.3 tsunami [Johnson and Satake, 1997] that killed 167 people and generated a 42 m tsunami wave at Scotch Cap [Fryer et al., 2004]. The tsunami size was larger than that of the neighboring events, i.e., the 1957 Mw 8.6 (Mt 9.0) Aleutian and 1964 Mw 9.2 (Mt 9.1) Alaska earthquake, despite the lower moment magnitude, which is characteristic of a tsunami earthquake [Kanamori, 1972; Johnson and Satake, 1997]. Various explanations for the anomalous tsunami waves have been proposed. The near-field tide gauge data is compatible with a 80 x

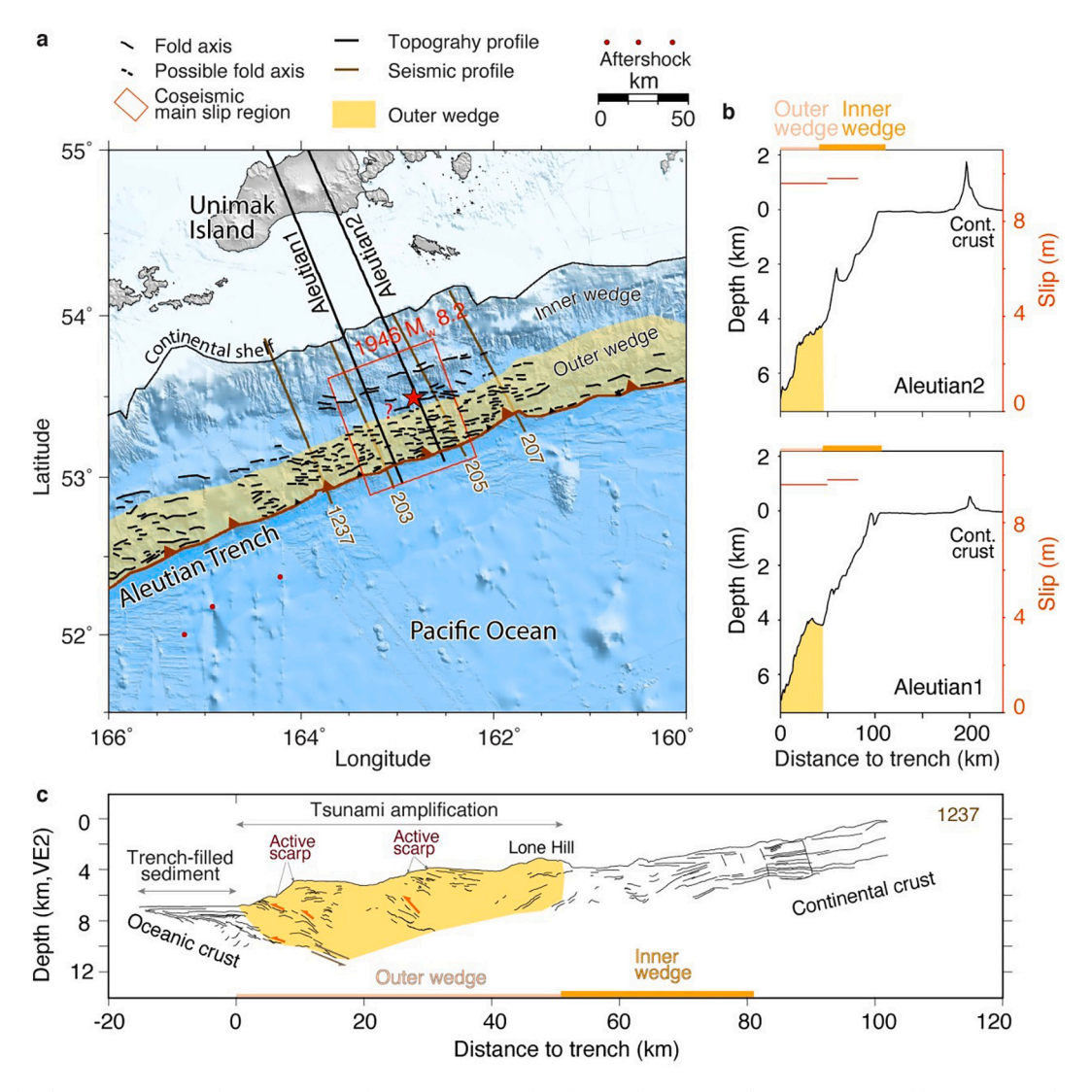


Fig. 9. Structural and tectonic setting of the 1946 Mw 8.2 Aleutian tsunami earthquake, Kuril. a) Estimated rupture region (red box) [Satake and Tanioka, 1999] and location of seismic profiles [Miller et al., 2014]. b) Bathymetry along profiles Aleutian1 and Aleutian2. c) Interpretation of representative seismic profile 1237 [Miller et al., 2014]. Other profiles include 203, 205 [von Huene et al., 2016], 207 [Miller et al., 2014]. For the remaining definitions, see the caption of Fig. 3. (For interpretation of the references to colour in this figure legend, the reader is referred to the web version of this article.)

145 km Mw 8.2 rupture with \sim 10 m of coseismic slip on two shallow patches [Johnson and Satake, 1997]. However, the resulting model cannot explain the second peaky wave recorded at a Honolulu, Hawaii tide gauge. Explaining near- and far-field tsunami waveform records requires a 40-60 x 160 km rupture of magnitude Mw 8.1 [Tanioka and Seno, 2001], slightly narrower than that estimated by Johnson and Satake [1997]. Tanioka and Seno [2001] also warn that additional sediment uplift due to deformation within the wedge may lower the coseismic slip estimate of the megathrust. Alternatively, a submarine landslide is also a possible mechanism for the peaky wave measured by 42 m at Scotch Cap and 6 m at Sanak Village [Fryer et al., 2004].

The Aleutian Trench marks the subduction of the Pacific plate below the North American plate. The Unimak segment corresponds to the transition between the continental arc bounding the Bering Shelf and the Aleutian Island Arc to the west, which is accompanied by a transition of geodetic coupling on the plate interface [Fournier and Freymueller, 2007; Li and Freymueller, 2018] and of internal structure of the accretionary prism [von Huene et al., 2016; von Huene et al., 2021]. Along the Aleutian Island Arc, the upper and lower slopes of the accretionary wedge are separated by the Aleutian Terrace [Miller et al., 2014]. Off the Bering Shelf, the lower, middle, and upper slopes form a more

continuous structure. However, a major splay fault zone bounding the frontal prism can be found along the Aleutian Trench [von Huene et al., 2021]. The source area of the 1946 Unimak tsunami earthquake was imaged across multiple seismic profiles but *RV Ewing line 1237* [Miller et al., 2014], located on the western end of the 1946 rupture, provides better resolution at depth (Fig. 9). At the Unimak segment, the outer wedge stretches for 50 km from the trench to the Lone Hill outer arc high, characterized throughout by highly tilted seismic horizons. An active scarp on the lower slope above a large splay fault marks the boundary of the frontal prism. Another major splay fault can be found in the middle of the outer wedge, below the middle slope. The epicenter of the 1946 Unimak earthquake sits above the central splay fault of the outer wedge [von Huene et al., 2021]. The location of splay faults is consistent with the narrow fault rupture and the extra uplift region proposed in previous tsunami studies [Tanioka and Seno, 2001].

2.8. 1992 Mw 7.7 Nicaragua tsunami earthquake at the Middle-American Trench

A tsunami earthquake ruptured the Middle-American trench offshore Nicaragua on September 2nd, 1992 (Fig. 10) with a local magnitude Ms.

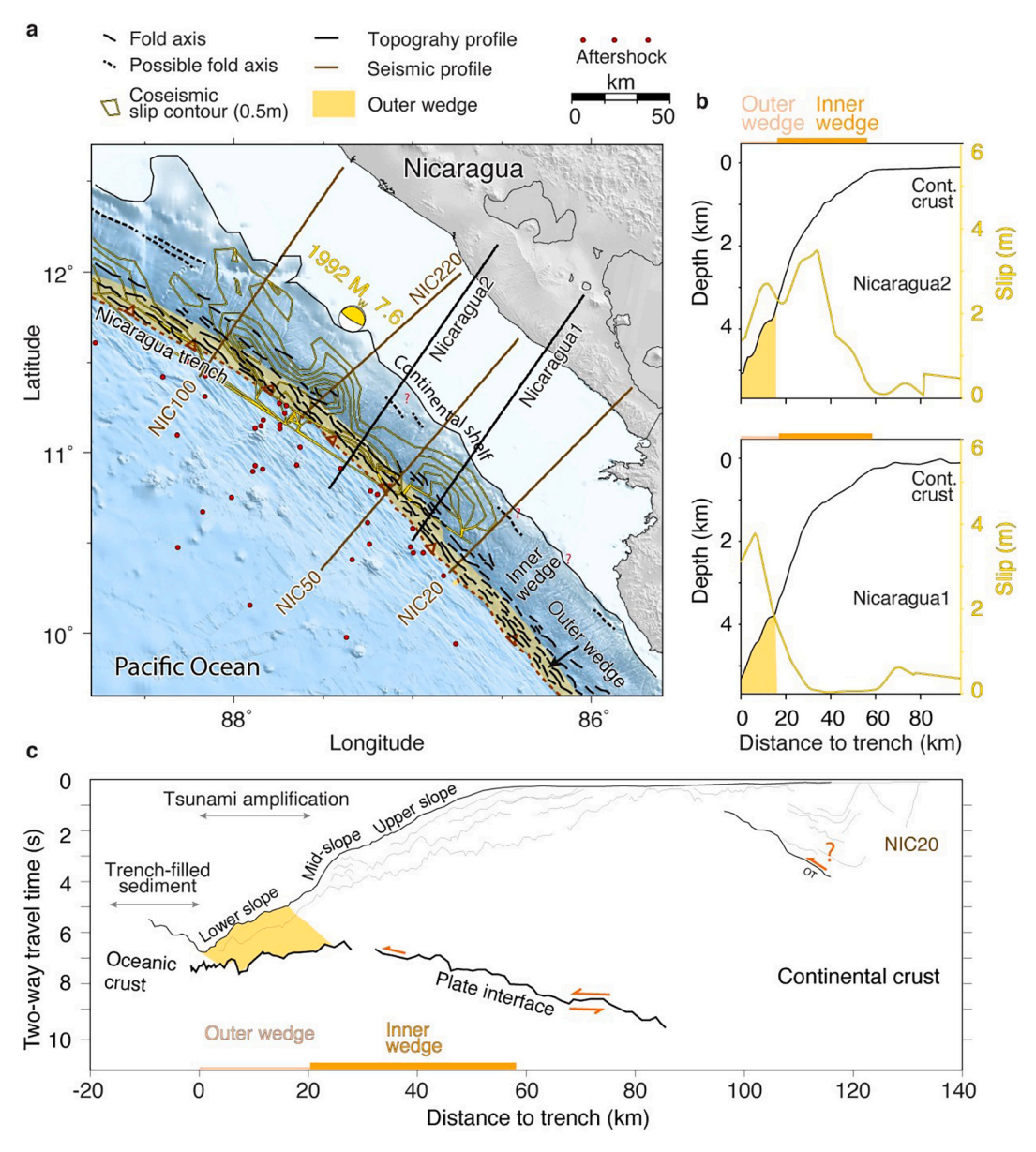


Fig. 10. Structural and tectonic setting of the 1992 Mw 7.7 Nicaragua, Central America tsunami earthquake. a) Slip model (yellow contours) retrieved from the USGS FFM database [Hayes, 2017] and location of seismic profiles [Sallares et al., 2013; McIntosh et al., 2007]. b) Bathymetry along profiles Nicaragua1 and Nicaragua2. c) Interpretation of representative seismic profile NIC20 [Sallares et al., 2013] at a representative cross-section. Other available seismic profiles include NIC50 and 100 [McIntosh et al., 2007], and NIC220 [Ranero and von Huene, 2000]. OT stands for out-of-sequence thrust. (For interpretation of the references to colour in this figure legend, the reader is referred to the web version of this article.)

7-7.3 and moment magnitude Mw 7.6-.

7.7 [Piatanesi et al., 1996; Satake, 1994]. It slowly ruptured the shallow megathrust with a disproportionately long duration of $\sim 100~\text{s}$ [Satake, 1994]. Body- and surface-wave analyses indicate a bilateral rupture over a 200 x 100 km area [Ide et al., 1993]. The quake generated tsunami waves with 9 m maximum run-up along the coast of Nicaragua, claiming 170 lives. Tide gauge data is compatible with 3 m of coseismic slip distributed over a 250x40 km area [Satake, 1994]. A variable slip distribution with larger slip northwest and southeast of the hypocenter was also suggested for this event [Piatanesi et al., 1996]. The seismic and tsunami wave data indicate that the initial tsunami waves were confined in a ~ 40 –50 km wide area near the trench.

The Mid-American Trench is an erosive margin [Clift and Vannucchi, 2004] where the Cocos plate subducts underneath the North American and Caribbean plates. We use the *NIC20* seismic profile [Sallares et al., 2013; McIntosh et al., 2007] that crosses the 1992 Nicaragua earthquake

rupture area as a representative cross-section (Fig. 10c). The section below the continent shelf is decomposed into the lower, middle, and upper slopes [Sallares et al., 2013]. The middle and upper slopes are overlain by at least a kilometer of surficial sediment cut by numerous normal faults, indicative of mass wasting. The lower slope is separated from the middle slope by a scarp, presumably the result of active folding or thrust faulting. The outer wedge conflates with the 22 km-wide frontal prism beneath the lower slope, with little sign of localized deformation. The distinctively undeformed outer wedge of the Nicaragua margin may explain the relatively small tsunami run-up of the 1992 tsunami earthquake (Fig. 1b and c).

2.9. 1996 Mw 7.5 Peru tsunami earthquake at the Peru Trench

On February 21st, 1996, a tsunami earthquake rattled the Peruvian subduction zone megathrust offshore the northern coast of Peru at depth

of \sim 10 km (Fig. 11). It ruptured with a gentle dipping thrust mechanism and a magnitude of Ms. 6.6 and Mw 7.5, respectively [e.g., Satake and Tanioka, 1999; Ihmle et al., 1998]. It triggered a large localized tsunami wave reaching 1–5 m that claimed 12 lives in Peru [Satake and Tanioka, 1999; Heinrich et al., 1998]. The tsunami information at the near- and far-field tide gauges in Galapagos Island and Hawaii suggest a tsunami magnitude Mt. 7.8 [Satake and Tanioka, 1999]. Seismological analysis indicates a bilateral trench-parallel rupture over \sim 110 km in length with the majority of coseismic slip confined to 30x30 km area south of the hypocenter, lasting \sim 50 s [Ihmle et al., 1998]. Reconciling the tsunami waves measured by tide gauges at Chimbote and Salaverry, Peru requires a rupture with 2–4 m of coseismic slip on a 150 \times 40–80 km area [Satake and Tanioka, 1999].

The Peruvian subduction zone is an erosive margin at the boundary between the Nazca and South American plates. We take the seismic profile *Peru 2* of von Huene et al. [1985] that crosses the high coseismic slip area of the 1996 earthquake as a representative section (Fig. 11c). The 17 km wide outer wedge stretches from the trench axis to an outer arc high. More thrusts can be found landward, but they are overlain by horizontal sediment layers indicating little ongoing deformation in the

inner wedge. Several imbricate faults cut the outer wedge, with a high fault density in the frontal prism. The seismic and tsunami modeling determined slip models place the majority of the coseismic slip in a confined area near the trench, which correlates remarkably well with the faults and folds structure of the outer wedge. Some high-angle splay faults may have been activated during the 1996 rupture to amplify the tsunami waves.

3. Structural control on tsunami excitation

A structural analysis of the berthing ground of tsunami earthquakes (Figs. 3-11 summarized in Fig. S1) illuminates their relationship with the outer wedge of accretionary prisms at subduction zones. We present a quantitative summary of the structural observations in Table S2 and Fig. 12. The location of tsunami earthquake ruptures is generally subject to epistemic uncertainties associated with the limited resolution of seismo-geodetic inversions near the trench [Sathiakumar et al., 2017]. To mitigate the uncertainties associated with smoothing of the coseismic slip distributions, we define the rupture width in the trench-perpendicular direction as the distance where the slip is larger or

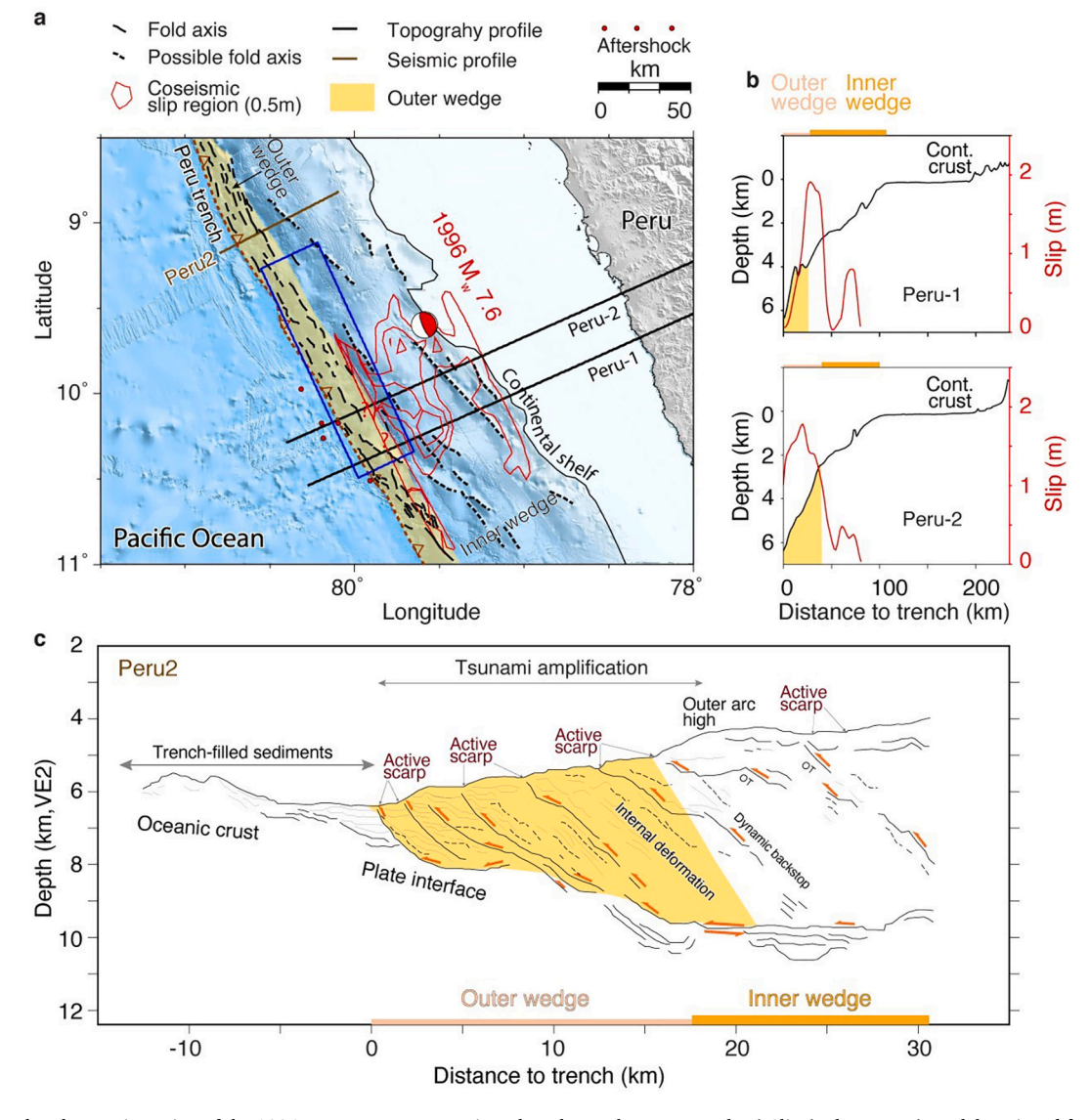


Fig. 11. Structural and tectonic setting of the 1996 Mw 7.5 Peru tsunami earthquake, at the Peru trench. a) Slip (red contours) model retrieved from the USGS FFM database [Hayes, 2017] and location of seismic profiles [von Huene et al., 1985]. We tied the finite-fault model to the trench. b) Bathymetry along profiles Peru1 and Peru2. c) Interpretation of representative seismic profile Peru2 [von Huene et al., 1985] at a representative cross-section. OT stands for out of sequence thrust. (For interpretation of the references to colour in this figure legend, the reader is referred to the web version of this article.)

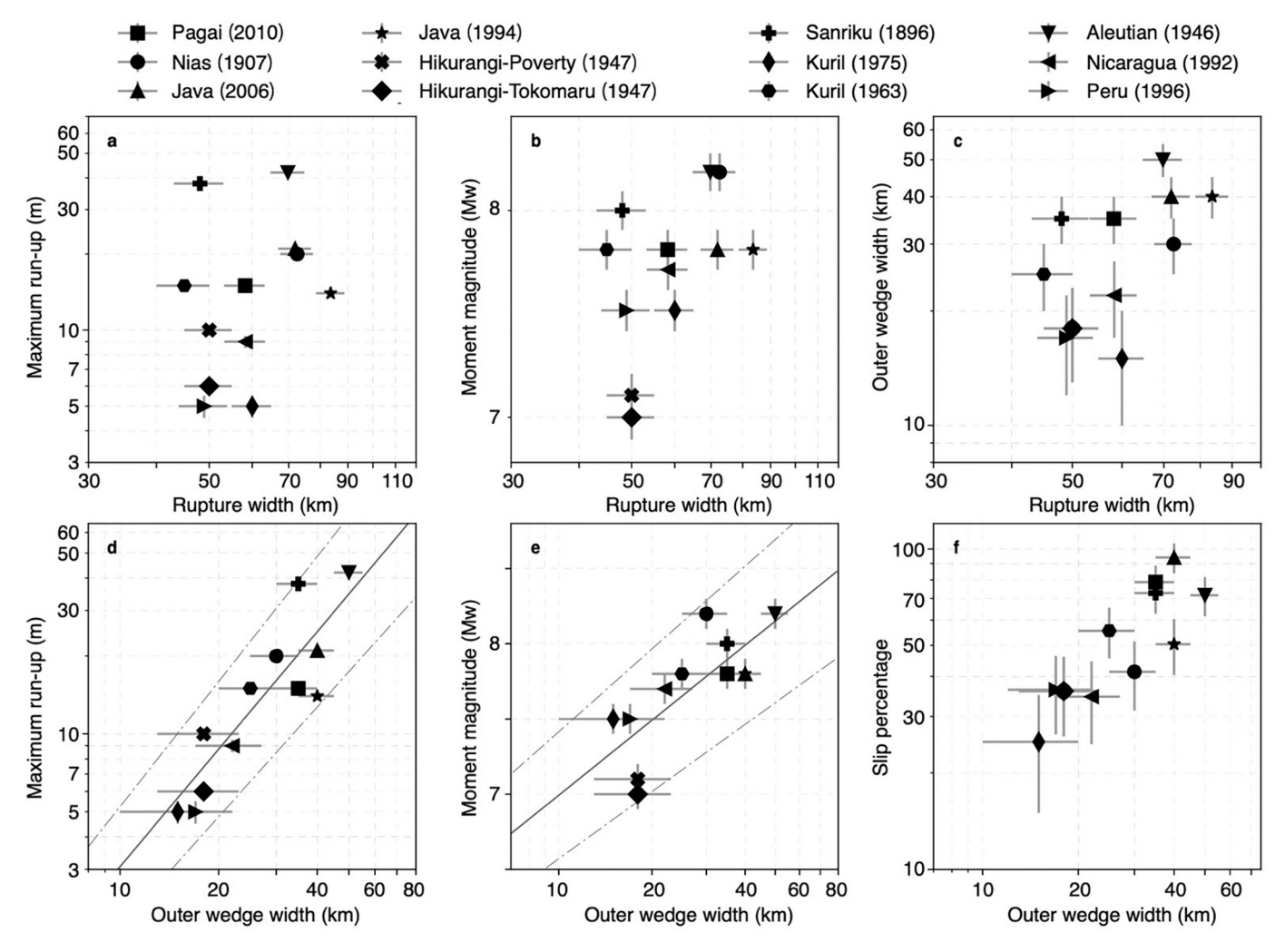


Fig. 12. Empirical relationships among run-up (Fig. 1), moment magnitude (Mw, Fig. 1), percentage of slip within the outer wedge, outer-wedge width, and effective rupture width for tsunami earthquakes since 1800. See also Fig. S2 and Table S2. A \sim 0.2 uncertainty in Mw reflects the variability from independent estimates.

equal to 10% of the maximum coseismic slip. We find that tsunami earthquake ruptures overlap with the outer wedge between 25 and 100%, and above 50% in most cases. There is little correlation between the estimated rupture width of tsunami earthquakes and the resulting earthquake moment magnitude and tsunami maximum run-up, presumably because of the presence of several other controlling variables. For example, earthquake size is otherwise controlled by the along-strike length of rupture, the overall stress drop, and the rigidity of the surrounding rocks [Nanjundiah et al., 2020].

In contrast, we find correlative outer-wedge width and maximum tsunami run-up; the wider the outer wedge, the higher the tsunami runup. The correlation between outer wedge width and maximum tsunami run-up holds independently of the inferred slip distribution of tsunami earthquakes, so it eliminates many uncertainties inherent to seismogeodetic inversions. This is exemplified by the 1907 Nias, Indonesia and 1946 Unimak, Aleutian tsunami earthquakes of the same moment magnitude (Mw 8.2) that ruptured in outer wedges of 30 and 50 km width, respectively, generating widely different tsunami waves of 20 and 42 m maximum run-up, respectively. Based on the data currently available, tsunami earthquakes that develop within an outer wedge narrower than 25 km, such as during the 1947 Poverty Bay and Tokomaru, 1975 Kuril, 1992 Nicaragua, 1996 Peru, generate tsunami waves smaller than 10 m. In contrast, tsunami earthquakes that occur within a well-developed outer wedge, such as the 1907 Nias, 1963 Kuril, 1896 Sanriku, 1946 Unimak, 1994 and 2006 Java, 2010 Mentawai earthquakes, generate larger tsunami waves. The correlation between outer-wedge width and tsunami run-up can be surprising given the various other possible controlling factors, such as the efficiency of seafloor uplift during rupture, the water depth at the source, and the topology of near-coastal bathymetry [Geist, 2002].

Based on these findings, we propose that an important factor for tsunami excitation is the overlap of seismic ruptures with the outer wedge at subduction margins. The outer wedge is the most actively deforming section of the hanging wall through faulting and folding. Deformation of the outer wedge takes place on imbricate, conjugate, or even bi-vergent faults that absorb a fraction of the relative convergence. As convergence is distributed among several structures that convert shortening into uplift, the long-term loading is reduced on the underlying megathrust [Sathiakumar et al., 2020], correspondingly increasing the recurrence time of tsunami earthquakes, making them less frequent than earthquakes of similar size at greater depths. In addition, the outer wedge is often associated with steeper slopes that transfer horizontal motion to apparent uplift of the seafloor more effectively. The highangle thrust faults within and the steeper seafloor slopes on top of the outer wedge may be responsible for the efficient excitation of tsunami waves, explaining the tsunamigenic potential of shallow earthquakes relative to similar-sized earthquakes that rupture deeper sections of the megathrust below the inner wedge or the crust. Efficient seafloor uplift may be facilitated when a seismic rupture propagates from the basal décollement to high-angle splay faults in the outer wedge, whether or

not the rupture initiated within or outside the outer wedge.

The correlative relationship between outer-wedge width and maximum tsunami run-up for tsunami earthquakes of moment magnitude from 7.1 to 8.2 allows us to place bounds on the tsunami run-up generated by future tsunami earthquakes based on the structural setting of the shallow accretionary prism. The results of Figs. 12d and 14a can be explained by a power-law relationship between maximum tsunami run-up of tsunami earthquakes and outer-wedge width. Similarly, the relationship between seismic moment of tsunami earthquakes and outer-wedge width can be explained by a power-law, although these data show more scatter (Fig. 12e).

O Northern Manila, line EW9509 (McIntosh et al. 2005) Western Makran, line 2 (Grando and McClay 2007) O Manila, line MGL0905-23 (Eakin et al. 2014) Eastern Makran, line 116 (Smith et al. 2012) Aleutian 1237 (Miller et al. 2014) 1946 Unimak tsunami earthquake O Luzon, line 973 (Lin et al. 2009) Lesser antilles, transect 3 (Fergusson et al. 1993) Cascadia, SO108 line 103 (Flueh et al. 1998) Two-way travel time (5 s) Distance (5 km) or Java trench SO137-03 (Kopp et al. 2009) 2006 tsunami earthquake -20 60 100 20 40 Distance from deformation front (km)

4. Empirical model of maximum tsunami run-up for trenchbreaking ruptures

The analysis of tsunami run-up from tsunami earthquakes illuminates a structural control of tsunami excitation that may operate for all types of trench-breaking ruptures. Activation of distinct structures in the outer wedge have also been observed to excite disproportional tsunami waves in great and giant earthquakes. For instance, mega-splays were involved in the rupture of the 1944 Mw 8.0 Tonankai [Park et al., 2002; Moore et al., 2007], 2004 Mw 9.2 Sumatra-Andaman [Singh et al., 2008; DeDontney and Rice, 2012], 2010 Mw 8.8 Maule [Lieser et al., 2014; Melnick et al., 2012], and the 1964 Mw 9.3 Alaska [Suleimani et al.,

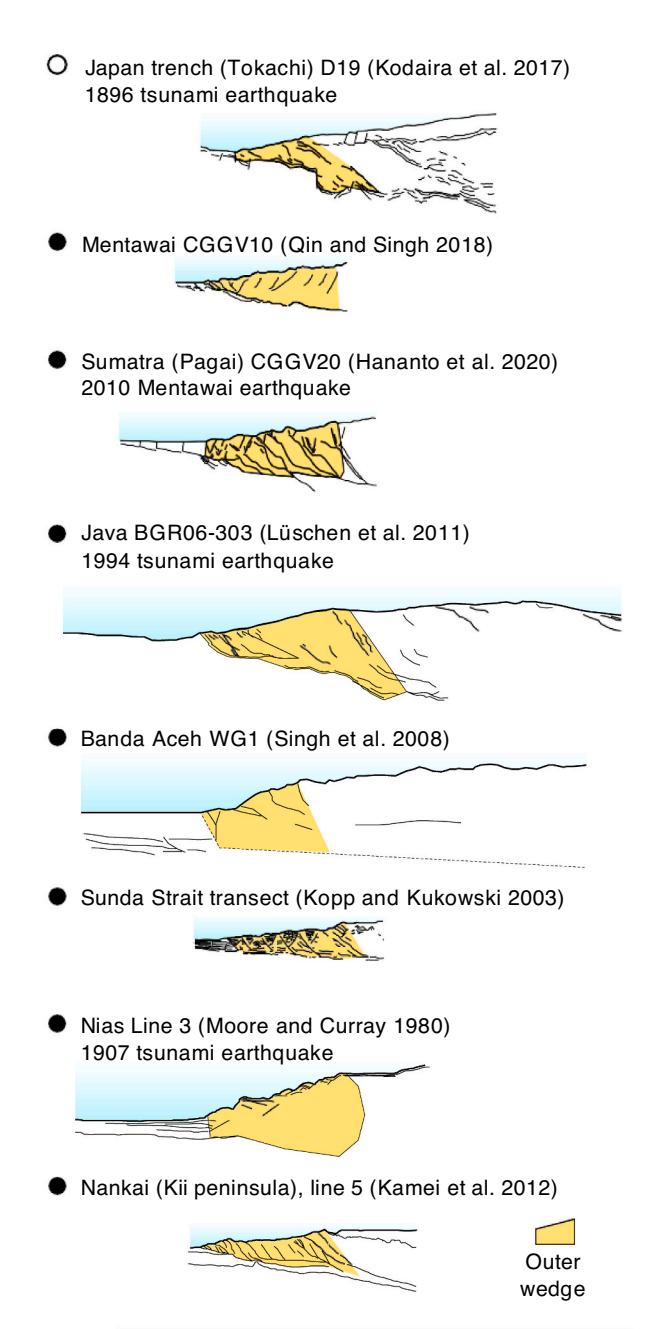


Fig. 13. Delineation of the outer wedge (yellow region) at global subduction zones, organized in descending order of outer wedge width (see also Fig. 20b and Table S3). The source of each seismic profile is labeled for each region and is also provided in Table S4. Accretionary and erosive margins are indicated by filled and open circles, respectively. (For interpretation of the references to colour in this figure legend, the reader is referred to the web version of this article.)

-20

20

40

Distance from deformation front (km)

60

80

100

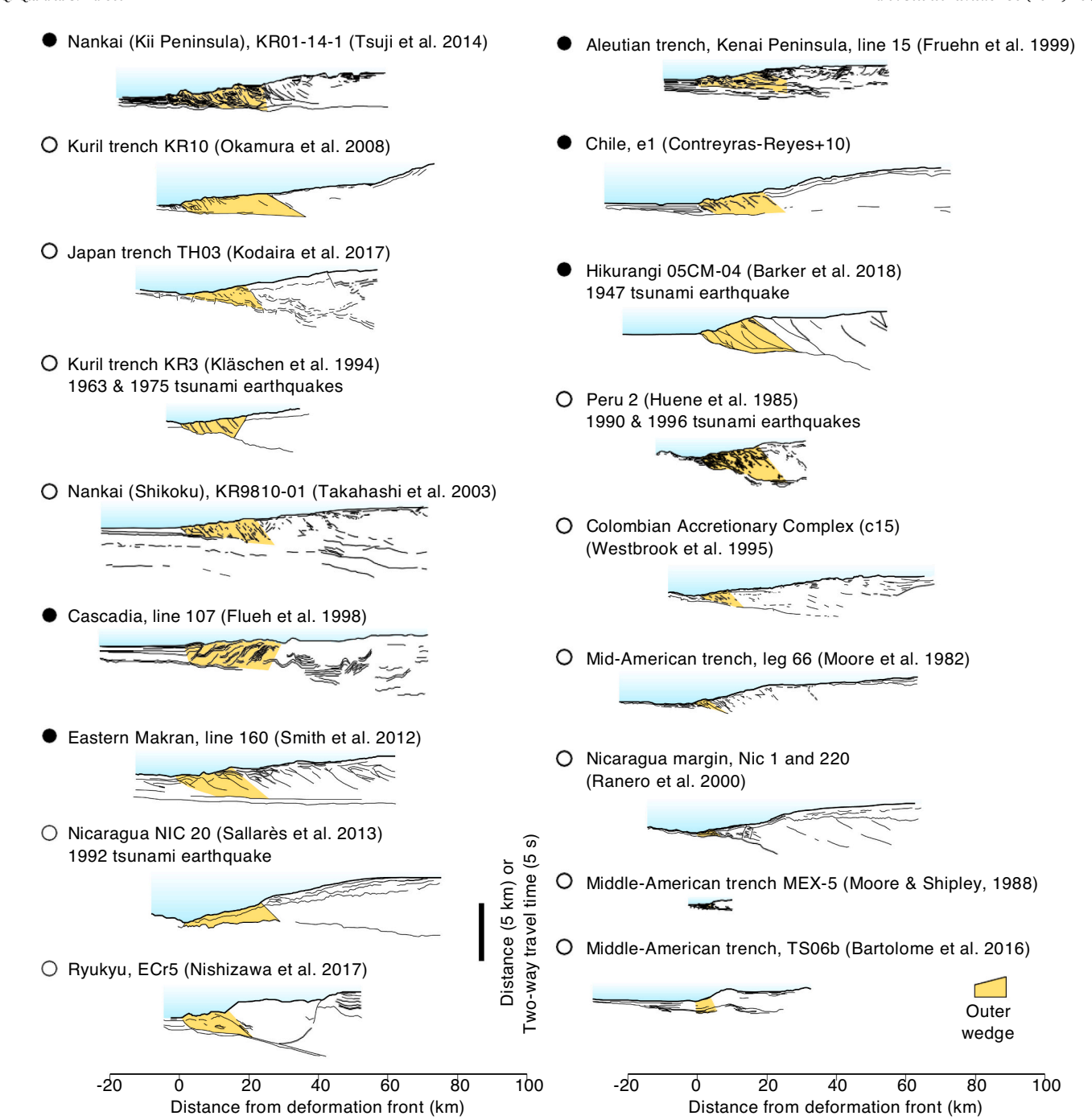


Fig. 13. (continued).

2008; Chapman et al., 2014; Suleimani and Freymueller, 2020] earthquakes. Seafloor bathymetric and geodetic measurements around the 2011 Mw 9.1 Tohoku-Oki earthquake provide direct evidence of shortening and uplift in the outer wedge [Ito et al., 2011; Fujiwara et al., 2011; Strasser et al., 2013]. These observations suggest that internal deformation of the outer wedge is an important factor for tsunami excitation. However, the tsunami waves produced by giant trenchbreaking earthquakes are also controlled by the size of the earthquake.

To estimate the maximum tsunami run-up of trench-breaking ruptures for a wide range of magnitudes, we propose an empirical relationship between run-up, outer-wedge width, and seismic moment, as follows

$$h^{max} = h_0 \left(\frac{w}{w_0}\right)^n \left(\frac{M_0}{m_0}\right)^m \tag{1}$$

where $h^{\rm max}$ is the maximum tsunami run-up, h_0 is a reference value, w is the outer wedge width with reference value $w_0=1$ km, M_0 is the seismic moment with reference $m_0=1$ x10¹⁸ N m. The model does not describe the tsunami run-up of blind ruptures. We calibrate the model using the data for tsunami earthquakes presented in Fig. 12d and for the 2004 Mw 9.2 Sumatra-Andaman, 2006 Mw 8.3 Kuril, 1964 Mw 9.2 Alaska, 2011 Mw 9.1 Tohoku, 2001 Mw 8.4 Southern Peru, 2010 Mw 8.8 Maule, 2015 Mw 8.3 Illapel, and 1960 Mw 9.5 Valdivia trench-breaking giant earthquakes. For each case, we gather representative seismic profiles and identify the outer wedge boundaries based on the presence of active

faults and folds and topographic slopes, following the approach detailed in Figs. 3 to 11 for tsunami earthquakes. The structural setting and our estimation of the outer wedge boundaries are presented in Fig. 13 and Table S3. We optimize the parameters $h_0=0.36 \times 10^{\pm 0.93}$ m, $n=0.963\pm 0.04$ and $m=0.254\pm 0.007$ using weighted least squares to obtain a reduced chi square of 1. In contrast, if we only consider a sensitivity of tsunami run-up to seismic moment (by forcing n=0 and optimizing the other parameters) or to outer-wedge width (this time by forcing m=0), we obtain reduced chi squares of 2.5 and 4, respectively (Supplementary Fig. S2). However, other factors such as local topology of bathymetry and earthquake source heterogeneity could also affect the maximum run-up, thus the model predicted errors are possibly underestimated.

We compare the model prediction with the tsunami run-up for the 8 trench-breaking ruptures covering moment magnitudes from 8.3 to 9.5

in Fig. 14b. The variability in the maximum run-up prediction is due to trench-parallel variations of outer wedge width and inherent uncertainties in model prediction associated with the uncertainties of model parameters. The predictions fall within a few percents of the observed maximum run-up. These findings are in striking contrast with the comparison with blind ruptures (Fig. 14c). For all the 1945 Mw 8.1 Makran, 2005 Mw 8.5 Nias, 2007 Mw 8.4 Bengkulu.

1946 Mw 8.3 Nankai, 2007 Mw 8.0 Peru, 2014 Mw 8.1 Iquique, 1995 Mw 8.0 Colima and 2012 Mw 7.6 Costa Rica earthquakes, the predictions are above the tail end of the observed tsunami run-up distribution. These results provide another indication that breaking the outer wedge greatly affects the tsunami potential. We conclude that a combination of the outer-wedge width and earthquake moment magnitude constitutes a useful basis to produce quantitative predictions of

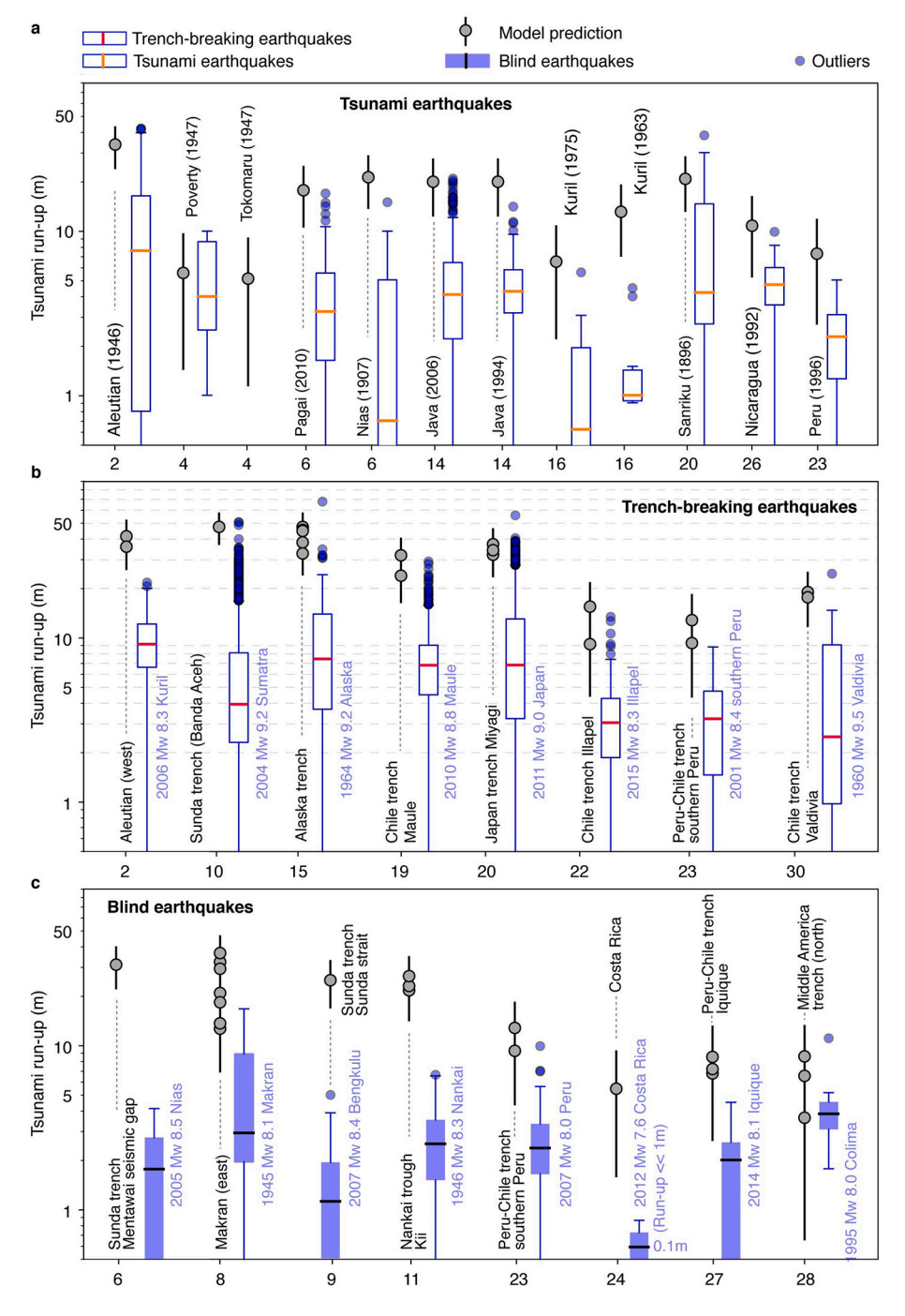


Fig. 14. Comparison between predicted and observed maximum tsunami run-up for a) tsunami earthquakes, b) great or giant trench-breaking earthquakes, and c) blind earthquakes. The numbers on the horizontal axis show the descending order of the outer wedge width of subduction zones (Fig. 20). The boxplots illustrates the statistical distribution of tsunami run-up measurements for each event: The middle bar shows the median run-up with the lower and top whisker show quartiles. The dots beyond thesewhiskers indicate outliers under Tukey's definition. Error bars (one sigma) show our model predictions. We provide multiple predictions in places where the outer wedge width varies drastically along strike. See also Table S3 and S4.

maximum tsunami run-up at subduction zones.

5. Implications for tsunami hazard at remaining seismic gaps

As the correlation with outer-wedge width provides useful estimates of maximum runup for tsunamis triggered by tsunami earthquakes and trench-breaking ruptures within a wide range of moment magnitudes, we survey the morphology of global subduction zones to shed light on

tsunami hazards at remaining seismic gaps. We conduct structural analyses of the Hikurangi, Makran, Lesser Antilles (Fig. S3), Sumatran (Fig. S4 and S5), Nankai (Fig. S7), Ryukyu (Fig. S6), Aleutian (Fig. S9), Cascadia, Northeast Japan (Fig. S8), Chile (Figs. S15, S16, and S17), Colombian (Fig. S13), Manila, Middle-American (Figs. S10, S11, and S12), and Peruvian (Fig. S14) subduction zones based on available seismic profiles. Several parallel profiles across the Makran, Sunda, and Nankai trenches document lateral variations of outer wedge geometry.

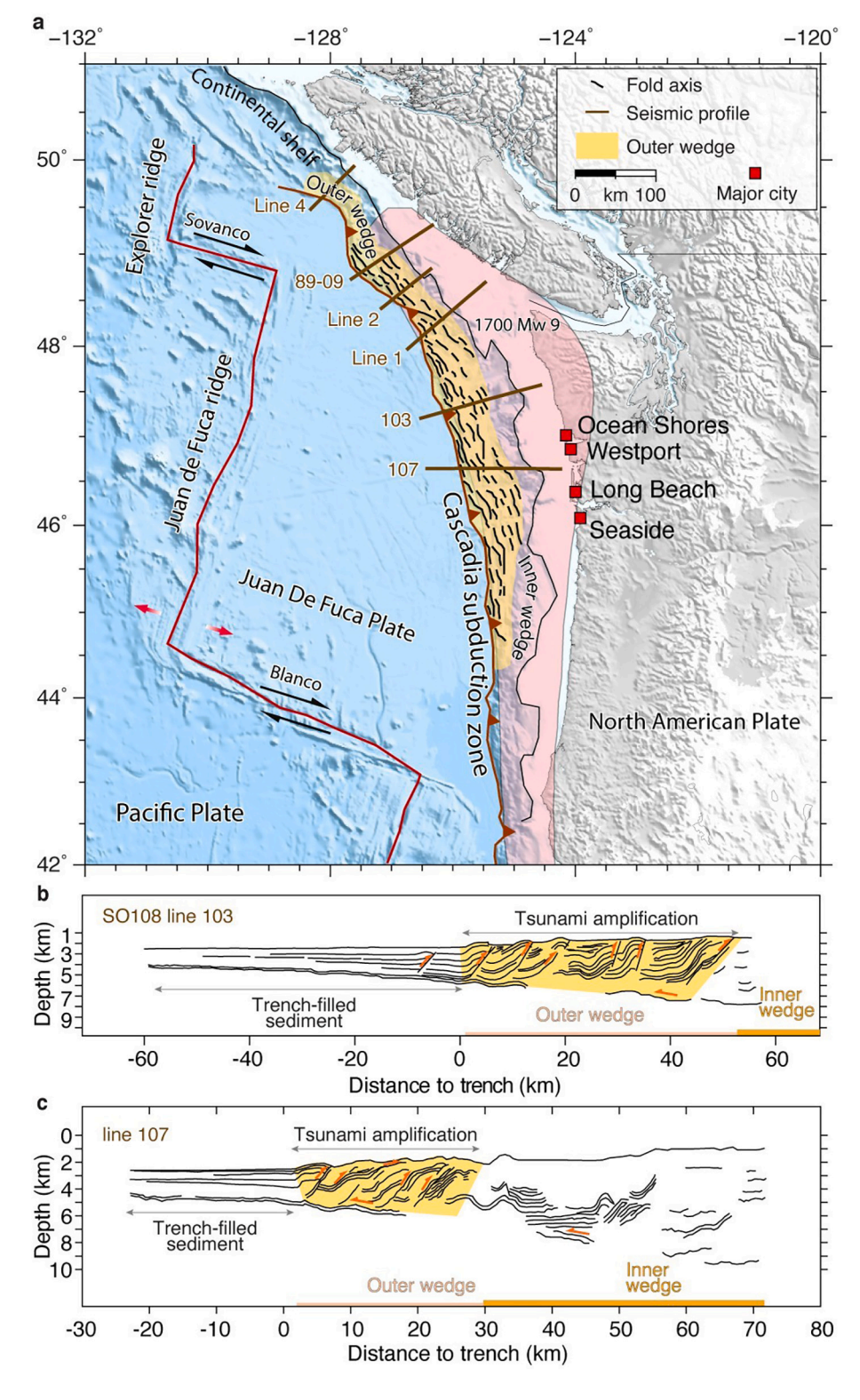


Fig. 15. Tectonic background, estimated 1700 Mw 9 earthquake rupture, and representative seismic profiles in the Cascadia subduction zone. a) Map view of seismic profiles location, outer wedge width, and major potentially impacted cities. Colored area with labels show the historical earthquake ruptures [Satake et al., 2003]. The seismic profiles include Lines 1, 2, and 4 [Davis and Hyndman, 1989] and 89–09 [Clowes et al., 1997]. b) and c) Seismic profiles from *Line 103* and *Line 107* [Flueh et al., 1998], respectively.

All the interpreted profiles are summarized in Fig. 13, but we provide more details for the subduction zones with high run-up potential exposing large coastal populations: the Cascadia subduction zone offshore the Pacific Northwest, the Makran subduction zone offshore Iran and Pakistan, the Sunda and Manila trenches in Southeast Asia, and the Nankai Trough in Southwest Japan.

5.1. Cascadia subduction zone

The Cascadia subduction zone is an accretionary margin at the boundary between the Juan de Fuca and the North American plates exposing the states of Oregon, Washington, and British Columbia to a potentially giant megathrust earthquake [Goldfinger et al., 2003a, 2003b], perhaps similar to the 1700 Mw 9 rupture [Satake et al., 2003]. The structure of the shallow subduction zone is determined by numerous seismic profiles [e.g., Flueh et al., 1998; Davis and Hyndman, 1989;

Clowes et al., 1997]. The outer wedge of the accretionary prism is characterized by a series of seaward, mixed, and landward-vergent steeply dipping thrusts [Watt and Brothers, 2020].

As representative examples, we focus on Lines 103 and 107 [Flueh et al., 1998] that show a stack of imbricate landward-vergent thrusts in the shallow section (Fig. 15). The presence of seabed scarps and inclined sedimentary strata and folds indicate active deformation and delineate the outer wedge. Based on seismic horizons and bathymetry, we estimate an outer-wedge width of \sim 43 km for Line 103 and of \sim 25 km for Line 107 (Fig. 15 and Table S3). These dimensions correspond to a maximum run-up along the coast of the Pacific Northwest between \sim 25 m and \sim 70 m for a hypothetical Mw 9.0 earthquake. The range is consistent with the most likely and the maximum possible run-up, respectively, predicted by inundation models based on a range of earthquake rupture scenarios [e.g., Witter et al., 2013].

Our model implies along-strike variations of tsunami run-up based

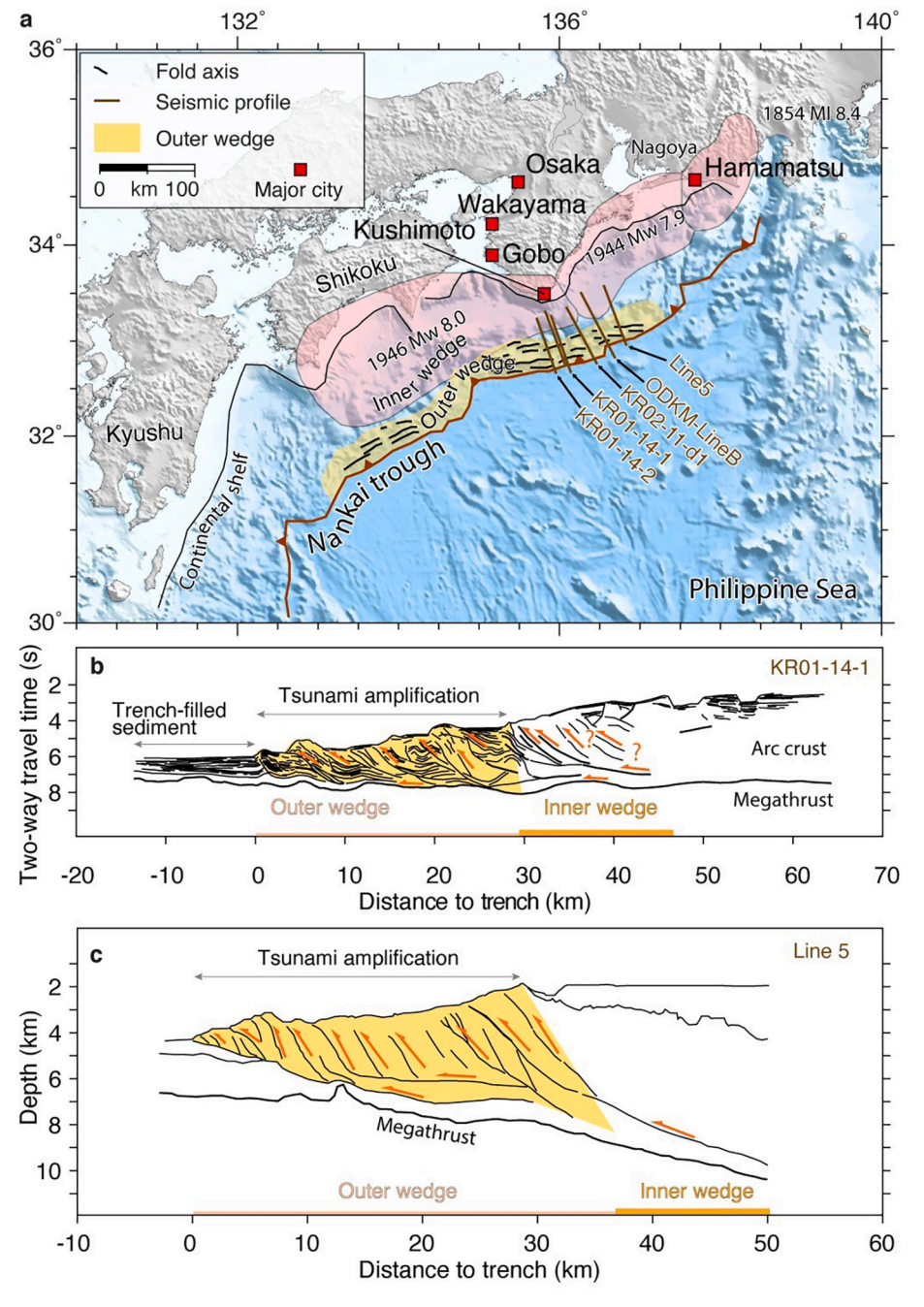


Fig. 16. Tectonic background, estimated 1946, 1944 and 1854 earthquake ruptures and representative seismic profiles in the Nankai Trough. a) Map view of seismic profiles location and inferred outer wedge dimension. Colored area with labels show the historical earthquake ruptures. b) and c) Interpretation of representative seismic structures, also shown in Fig. 13. The seismic profiles include KR01–14-1, KR01–14-2, and ODKM-LineB [Tsuji et al., 2015], and Line 5 [Park et al., 2002; Kamei et al., 2012].

on the evolving structure of the outer wedge that may help refine deterministic scenarios of rupture propagation and tsunami excitation. It is possible that the rupture of numerous splay faults in the outer wedge during trench-breaking earthquakes is more commonplace than previously thought, with important implications for tsunami run-up. In that case the current hazard map including inundation distance, flow depth, current speed, and maximum wave height may need to be refined to make large run-up a more likely scenario. This is particularly crucial for coastal cities, e.g., Ocean Shores, West port, Long Beach, and Seaside that are exposed to local tsunamis and to those triggered by distant earthquakes.

5.2. Nankai Trough

The Nankai Trough in Southwest Japan is an accretionary margin

a 116° 120° 112 24 Guangzhou Tsunami energy path Tainan Hong Kona Kaohsiung Macau = 22° MGL0905-23 MGL0905 25A Line 973 20 MCS693-4 MCS693-6 Laoag South China Sea 18 Vigan 1934 Ms 7 1924 Ms 7.0 16 Major city Seismic profile 14 Outer wedge ∃ km 100 200 Fold axis b Tsunami amplification 0 Inner 4 wedge Two-way travel time (s) Megathrust Trench-filled sediment A-A' Outer wedge Trench-filled C Tsunami amplification Inner MGL0905-23 Outer wedge -100 0 50 -50 100 Distance to trench (km)

between the Philippine Sea and the Eurasian plates, which recently ruptured during the $1854\,M_L=8.4\,\mathrm{Tokai},\,1944\,\mathrm{Mw}=8.1\,\mathrm{Tonankai},\,\mathrm{and}\,1946\,\mathrm{Mw}=8.3\,\mathrm{Nankai}$ mega-quakes [Kumagai, 1996]. The structure of the arc is well constrained by seismic profiles [Leggett et al., 1985; Moore et al., 1990; Park et al., 2000; Kodaira et al., 2000; Takahashi et al., 2003; Ito et al., 2009]. We use seismic lines KR01–14-1, KR01–14-2, and ODKM-LineB [Tsuji et al., 2015], and Line 5 [Park et al., 2002; Kamei et al., 2012] as representative examples (Figs. 16 and S6). The shallow structure is spatially coherent, showing sub-parallel seaward-vergent thrusts cutting through the sedimentary strata down to the megathrust within a $\sim\!30\,\mathrm{km}\text{-wide}$ outer wedge.

Our model predicts a maximum run-up between ~ 15 and ~ 25 m, and between ~ 30 to ~ 60 m for hypothetical Mw 8 and Mw 9 earth-quakes, respectively. This range is compatible with the probabilistic tsunami hazard analysis (PTHA), which indicates a maximum tsunami

Fig. 17. Tectonic background, historical earthquake ($Mw \ge 6.8$), and representative seismic profiles in the Manila trench. a) Map view of seismic profiles location, outer wedge, and major cities. Colored area shows the tsunami wave energy path from a hypothetical earthquake rupture, and red circles show the historical earthquakes ($Mw \ge 6.8$) [Qiu et al., 2019a]. b) and c) Interpretations of representative seismic profiles A-A' and MGL0905–23 [Eakin et al., 2014], also shown in Fig. 13. Additional profiles includeLine 973 [Lin et al., 2009], MGL0905-25A [Eakin et al., 2014], and C-C', B-B', J-J', F-F' and E-E' [Hayes and Lewis, 1984]. (For interpretation of the references to colour in this figure legend, the reader is referred to the web version of this article.)

wave height along the Nankai coastline >30 m [Goda et al., 2018]. The difference may come from varying assumptions regarding the shallow rupture propagation. Our model assigns more tsunami excitation potential from the rupture of splay faults in the hanging wall of the outer wedge. The larger predicted tsunami waves are relevant for tsunami hazards at major coastal cities, e.g., Kushimoto, Gobo, Wakayama and Osaka.

5.3. Manila trench

The Manila trench is an eroding margin between the Sunda and the Philippines Sea plate along the Luzon arc and the northwestern Philippines. Geodetic measurements suggest a locked megathrust [Hsu et al., 2012, 2016] and the absence of Mw >7.6 historical megathrust earthquakes suggest a seismic gap. The total length of the Manila subduction zone of \sim 1000 km is similar to the rupture length of the 2004 Mw 9.15 Sumatra-Andaman earthquake [Chlieh et al., 2007]. Tsunami deposits found around the South China Sea [Yang et al., 2018; Sun et al., 2013; Yu et al., 2009] and the western Luzon [Ramos et al., 2017] are

compatible with an ocean-wide tsunami triggered by a giant earthquake at the Manila subduction zone some thousand years ago [Qiu et al., 2019a]. Understanding tsunami hazards on the Manila trench is relevant for many highly populated coastal cities around the South China Sea, e. g., Macau and Hong Kong, Tainan and Kaohsiung, and Laoag and Vigan (Fig. 17).

We use various seismic profiles [Hayes and Lewis, 1984; Lin et al., 2009; Eakin et al., 2014] to characterize the shallow structure of the Manila subduction zone. The outer wedge is characterized by many active high-angle imbricate thrusts revealed by internal deformation and seabed scarps (Fig. 17). The outer wedge of the southern segment (13–19°N) is narrower than in the northern one (19–22°N), corresponding to a variation of the maximum run-up prediction from ~20 to 80 m for a hypothetical Mw 9 earthquake (Fig. 14). Our prediction is larger than previous PTHA results for select offshore hazard points [Nguyen et al., 2014; Li et al., 2016, 2018a]. The difference can be attributed to previous models assuming the rupture of a single splay fault [Qiu et al., 2019a] or only the basal megathrust [Huang et al., 2009]. If more high-angle faults rupture during a trench-breaking

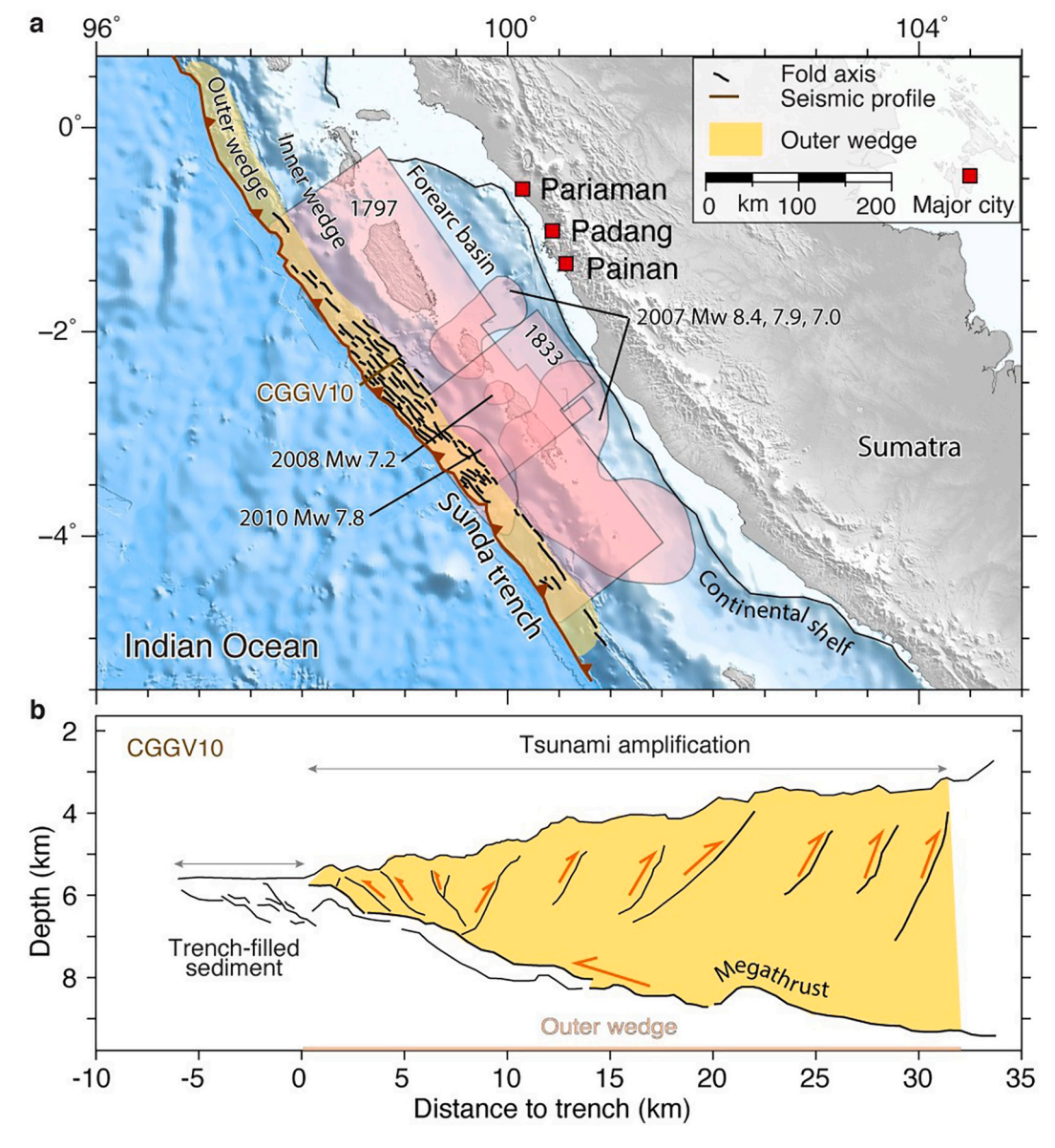


Fig. 18. Tectonic background, historical earthquakes and representative seismic profiles in the Sunda trench. a) Map view of seismic profiles location and inferred dimension of the outer wedge. Colored areas show the extent of the 1797 and 1833 [Natawidjaja et al., 2006], 2007 Bengkulu [Tsang et al., 2016], and the 2010 Mentawai [Hill et al., 2012] earthquakes. b) Interpretation of representative seismic profile CGGV10 [Qin and Singh, 2018], also shown in Fig. 13.

rupture, our run-up prediction may be more appropriate and inundation map for major cities around the South China Sea may need to be refined accordingly. This is especially important for the southern coast of China, where large tsunami wave energy is focused as the effect of the reflection and refraction by the continental slope and shelf [Qiu et al., 2019a; Li et al., 2018b].

5.4. Sunda trench

The Sunda megathrust features a complex recurrence pattern of large earthquakes called seismic super-cycles with highly clustered events separated by a long quiescence period [Sieh et al., 2008]. The megathrust recently broke in a piecemeal fashion, starting with the 2004 Mw 9.2 Sumatra-Andaman earthquake that ruptured the Andaman and Aceh sections, continuing with the 2005 Mw 8.6 Nias-Simeulue, 2007 Mw 8.4 Bengkulu, and 2010 Mw 7.8 Pagai earthquakes to the south [e.g., Qiu et al., 2018]. The Mentawai seismic gap did not yet rupture during the current super-cycle. The seismic profile CGV10 [Qin and Singh, 2018] offshore Padang, Sumatra and the Mentawai Island reveals a mix of seaward- and landward-vergent high-angle thrust faults above the Sunda megathrust along a $\sim\!30$ km-wide outer wedge (Fig. 18), similar to farther south in the epicentral region of the 2010 Mw 7.8 Mentawai

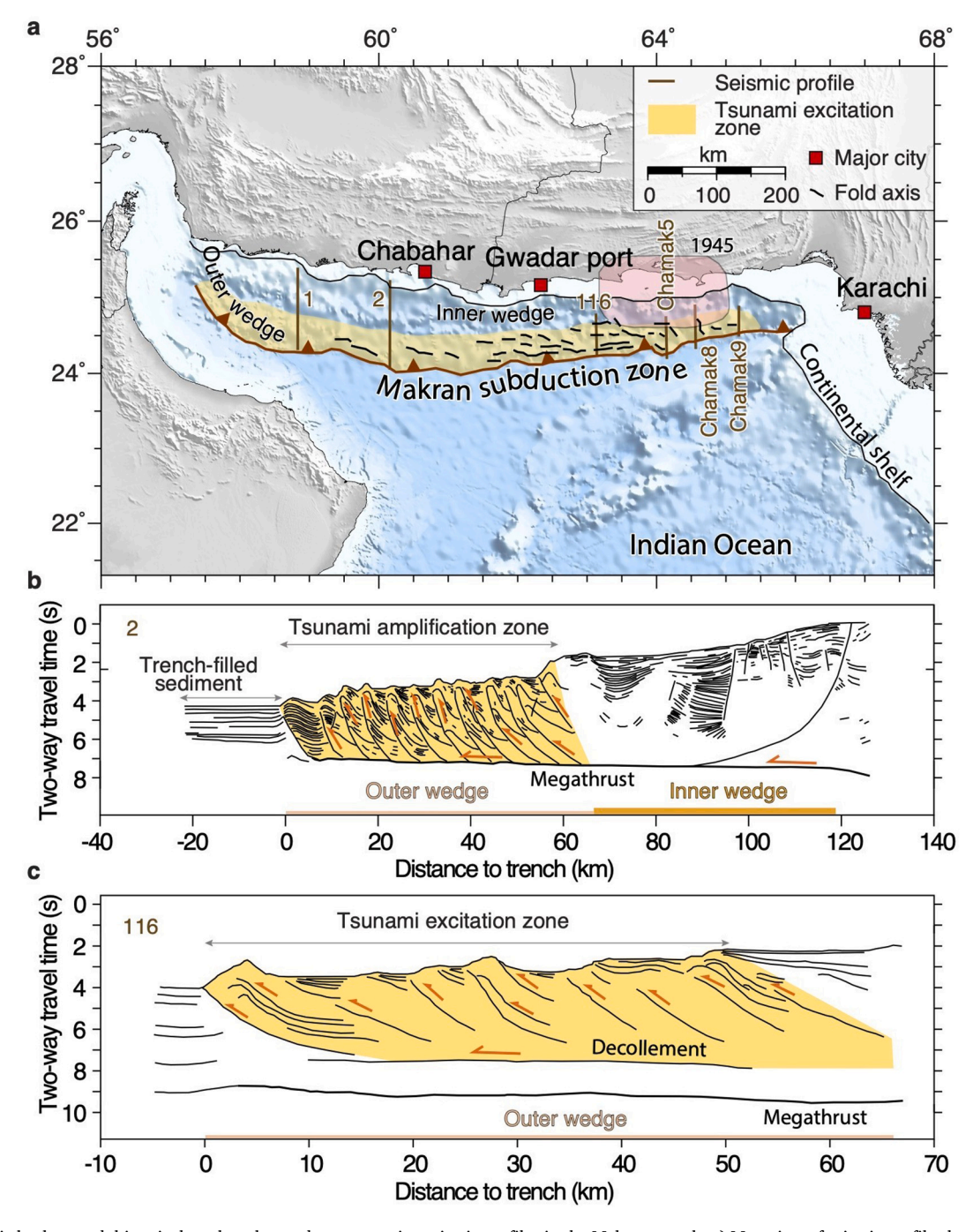


Fig. 19. Tectonic background, historical earthquakes and repres*ent*ative seismic profiles in the Makran trench. a) Map view of seismic profiles location and inferred dimension of the outer wedge. Colored area shows the 1945 historical earthquake rupture [Byrne et al., 1992]. b) and Interpretation of representative seismic profiles 2 Grando and McClay [2007] and 116 Smith et al. [2012], also shown in Fig. 13. Additional available profiles include 1 [Grando and McClay, 2007] and chamak5, 8, and 9 [Ellouz-Zimmermann et al., 2007].

tsunami earthquake (Fig. 4).

Our model predicts \sim 10 m of maximum run-up in the Mentawai segment for a hypothetical Mw 7 tsunami earthquake, slightly smaller than the \sim 16 m run-up of the 2010 Mw 7.8 event, but more than twice that of the 2005 Mw 8.6 Nias-Simeulue blind rupture [Briggs et al., 2006; Borrero et al., 2011]. Historically, the Mentawai segment ruptured in the 1797 Mw 8.5–8.7 and the 1833 Mw 8.6–8.9 great earthquakes, resulting in >5 m and > 3–4 m run-up, respectively [Natawidjaja et al., 2006]. For hypothetical Mw 8 and Mw 9 earthquakes in this segment, the model predicts a maximum run-up of \sim 15–30 m and \sim 50 m in the coastal area, respectively. It is possible that the 1797 and 1833 events were blind ruptures, similar to the 2005 Mw

8.6 Nias-Simeulue earthquake [Briggs et al., 2006; Qiu et al., 2019b], explaining their lower run-up. If the next Mw 8+ earthquake of the Mentawai seismic gap is trench-breaking, the deformation of the outer wedge may create larger tsunami waves than the recent blind earthquakes have produced. Adjusting the PTHA accordingly may be important to mitigate tsunami hazard in the major coastal cities of Padang, Pariaman, and Painan.

5.5. Makran subduction

The Makran subduction zone accommodates the relative motion between the Arabian and Eurasian plates exposing the coast of Iran and

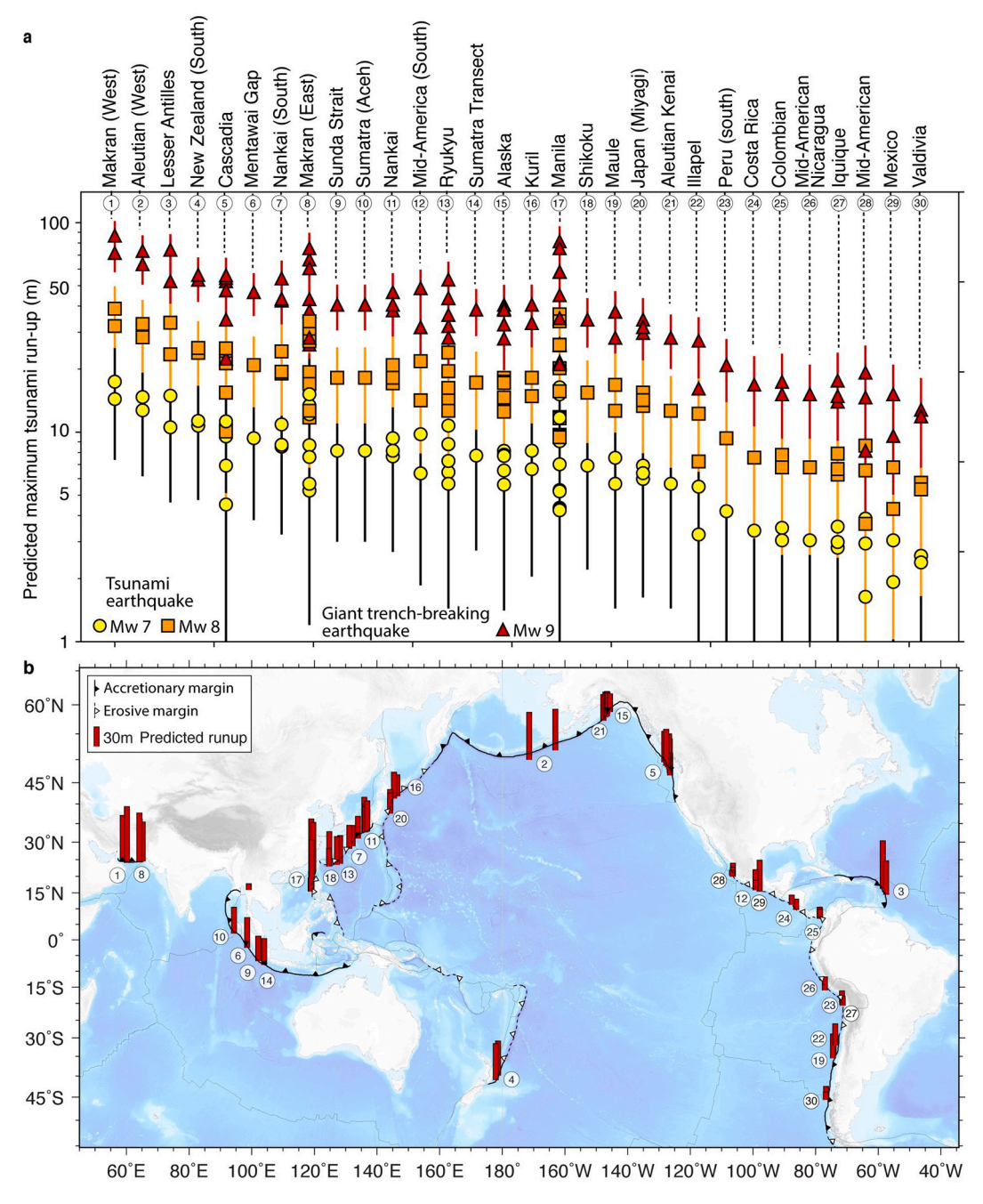


Fig. 20. Maximum run-up prediction based on hypothetical tsunami earthquakes (yellow circles for Mw 7 and orange squares for Mw 8) and Mw 9 trench-breaking earthquakes (red triangles) at global subduction zones based on Eq. 1. a) Run-up prediction at global subduction zones organized by descending order of the outer wedge width. The representative seismic profile used to estimate the outer wedge width for each region is given in Fig. 13 and Table S4. b) The maximum run-up prediction from a hypothetical Mw 9 trench-breaking earthquake at global subduction zones in map view (red triangles in a)). The numbers are the same in a). (For interpretation of the references to colour in this figure legend, the reader is referred to the web version of this article.)

Pakistan to seismic and tsunami hazards. Historical earthquake and tsunami records date back to 326 BCE [Heidarzadeh et al., 2008], the most recent event being the 1945 Mw 8.2 earthquake [Heidarzadeh and Satake, 2017] that caused >4000 casualties and generated ~12–13 m tsunami waves along the Pakistan coastline [Heidarzadeh and Satake, 2015]. The Makran subduction zone developed one of the widest (>400 km) accretionary wedge of all subduction zones [Kopp, 2002; Schlüter et al., 2002]. The thick sediment cover of >7 km hosts many imbricate thrusts and folds within a remarkably wide (~55–70 km) outer wedge (Fig. 19). Accordingly, our model associates among the highest run-up potential worldwide (Fig. 14). Overall, the width of the outer wedge in the west segment offshore Iran is slightly larger than that of the eastern segment offshore Pakistan, but the latter exhibit significant variation along strike. This results in a large range of run-up prediction for a given earthquake magnitude (Fig. 14c).

Our model predicts a maximum run-up between ~12 m to 40 m for a hypothetical Mw 8 earthquake in eastern Makran, essentially covering the wave height range triggered by the 1945 event or estimated maximum wave height range from the conventional PTHA analysis [Hoechner et al., 2016; Rashidi et al., 2020]. The Makran subduction is currently locked, no major earthquake with Mw >7 having occurred since 1945, and the corresponding accumulated strain may rupture as Mw 8–9 earthquakes [Lin et al., 2015; Smith et al., 2013; Sultan and Ahmed, 2017; Penney et al., 2017]. For a hypothetical Mw 9 trenchbreaking earthquake, the model implies a maximum run-up between 28 and 80 m. This prediction can help mitigate tsunami hazard in the major coastal cities or ports, i.e., Chabahar, Gwadar, and Karachi.

5.6. Global subduction zones

The survey of outer wedge geometry at global subduction zones reveals a wide range of outer wedge widths from ~5 to 90 km (Fig. 13), associated with correspondingly widely different tsunami hazards from potential tsunami earthquakes and trench-breaking ruptures. Adopting the empirical relationship between outer-wedge width, seismic moment, and maximum tsunami run-up of trench-breaking ruptures (Eq. (1)), we obtain an assessment of tsunami hazard at global subduction margins (Fig. 20). Given a local configuration of the outer wedge, the tsunami potential of future seismicity depends chiefly on the type of rupture, i.e., trench-breaking or blind. Large-magnitude (7.0≤Mw≤8.2) trenchbreaking ruptures are tsunami earthquakes with a tsunami excitation potential controlled dominantly by the width of the outer wedge. We provide an estimate for hypothetical Mw 7.0 and Mw 8.0 tsunami earthquakes at subduction margins. The run-up caused by giant (8.2 \le Mw \le 9.5) trench-breaking ruptures depends also on the actual seismic moment. We offer an estimate of tsunami run-up for a hypothetical Mw 9 trench-breaking rupture. The actual seismic moment of future ruptures depend on their capacity to propagate up-dip into the outer wedge and to break contiguous along-trench segments, which cannot be predicted based on current knowledge. The predicted maximum tsunami run-up depends on the outer wedge width, which is most developed at the Western Makran, Aleutian, Lesser Antilles, Southern Hikurangi and Cascadia trenches, with estimates varying overall from 10 to 100 m for Mw 9.0 earthquakes and from 1 to 40 m for tsunami earthquakes. The Mentawai section of the Sunda megathrust, eastern Makran, Ryukyu, and Manila trench have a smaller outer wedge, implying estimated tsunami run-up between 4 and 20 m for tsunami earthquakes. Subduction margins with a poorly developed outer wedge, such as the Middle-American, Nicaraguan, Colombian, and North Chilean trenches, are associated with the lowest tsunami run-up predictions. However, each subduction margin exhibits lateral variations in outer wedge structure implying great variability of tsunami hazards along trenches. For example, the outer wedge varies between ~16 and 43 km width in Cascadia, implying run-up between ~4 and 70 m depending on the source location and the magnitude of the earthquake.

6. Discussion

Several forms of structural control of tsunami excitation have been tested [Satake and Tanioka, 1999], including the incoming seafloor roughness, the sediment vertical thickness in the outer wedge and frontal prism, and the accretionary versus erosive nature of sedimentary prisms [Geersen, 2019]. However, the vertical thickness of the outer wedge may not be a systematic controlling factor for tsunami excitation [Geersen, 2019]. The efficiency of seafloor uplift depends on the presence of high-angle faults, not on how thick a sediment layer they cross. In contrast, the total coseismic slip on activated faults for a given stress drop is controlled by the down-dip width of rupture [Kanamori and Anderson, 1975] and slip amplitude may be continuous between the basal décollement and the overlying splay faults. This implies that the width of the outer wedge is a more relevant factor than its vertical thickness. Tsunami earthquakes have also been associated with subducted seamounts [Abercrombie et al., 2001; Bell et al., 2010]. However, several other types of subducted seafloor features — horsts, grabens, ridges, abyssal hills, and fracture zones — can deform the base of the outer wedge. In principle, any morphological gradient at the plate interface may be associated with permanent deformation of the overlying sediment by folding or faulting, creating a network of fractures in the hanging wall [Wang and Bilek, 2011]. Additional deformation comes from shortening of sediment as is typical in thrust-and-fold belts, creating splay faults that provide additional pathways for rupture propagation to the seafloor with more efficient tsunami excitation than slip on the basal décollement [Hubbard et al., 2015; Bradley et al., 2019].

Wider outer wedges are often found at accretionary margins where the convergence is slow and the incoming sediment input is high, for example at the Makran, Cascadia, and Hellenic subduction zones [Clift and Vannucchi, 2004; von Huene et al., 2009; Scholl et al., 2015; Seno, 2017]. Conversely, subduction zones with a fast convergence and a limited sediment supply often result in a poorly-developed sediment prism and thus a narrower outer wedge. These relationships imply a tectonic control on the size of tsunami earthquakes and tsunami excitation. For example, the smallest magnitude tsunami earthquakes with the lowest maximum tsunami run up — the 1963 Mw 7.8 and 1975 Mw 7.5 Kuril, 1960 Mw 7.5 Peru, and the 1992 Mw 7.7 Nicaragua tsunami earthquakes — occurred at erosive margins (Fig. 1). However, the 1896 Mw 8.0 Sanriku tsunami earthquake at an erosive margin is a notable exception, as it produced some of the largest tsunami run up ever observed. Tsunami earthquakes in fact occur at both erosive and accretionary margins. A similar conclusion can be drawn for giant, trench-breaking earthquakes with outsize tsunami waves. While a majority of these ruptures occurred at accretionary margins, like for the 1964 Mw 9.2 Alaska earthquake, some occur at erosive margins, like the 2011 Mw 9.1 Tohoku earthquake.

The accretionary versus erosive nature of subduction zones therefore provides only limited quantitative predictive power of tsunami excitation. Although the largest outer wedges are most often found at accretionary margins and the narrowest ones at erosive margins, there are notable exceptions (Fig. 13). For example, some of the largest outer wedges are found along the Manila and Luzon erosive margins. Conversely, a narrow outer wedge can be found along the Cascadia and Eastern Makran accretionary margins. Erosive or accretionary margins reflect a deficit or surplus of sediment flux, respectively, not directly the size of the outer wedge and the presence of active faults in the handing wall. As outer-wedge width can vary greatly among or along trenches, a more useful approach is to directly image the structural layout based on seismic profiles and high-resolution bathymetry.

Our proposed model for tsunami excitation provides new insights to help mitigate tsunami hazards at global subduction zones. First, we highlight that the cradle of tsunami earthquakes is the outer wedge of the sedimentary prism where many active structures — faults and folds — provide an efficient seafloor vertical displacement mechanism during

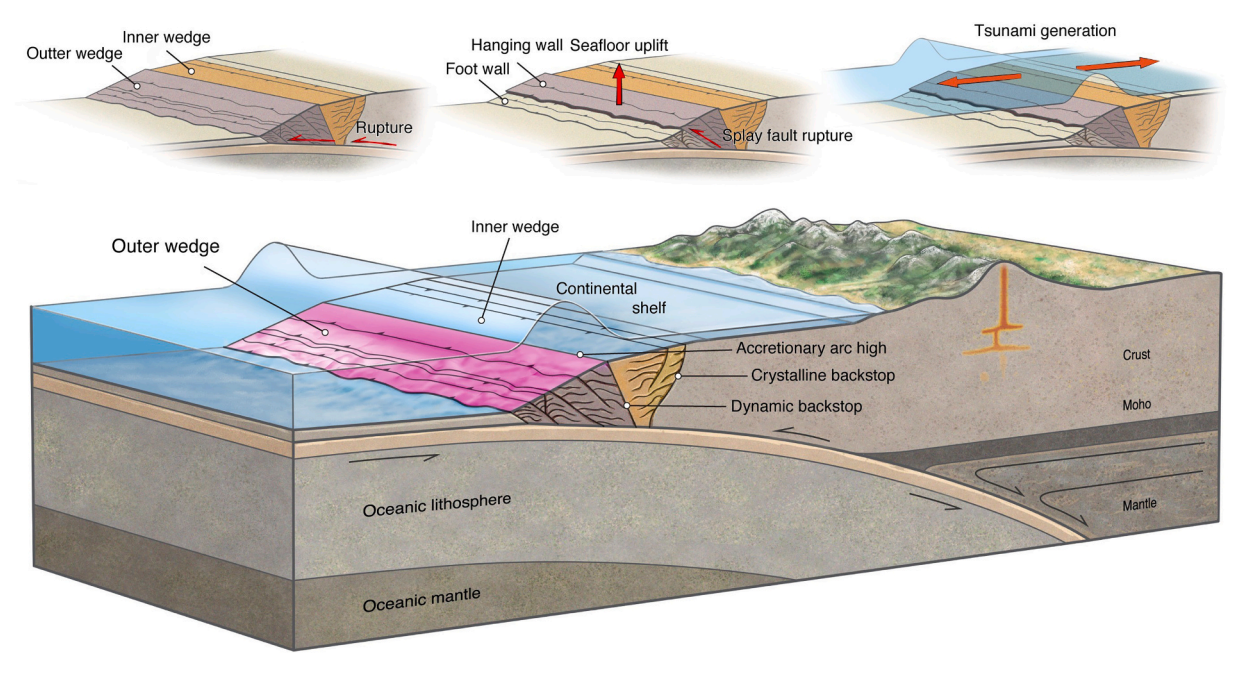


Fig. 21. Conceptual model of tsunami excitation in the outer wedge of the accretionary prism at subduction margins. The yellow area represents the inner wedge bounded by the dynamic and crystalline backstops and characterized by subhorizontal sediment bedding planes. The pink area consists of many foreward-, or bi-vergent thrust and folds, forming potential pathways for rupture propagation, large seafloor vertical displacement, and efficient tsunami excitation. (For interpretation of the references to colour in this figure legend, the reader is referred to the web version of this article.)

seismic ruptures. Empirical power-law relationships between outer wedge width, maximum tsunami run-up, and tsunami earthquake moment magnitude provide simple but rapid estimates of expected maximum tsunami run-up that can be used for a tsunami early warning if the structure of the outer wedge is well established. Numerical modeling of tsunami propagation can also be used to assess run-up, but these calculations can be time consuming, wasting precious time for early-warning and decision making in a possible crisis situation. Second, our predictions of the maximum tsunami run-up associated with giant, trench-breaking ruptures can inform the design of coastal infrastructure for long-term mitigation of tsunami hazards. Evacuation routes and flood zones should extend horizontally to the topographic contour line standing above the anticipated maximum run-up height. The maximum tsunami run-up can be obtained from Eq. (1) by considering a hypothetical giant earthquake, for example, of moment magnitude 9.0, and incorporating the structural layout of the outer wedge along the margin. Remarkable differences in maximum tsunami-height predictions arise between narrow, e.g., along the Mid-American and N. Chile trenches, and wide, e.g., the Makran, Aleutian, Lesser Antilles, and Cascadia, margins, with peak waves of about 20 and 100 m, respectively. There remains fundamental uncertainties about the exact earthquake magnitude a particular subduction zone can expect and when such event is likely to occur. However, the 2004 Mw 9.2 Sumatra-Andaman and 2011 Mw 9.1 Tohoku-Oki mega-quakes have shown the potential of seismic ruptures to propagate to the trench and to extend laterally across multiple segments, which could occur at other subduction zones.

Conceptual models of subduction zone seismicity must evolve to incorporate the complexity of fault networks in the outer wedge and aim for more specific descriptions of frontal deformation than generic terms such as "plastic deformation", "damage", or "compliant zone" near the trench. The structure of accretionary prisms is readily described by seismic profiles at virtually all major subduction zones. These surveys reveal networks of imbricate, conjugate, forward-, backward- or bivergent high-angle faults and associated folding of the thrusted sediment that produce more efficient seafloor deformation than coseismic slip along the basal décollement. Currently available data are sufficient to draw a simple scenario of tsunami excitation in the outer wedge

(Fig. 21) whereby rupture propagation along one or several of these structures is responsible for the triggering of exceptionally large tsunami waves.

Future efforts in rupture dynamics and tsunami modeling should incorporate the effect of faulting and folding in the outer wedge. Further improvement in prediction of seismic and tsunami hazards will necessitate three-dimensional imaging of the outer wedge to better understand the rupture pathway from the megathrust to hanging wall faults. An important remaining unknown is the structural and rheological controls on up-dip rupture propagation that turns blind ruptures into giant, trench-breaking earthquakes. A related challenge is understanding the nucleation and propagation of ruptures within the complex setting of the frontal accretionary wedge and shallow megathrust.

7. Conclusions

Tsunami earthquakes occur in the complex structural setting of the outer wedge of accretionary prisms at subduction zones. The presence of active deformation structures off the plate interface allows rupture propagation on high-angle faults that displace the seafloor more effectively than slip on the shallow dipping décollement. Active faults of the outer wedge include forward-, backward-, and bi-vergent thrusts permitting shortening and accretion as well as normal faults that accompany gravitational collapse. Additional seafloor deformation may occur due to folding, presumably accommodated by flexural slip along active axial surfaces. As shortening in the hanging wall reduces the longterm slip on the plate interface, the frequency of tsunami earthquakes that accommodate this motion on the shallow décollement is lower than that of deeper earthquakes with a similar moment magnitude. Furthermore, slip on high-angle faults within a low-rigidity sediment matrix may explain the unusual characteristics of tsunami earthquakes with slow rupture propagation and low stress drop, yet high potency density and relatively large seafloor displacements. These effects may be further amplified by the characteristically steep seafloor slopes of the outer wedge that can transfer horizontal motion to vertical displacements of the seafloor.

The structure of the outer wedge controls the tsunamigenic potential

of tsunami earthquakes and larger trench-breaking ruptures. At first order, the wider the outer wedge, the stronger the tsunami excitation. A power-law relationship with seismic moment and outer-wedge width (Eq. 1) allows us to predict the maximum tsunami run-up of tsunami earthquakes and giant, trench-breaking ruptures at any particular segments of subduction zones based on the characteristics of the outer wedge. These empirical relationships can form the basis of tsunami hazard mitigation by providing rapid estimates of floods caused by a seismically triggered tsunami. Estimates of tsunami run-up should be particularly useful at subduction zones where paleoseismic data indicate a seismic gap.

Further concerted efforts are required to grapple with the scourge of the Pacific. Better understanding of seismic and tsunami hazards at subduction margins will necessitate more detailed seismic imaging of the outer wedge to delineate the three-dimensional extent of active deformation structures and their mechanical connection with the basal décollement. Numerical simulations of seismic and tsunami cycles should resolve the mechanical complexity of shallow accretionary prisms to better constrain the dynamics of tsunami excitation. Further experimental studies of the mechanical properties of faults and soft sediment deformation are needed to elucidate the conditions for nucleation and rupture propagation in the fluid-rich, low-temperature, and low-strength environment of the outer wedge. Nevertheless, the key to unlock the mechanics of tsunami excitation at subduction zones will reside at the interface between structural geology and rock mechanics.

Data availability

The structural data presented in Fig. 13 is available in digital format at the DOI https://doi.org/10.5281/zenodo.5854751. The topography is from Ryan et al. [2009]. The finite slip distributions are from Hayes [2017]. Our analyzed data sets in this study are given in the supplementary document.

Author contributions

QQ and SB designed the study, gathered the data, and wrote the manuscript.

Declaration of Competing Interest

The authors declare no competing financial or non-financial interests.

Acknowledgments

QQ and SB are supported by the funding from the National Science Foundation, under award number EAR-1848192. QQ is also supported by grants from the National Natural Science Foundation of China (42076059, 41890813, 41976066, 41976064), the Key Special Project for Introduced Talents Team of Southern Marine Science and Engineering, Guangdong Laboratory (Guangzhou) (GML2019ZD0205), Chinese Academy of Sciences (Y4SL021001, QYZDY-SSW-DQC005, 133244KYSB20180029, ISEE2021PY03, 131551KYSB20200021), The Guangdong Provincial Research and Development Program in key areas (2020B1111520001) and China-Pakistan Joint Research Center on Earth Sciences. We are very grateful for the three anonymous reviewers' comments that greatly improved our manuscript. We also thank chief editor Prof. Gillian Foulger for her kindness and patience when processing our manuscript.

Appendix A. Supplementary data

Supplementary data to this article can be found online at https://doi.org/10.1016/j.earscirev.2022.104054.

References

- Abe, K., 1979. Size of great earthquakes of 1837–1974 inferred from tsunami data. J. Geophys. Res. Solid Earth 84 (B4), 1561–1568.
- Abe, K., 1994. Instrumental magnitudes of historical earthquakes, 1892 to 1898. Bull. Seismol. Soc. Am. 84 (2), 415–425.
- Abercrombie, R.E., Antolik, M., Felzer, K., Ekstrom, G., 2001. The 1994 java tsunami earthquake: Slip over a subducting seamount. J. Geophys. Res. Solid Earth 106 (B4), 6595–6607
- Ammon, C.J., et al., 2005. Rupture process of the 2004 Sumatra-Andaman earthquake. Science (New York, N.Y.) 308 (5725), 1133–1139. https://doi.org/10.1126/science.1112260.
- Ammon, C.J., Kanamori, H., Lay, T., Velasco, A.A., 2006. The 17 July 2006 Java tsunami earthquake. Geophys. Res. Lett. 33 (24).
- Araki, E., et al., 2017. Recurring and triggered slow-slip events near the trench at the nankai trough subduction megathrust. Science 356 (6343), 1157–1160.
- Aretusini, S., Meneghini, F., Spagnuolo, E., Harbord, C., Di Toro, G., 2021. Fluid pressurisation and earthquake propagation in the hikurangi subduction zone. Nat. Commun. 12 (1), 1–8. https://doi.org/10.1038/s41467-021-22805-w.
- Barbot, S., 2020. Frictional and structural controls of seismic super-cycles at the Japan trench. Earth Planets Space 72 (63). https://doi.org/10.1186/s40623-020-01185-3.
- Barker, D.H.N., Sutherland, R., Henrys, S., Bannister, S., 2009. Geometry of the Hikurangi subduction thrust and upper plate, North Island, New Zealand. Geochem. Geophys. Geosyst. 10 (2) https://doi.org/10.1029/2008GC002153.
- Barnes, P.M., Nicol, A., Harrison, T., 2002. Late Cenozoic evolution and earthquake potential of an active listric thrust complex above the Hikurangi subduction zone, New Zealand. Geol. Soc. Am. Bull. 114 (11), 1379–1405. https://doi.org/10.1130/0016-7606(2002)114¡1379:LCEAEP¿2.0.CO;2.
- Beeler, N.M., Tullis, T.E., Goldsby, D.L., 2008. Constitutive relationships and physical basis of fault strength due to flash heating. J. Geophys. Res. Solid Earth 113 (1). https://doi.org/10.1029/2007JB004988.
- Behr, W.M., Bürgmann, R., 2021. What's down there? the structures, materials and environment of deep-seated slow slip and tremor. Phil. Trans. R. Soc. A 379 (2193). https://doi.org/10.1098/rsta.2020.0218, 20200,218.
- Bell, R., Sutherland, R., Barker, D.H., Henrys, S., Bannister, S., Wallace, L., Beavan, J., 2010. Seismic reflection character of the Hikurangi subduction interface, New Zealand, in the region of repeated Gisborne slow slip events. Geophys. J. Int. 180 (1), 34-48. https://doi.org/10.1111/j.1365-246X.2009.04401.x.
- Bilek, S.L., Engdahl, E.R., 2007. Rupture characterization and aftershock relocations for the 1994 and 2006 tsunami earthquakes in the java subduction zone. Geophys. Res. Lett. 34 (20).
- Bilek, S.L., Lay, T., 1999. Rigidity variations with depth along interplate megathrust faults in subduction zones. Nature 400 (6743), 443–446. https://doi.org/10.1038/ 22729
- Bilek, S.L., Lay, T., 2018. Subduction zone megathrust earthquakes. Geosphere 14 (4), 1468–1500.
- Blanpied, M.L., Lockner, D.A., Byerlee, J.D., 1991. Fault stability inferred from granite sliding experiments at hydrothermal conditions. Geophys. Res. Lett. 18 (4), 609–612. https://doi.org/10.1029/91GL00469.
- Blanpied, M.L., Lockner, D.A., Byerlee, J.D., 1995. Frictional slip of granite at hydrothermal conditions. J. Geophys. Res. 100 (B7), 13,045–13,064. https://doi. org/10.1029/95JB00862.
- Borrero, J.C., et al., 2011. Field survey of the March 28, 2005 Nias-Simeulue earthquake and Tsunami. Pure Appl. Geophys. 168 (6–7), 1075–1088. https://doi.org/10.1007/s00024-010-0218-6.
- Boston, B., Moore, G.F., Nakamura, Y., Kodaira, S., 2017. Forearc slope deformation above the Japan Trench megathrust: Implications for subduction erosion. Earth Planet. Sci. Lett. 462, 26–34. https://doi.org/10.1016/j.epsl.2017.01.005.
- Bradley, K., et al., 2019. Stratigraphic control of frontal décollement level and structural vergence and implications for tsunamigenic earthquake hazard in Sumatra, Indonesia. Geochem. Geophys. Geosyst. 20 (3), 1646–1664.
- Brantut, N., Schubnel, A., Rouzaud, J.-N., Brunet, F., Shimamoto, T., 2008. High-velocity frictional properties of a clay-bearing fault gouge and implications for earthquake mechanics. J. Geophys. Res. 113 (B10401), 18. https://doi.org/10.1029/ 2007 IB005551
- Briggs, R.W., et al., 2006. Deformation and Slip along the Sunda Megathrust in the Great 2005 Nias-Simeulue Earthquake. Science 311 (5769), 1897–1901. https://doi.org/ 10.1126/science.1122602.
- Brodsky, E.E., Kanamori, H., 2001. Elastohydrodynamic lubrication of faults. J. Geophys. Res. Solid Earth 106 (B8), 16,357–16,374.
- Bürgmann, R., 2018. The geophysics, geology and mechanics of slow fault slip. Earth Planet. Sci. Lett. 495, 112–134.
- Byrne, D.E., Sykes, L.R., Davis, D.M., 1992. Great thrust earthquakes and aseismic slip along the plate boundary of the Makran subduction zone. J. Geophys. Res. 97 (B1), 449–478. https://doi.org/10.1029/91JB02165.
- Chapman, J.B., Elliott, J., Doser, D.I., Pavlis, T.L., 2014. Slip on the suckling hills splay fault during the 1964 Alaska earthquake. Tectonophysics 637, 191–197.
- Chlieh, M., et al., 2007. Coseismic slip and afterslip of the great Mw 9.15 Sumatra-Andaman earthquake of 2004. Bull. Seismol. Soc. Am. 97 (1A), S152–S173. https://doi.org/10.1785/0120050631.
- Choi, B., Min, B., Pelinovsky, E., Tsuji, Y., Kim, K., 2012. Comparable analysis of the distribution functions of runup heights of the 1896, 1933 and 2011 japanese tsunamis in the sanriku area. Nat. Hazards Earth Syst. Sci. 12 (5), 1463.
- Clift, P., Vannucchi, P., 2004. Controls on tectonic accretion versus erosion in subduction zones: implications for the origin and recycling of the continental crust. Rev. Geophys. 42 (2).

Earth-Science Reviews 230 (2022) 104054

Clowes, R.M., Baird, D.J., Dehler, S.A., 1997. Crustal structure of the cascadia subduction zone, southwestern British columbia, from potential field and seismic studies. Can. J. Earth Sci. 34 (3), 317–335.

O. Oiu and S. Barbot

- Condit, C.B., Guevara, V.E., Delph, J.R., French, M.E., 2020. Slab dehydration in warm subduction zones at depths of episodic slip and tremor. Earth Planet. Sci. Lett. 552, 116,601. https://doi.org/10.1016/j.epsl.2020.116601.
- Davis, E., Hyndman, R., 1989. Accretion and recent deformation of sediments along the northern cascadia subduction zone. Geol. Soc. Am. Bull. 101 (11), 1465–1480.
- Dean, S.M., McNeill, L.C., Henstock, T.J., Bull, J.M., Gulick, S.P., Austin, J.A., Bangs, N. L., Djajadihardja, Y.S., Permana, H., 2010. Contrasting décollement and prism properties over the Sumatra 2004-2005 earthquake rupture boundary. Science 329 (5988), 207–210. https://doi.org/10.1126/science.1189373.
- DeDontney, N., Rice, J.R., 2012. Tsunami wave analysis and possibility of splay fault rupture during the 2004 indian ocean earthquake. Pure Appl. Geophys. 169 (10), 1707–1735.
- Di Toro, G., Hirose, T., Nielsen, S., Pennacchioni, G., Shimamoto, T., 2006. Natural and experimental evidence of melt lubrication of faults during earthquakes. Science 311 (5761), 647–649. https://doi.org/10.1126/science.1121012.
- Eakin, D.H., McIntosh, K.D., Van Avendonk, H.J.A., Lavier, L., Lester, R., Liu, C.-S., Lee, C.-S., 2014. Crustal-scale seismic profiles across the Manila subduction zone: the transition from intraoceanic subduction to incipient collision. J. Geophys. Res. Solid Earth 119 (1), 1–17. https://doi.org/10.1002/2013JB010395.
- Eiby, G., 1982. Two New Zealand tsunamis. J. R. Soc. N. Z. 12 (4), 338-351.
- Ellouz-Zimmermann, N., et al., 2007. Offshore frontal part of the makran accretionary prism: the chamak survey (Pakistan). In: Thrust Belts and Foreland Basins. Springer, pp. 351–366.
- Fan, W., Bassett, D., Jiang, J., Shearer, P.M., Ji, C., 2017. Rupture evolution of the 2006 java tsunami earthquake and the possible role of splay faults. Tectonophysics 721, 143–150.
- Flueh, E.R., et al., 1998. New seismic images of the cascadia subduction zone from cruise so108—orwell. Tectonophysics 293 (1–2), 69–84.
- Fournier, T.J., Freymueller, J.T., 2007. Transition from locked to creeping subduction in the shumagin region, alaska. Geophys. Res. Lett. 34 (6) https://doi.org/10.1029/ 2006GL029073.
- Fritz, H.M., et al., 2007. Extreme runup from the 17 july 2006 java tsunami. Geophys. Res. Lett. 34 (12).
- Fryer, G.J., Watts, P., Pratson, L.F., 2004. Source of the great tsunami of 1 april 1946: a landslide in the upper aleutian forearc, Mar. Geol. 203 (3-4), 201–218.
- Fujii, Y., Satake, K., 2006. Source of the july 2006 west java tsunami estimated from tide gauge records. Geophys. Res. Lett. 33 (24).
- Fujiwara, T., Kodaira, S., No, T., Kaiho, Y., Takahashi, N., Kaneda, Y., 2011. The 2011 Tohoku-Oki Earthquake: Displacement Reaching the Trench Axis. https://doi.org/ 10.1126/science.1211554.
- Fujiwara, T., dos Santos Ferreira, C., Bachmann, A.K., Strasser, M., Wefer, G., Sun, T., Kanamatsu, T., Kodaira, S., 2017. Seafloor displacement after the 2011 tohoku-oki earthquake in the northern Japan trench examined by repeated bathymetric surveys. Geophys. Res. Lett. 44 (23), 11–833.
- Fukao, Y., 1979. Tsunami earthquakes and subduction processes near deep-sea trenches. J. Geophys. Res. Solid Earth 84 (B5), 2303–2314.
- Gao, X., Wang, K., 2017. Rheological separation of the megathrust seismogenic zone and episodic tremor and slip. Nature 543 (7645), 416–419. https://doi.org/10.1038/ nature21389.
- Geersen, J., 2019. Sediment-starved trenches and rough subducting plates are conducive to tsunami earthquakes. Tectonophysics 762, 28–44. https://doi.org/10.1016/j. tecto.2019.04.024.
- Geist, E.L., 2002. Complex earthquake rupture and local tsunamis. J. Geophys. Res. Solid Earth 107 (B5). https://doi.org/10.1029/2000JB000139. ESE-2.
- Geist, E.L., Oglesby, D.D., 2014. Earthquake mechanism and seafloor deformation for tsunami generation. In: Encyclopedia of Earthquake Engineering. Springer Berlin Heidelberg, pp. 1–17. https://doi.org/10.1007/978-3-642-36197-5, 296–1.
- Goda, K., Yasuda, T., Mai, P.M., Maruyama, T., Mori, N., 2018. Tsunami simulations of mega-thrust earthquakes in the nankai-tonankai trough (Japan) based on stochastic rupture scenarios. Geol. Soc. Lond., Spec. Publ. 456 (1), 55–74.
- Goldfinger, C., Nelson, C.H., Johnson, J.E., 2003a. Deep-water turbidites as Holocene earthquake proxies: the Cascadia subduction zone and northern San Andreas fault systems. Ann. Geophys. 46 (5) https://doi.org/10.4401/ag-3452.
- Goldfinger, C., Nelson, C.H., Johnson, J.E., Shipboard Scientific Party, 2003b. Holocene earthquake records from the cascadia subduction zone and northern san andreas fault based on precise dating of offshore turbidites. Annu. Rev. Earth Planet. Sci. 31 (1), 555–577.
- Grando, G., McClay, K., 2007. Morphotectonics domains and structural styles in the makran accretionary prism, offshore Iran. Sediment. Geol. 196 (1–4), 157–179.
- Hananto, N., et al., 2020. Tsunami earthquakes: Vertical pop-up expulsion at the forefront of subduction megathrust. Earth Planet. Sci. Lett. 538, 116,197.
- Hayes, G.P., 2017. The finite, kinematic rupture properties of great-sized earthquakes since 1990. Earth Planet. Sci. Lett. 468, 94–100.
- Hayes, D.E., Lewis, S.D., 1984. A geophysical study of the manila trench, luzon, Philippines: 1. Crustal structure, gravity, and regional tectonic evolution. J. Geophys. Res. Solid Earth 89 (B11), 9171–9195.
- Heaton, T.H., Kanamori, H., 1984. Seismic potential associated with subduction in the northwestern United States. Bull. Seismol. Soc. Am. 74 (3), 933–941.
- Heidarzadeh, M., Satake, K., 2015. New insights into the source of the makran tsunami of 27 november 1945 from tsunami waveforms and coastal deformation data. Pure Appl. Geophys. 172 (3), 621–640.

Heidarzadeh, M., Satake, K., 2017. A combined earthquake-landslide source model for the tsunami from the 27 november 1945 m w 8.1 makran earthquake. Bull. Seismol. Soc. Am. 107 (2), 1033–1040.

- Heidarzadeh, M., Pirooz, M.D., Zaker, N.H., Yalciner, A.C., Mokhtari, M., Esmaeily, A., 2008. Historical tsunami in the makran subduction zone off the southern coasts of iran and pakistan and results of numerical modeling. Ocean Eng. 35 (8–9), 774–786.
- Heinrich, P., Schindele, F., Guibourg, S., Ihmle, P.F., 1998. Modeling of the february 1996 peruvian tsunami. Geophys. Res. Lett. 25 (14), 2687–2690.
- Herman, M.W., Furlong, K.P., 2021. Triggering an unexpected earthquake in an uncoupled subduction zone. Sci. Adv. 7 (13), eabf7590 https://doi.org/10.1126/ sciady.abf7590
- Hill, E.M., et al., 2012. The 2010 M w 7.8 Mentawai earthquake: Very shallow source of a rare tsunami earthquake determined from tsunami field survey and near-field GPS data. J. Geophys. Res. 117 (B6), B06,402 https://doi.org/10.1029/2012JB009159.
- Hirono, T., et al., 2008. Clay mineral reactions caused by frictional heating during an earthquake: an example from the Taiwan Chelungpu fault. Geophys. Res. Lett. 35 (16), L16,303 https://doi.org/10.1029/2008GL034476.
- Hoechner, A., Babeyko, A.Y., Zamora, N., 2016. Probabilistic tsunami hazard assessment for the makran region with focus on maximum magnitude assumption. Nat. Hazards Earth Syst. Sci. 16 (6), 1339–1350.
- Hsu, Y.-J., Simons, M., Avouac, J.-P., Galetzka, J., Sieh, K., Chlieh, M., Natawidjaja, D., Prawirodirdjo, L., Bock, Y., 2006. Frictional afterslip following the 2005 niassimeulue earthquake, sumatra. Science 312 (5782), 1921–1926.
- Hsu, Y.-J., Yu, S.-B., Song, T.-R.A., Bacolcol, T., 2012. Plate coupling along the manila subduction zone between Taiwan and northern luzon. J. Asian Earth Sci. 51, 98–108.
- Hsu, Y.-J., Yu, S.-B., Loveless, J.P., Bacolcol, T., Solidum, R., Luis Jr., A., Pelicano, A., Woessner, J., 2016. Interseismic deformation and moment deficit along the manila subduction zone and the philippine fault system. J. Geophys. Res. Solid Earth 121 (10), 7639–7665.
- Huang, Z., Wu, T.-R., Tan, S.K., Megawati, K., Shaw, F., Liu, X., Pan, T.-C., 2009.
 Tsunami hazard from the subduction megathrust of the South China Sea: part ii.
 Hydrodynamic modeling and possible impact on singapore. J. Asian Earth Sci. 36 (1), 93–97.
- Hubbard, J., Barbot, S., Hill, E.M., Tapponnier, P., 2015. Coseismic Slip on Shallow Décollement Megathrusts: Implications for Seismic and Tsunami Hazard. https://doi.org/10.1016/j.earscirev.2014.11.003.
- von Huene, R., Kulm, L., Miller, J., 1985. Structure of the frontal part of the andean convergent margin. J. Geophys. Res. Solid Earth 90 (B7), 5429–5442.
- von Huene, R., Ranero, C.R., Scholl, D.W., 2009. Convergent margin structure in high-quality geophysical images and current kinematic and dynamic models. In: Subduction Zone Geodynamics. Springer, pp. 137–157.
- von Huene, R., Miller, J.J., Klaeschen, D., Dartnell, P., 2016. A possible source mechanism of the 1946 unimak alaska far-field tsunami: uplift of the mid-slope terrace above a Splay Fault Zone. Pure Appl. Geophys. 173 (12), 4189–4201. https://doi.org/10.1007/s00024-016-1393-x.
- von Huene, R., Miller, J.J., Krabbenhoeft, A., 2021. The Alaska convergent margin backstop splay fault zone, a potential large tsunami generator between the frontal prism and continental framework. Geochem. Geophys. Geosyst. 22 (1), e2019GC008,901 https://doi.org/10.1029/2019GC008901.
- Hüpers, A., et al., 2017. Release of mineral-bound water prior to subduction tied to shallow seismogenic slip off Sumatra. Science 356 (6340), 841–844. https://doi.org/ 10.1126/science.aal3429.
- Hyndman, R.D., Yamano, M., Oleskevich, D.A., 1997. The seismogenic zone of subduction thrust faults. Island Arc 6 (3), 244–260.
- Ide, S., Imamura, F., Yoshida, Y., Abe, K., 1993. Source characteristics of the nicaraguan tsunami earthquake of september 2, 1992. Geophys. Res. Lett. 20 (9), 863–866.
- Ihmle, P.F., Gomez, J.-M., Heinrich, P., Guibourg, S., 1998. The 1996 Peru tsunamigenic earthquake: Broadband source process. Geophys. Res. Lett. 25 (14), 2691–2694. https://doi.org/10.1029/98GL01987.
- Ikari, M.J., Kopf, A.J., 2017. Seismic potential of weak, near-surface faults revealed at plate tectonic slip rates. Sci. Adv. 3 (11), e1701,269 https://doi.org/10.1126/ sciadv.1701269.
- Ishikawa, T., et al., 2008. Coseismic fluid-rock interactions at high temperatures in the Chelungpu fault. Nat. Geosci. 1 (10), 679–683. https://doi.org/10.1038/ngeo308.
- Ito, Y., Obara, K., 2006. Very low frequency earthquakes within accretionary prisms are very low stress-drop earthquakes. Geophys. Res. Lett. 33 (9), L09,302 https://doi. org/10.1029/2006GL025883.
- Ito, T., et al., 2009. Crustal structure of Southwest Japan, revealed by the integrated seismic experiment Southwest Japan 2002. Tectonophysics 472 (1-4), 124-134.
- Ito, Y., Tsuji, T., Osada, Y., Kido, M., Inazu, D., Hayashi, Y., Tsushima, H., Hino, R., Fujimoto, H., 2011. Frontal wedge deformation near the source region of the 2011 Tohoku-Oki earthquake. Geophys. Res. Lett. 38 (15) https://doi.org/10.1029/2011GI.048355.
- Johnson, J.M., Satake, K., 1997. Estimation of seismic moment and slip distribution of the april 1, 1946, aleutian tsunami earthquake. J. Geophys. Res. Solid Earth 102 (B6), 11,765–11,774.
- Kamei, R., Pratt, R.G., Tsuji, T., 2012. Waveform tomography imaging of a megasplay fault system in the seismogenic Nankai subduction zone. Earth Planet. Sci. Lett. 317-318, 343–353. https://doi.org/10.1016/j.epsl.2011.10.042.
- Kanamori, H., 1972. Mechanism of tsunami earthquakes. Phys. Earth Planet. Inter. 6 (5), 346–359. https://doi.org/10.1016/0031-9201(72)90058-1.
- Kanamori, H., Anderson, D.L., 1975. Theoretical basis of some empirical relations in seismology. Bull. Seismol. Soc. Am. 65 (5), 1073–1095.
- Kanamori, H., Kikuchi, M., 1993. The 1992 Nicaragua earthquake: a slow tsunami earthquake associated with subducted sediments. Nature 361 (6414), 714–716. https://doi.org/10.1038/361714a0.

Kanamori, H., Rivera, L., Lee, W.H., 2010. Historical seismograms for unravelling a mysterious earthquake: the 1907 Sumatra earthquake. Geophys. J. Int. 183 (1), 259, 274

- Kido, M., Osada, Y., Fujimoto, H., Hino, R., Ito, Y., 2011. Trench-normal variation in observed seafloor displacements associated with the 2011 Tohoku-Oki earthquake. Geophys. Res. Lett. 38 (24) https://doi.org/10.1029/2011GL050057.
- Kimura, G., Kitamura, Y., Hashimoto, Y., Yamaguchi, A., Shibata, T., Ujiie, K., Okamoto, S., 2007. Transition of accretionary wedge structures around the up-dip limit of the seismogenic subduction zone. Earth Planet. Sci. Lett. 255 (3–4), 471.484
- Kirkpatrick, J.D., Fagereng, A., Shelly, D.R., 2021. Geological constraints on the mechanisms of slow earthquakes. Nat. Rev. Earth Environ. 1–17. https://doi.org/ 10.1038/s43017-021-00148-w.
- Klaeschen, D., Belykh, I., Gnibidenko, H., Patrikeyev, S., von Huene, R., 1994. Structure of the kuril trench from seismic reflection records. J. Geophys. Res. Solid Earth 99 (B12), 24,173–24,188.
- Kodaira, S., Takahashi, N., Park, J.-O., Mochizuki, K., Shinohara, M., Kimura, S., 2000. Western Nankai Trough seismogenic zone: results from a wide-angle ocean bottom seismic survey. J. Geophys. Res. Solid Earth 105 (B3), 5887–5905. https://doi.org/ 10.1097/1906/b00304
- Kodaira, S., No, T., Nakamura, Y., Fujiwara, T., Kaiho, Y., Miura, S., Takahashi, N., Kaneda, Y., Taira, A., 2012. Coseismic fault rupture at the trench axis during the 2011 Tohoku-oki earthquake. Nat. Geosci. 5 (9), 646. https://doi.org/10.1038/ngeo1547
- Kodaira, S., Nakamura, Y., Yamamoto, Y., Obana, K., Fujie, G., No, T., Kaiho, Y., Sato, T., Miura, S., 2017. Depth-varying structural characters in the rupture zone of the 2011 Tohoku-oki earthquake. Geosphere 13 (5), 1408–1424. https://doi.org/10.1130/ GFS01489.1.
- Koketsu, K., Hikima, K., Miyazaki, S., Ide, S., 2004. Joint inversion of strong motion and geodetic data for the source process of the 2003 tokachi-oki, Hokkaido, earthquake. Earth Planets Space 56 (3), 329–334.
- Kopp, H., 2002. Crustal structure of the Java margin from seismic wide-angle and multichannel reflection data. J. Geophys. Res. 107 (B2) https://doi.org/10.1029/ 2000ib000095. ETG 1-1.
- Kopp, H., Hindle, D., Klaeschen, D., Oncken, O., Reichert, C., Scholl, D., 2009. Anatomy of the western Java plate interface from depth-migrated seismic images. Earth Planet. Sci. Lett. 288 (3–4), 399–407. https://doi.org/10.1016/j.epsl.2009.09.043.
- Kozdon, J.E., Dunham, E.M., 2014. Constraining shallow slip and tsunami excitation in megathrust ruptures using seismic and ocean acoustic waves recorded on oceanbottom sensor networks. Earth Planet. Sci. Lett. 396, 56–65.
- Kumagai, H., 1996. Time sequence and the recurrence models for large earthquakes along the nankai trough revisited. Geophys. Res. Lett. 23 (10), 1139–1142. https://doi.org/10.1029/96GL01037.
- Lay, T., Kanamori, H., 2011. Insights from the great 2011 Japan earthquake. Phys. Today 64 (12), 33–39. https://doi.org/10.1063/PT.3.1361.
- Lay, T., et al., 2005. The Great Sumatra-Andaman Earthquake of 26 December 2004. https://doi.org/10.1126/science.1112250.
- Lay, T., Ammon, C.J., Kanamori, H., Xue, L., Kim, M.J., 2011a. Possible large near-trench slip during the 2011 mw 9.0 off the pacific coast of tohoku earthquake. Earth Planets Space 63 (7), 32.
- Lay, T., Ammon, C.J., Kanamori, H., Yamazaki, Y., Cheung, K.F., Hutko, A.R., 2011b. The 25 October 2010 Mentawai tsunami earthquake (Mw 7.8) and the tsunami hazard presented by shallow megathrust ruptures. Geophys. Res. Lett. 38 (6) https://doi. org/10.1029/2010GL046552.
- Lay, T., Kanamori, H., Ammon, C.J., Koper, K.D., Hutko, A.R., Ye, L., Yue, H., Rushing, T. M., 2012. Depth-varying rupture properties of subduction zone megathrust faults. J. Geophys. Res. Solid Earth 117 (4), 1–21. https://doi.org/10.1029/2011JB009133.
- Leggett, J., Aoki, Y., Toba, T., 1985. Transition from frontal accretion to underplating in a part of the Nankai Trough Accretionary complex off Shikoku (SW Japan) and extensional features on the lower trench slope. Mar. Pet. Geol. 2 (2), 131–141. https://doi.org/10.1016/0264-8172(85)90003-0.
- Li, S., Freymueller, J.T., 2018. Spatial variation of slip behavior beneath the Alaska peninsula along Alaska-aleutian subduction zone. Geophys. Res. Lett. 45 (8), 3453–3460. https://doi.org/10.1002/2017GL076761.
- Li, J., Shillington, D.J., Becel, A., Nedimovíc, M.R., Webb, S.C., Saffer, D.M., Keranen, K. M., Kuehn, H., 2015. Downdip variations in seismic reflection character: implications for fault structure and seismogenic behavior in the Alaska subduction zone. J. Geophys. Res. Solid Earth 120 (11), 7883–7904.
- Li, L., Cheung, K.F., Yue, H., Lay, T., Bai, Y., 2016. Effects of dispersion in tsunami green's functions and implications for joint inversion with seismic and geodetic data: a case study of the 2010 mentawai mw 7.8 earthquake. Geophys. Res. Lett. 43 (21), 11–182
- Li, H., Yuan, Y., Xu, Z., Wang, Z., Wang, J., Wang, P., Gao, Y., Hou, J., Shan, D., 2018a. The dependency of probabilistic tsunami hazard assessment on magnitude limits of seismic sources in the south china sea and adjoining basins. In: Earthquakes and Multi-hazards around the Pacific Rim, vol. I. Springer, pp. 157–176.
- Li, L., Switzer, A.D., Wang, Y., Chan, C.-H., Qiu, Q., Weiss, R., 2018b. A modest 0.5-m rise in sea level will double the tsunami hazard in macau. Sci. Adv. 4 (8), eaat1180.
- Lieser, K., Grevemeyer, I., Lange, D., Flueh, E., Tilmann, F., Contreras-Reyes, E., 2014.
 Splay fault activity revealed by aftershocks of the 2010 mw 8.8 Maule earthquake,
 Central Chile. Geology 42 (9), 823–826.
- Lin, A.T., Yao, B., Hsu, S.-K., Liu, C.-S., Huang, C.-Y., 2009. Tectonic features of the incipient arc-continent collision zone of Taiwan: implications for seismicity. Tectonophysics 479 (1–2), 28–42.

- Lin, Y., Jolivet, R., Simons, M., Agram, P., Martens, H.R., Li, Z., Lodi, S., 2015. High interseismic coupling in the eastern makran (Pakistan) subduction zone. Earth Planet. Sci. Lett. 420, 116–126.
- Lockridge, P., 1985. Tsunamis-scourge of the pacific. Earthq. Inform. Bull. (USGS) 17 (6), 211–217.
- Lotto, G.C., Nava, G., Dunham, E.M., 2017. Should tsunami simulations include a nonzero initial horizontal velocity? Earth Planets Space 69 (1), 117. https://doi.org/ 10.1186/c40623.017.0701-8
- Luo, H., Wang, K., 2021. Postseismic geodetic signature of cold forearc mantle in subduction zones. Nat. Geosci. 14 (2), 104–109. https://doi.org/10.1038/s41561-020.00679.9
- Lüschen, E., Müller, C., Kopp, H., Engels, M., Lutz, R., Planert, L., Shulgin, A., Djajadihardja, Y.S., 2011. Structure, evolution and tectonic activity of the eastern Sunda forearc, Indonesia, from marine seismic investigations. Tectonophysics 508 (1–4), 6–21. https://doi.org/10.1016/j.tecto.2010.06.008.
- Ma, S., Hirakawa, E.T., 2013. Dynamic wedge failure reveals anomalous energy radiation of shallow subduction earthquakes. Earth Planet. Sci. Lett. 375, 113–122.
- Ma, S., Nie, S., 2019. Dynamic wedge failure and along-arc variations of tsunamigenesis in the Japan trench margin. Geophys. Res. Lett. 46 (15), 8782–8790. https://doi. org/10.1029/2019GL083148.
- Mandal, N., Chattopadhyay, A., Bose, S., 1997. Imbricate thrust spacing: experimental and theoretical analyses. In: Evolution of Geological Structures in Micro-to Macro-Scales. Springer, pp. 143–165.
- Maramai, A., Tinti, S., 1997. The 3 june 1994 java tsunami: A post-event survey of the coastal effects. Nat. Hazards 15 (1), 31–49.
- Martin, S.S., Li, L., Okal, E.A., Morin, J., Tetteroo, A.E., Switzer, A.D., Sieh, K.E., 2019. Reassessment of the 1907 Sumatra "Tsunami Earthquake" based on Macroseismic, Seismological, and Tsunami Observations, and Modeling. Pure Appl. Geophys. 176 (7), 2831–2868. https://doi.org/10.1007/s00024-019-02134-2.
- McCann, W., Nishenko, S., Sykes, L., Krause, J., 1979. Seismic gaps and plate tectonics: Seismic potential for major boundaries. In: Earthquake Prediction and Seismicity Patterns. Springer, pp. 1082–1147.
- McIntosh, K.D., Silver, E.A., Ahmed, I., Berhorst, A., Ranero, C.R., Kelly, R.K., Flueh, E., 2007. The Nicaragua Convergent Margin: Seismic Reflection Imaging of the Source of a Tsunami Earthquake.
- Melnick, D., Moreno, M., Motagh, M., Cisternas, M., Wesson, R.L., 2012. Splay fault slip during the mw 8.8 2010 Maule Chile earthquake. Geology 40 (3), 251–254.
- Miller, J., von Huene, R., Ryan, H., 2014. USGS Open-File Report 2014–1024: The 1946
 Unimak Tsunami Earthquake Area: Revised Tectonic Structure in Reprocessed
 Seismic Images and a Suspect Near-Field Tsunami Source.
- Miura, S., Takahashi, N., Nakanishi, A., Tsuru, T., Kodaira, S., Kaneda, Y., 2005. Structural characteristics off Miyagi forearc region, the Japan Trench seismogenic zone, deduced from a wide-angle reflection and refraction study. Tectonophysics 407 (3-4), 165–188. https://doi.org/10.1016/j.tecto.2005.08.001.
- Moore, G.F., Curray, J.R., 1980. Structure of the Sunda Trench lower slope off Sumatra from multichannel seismic reflection data. Mar. Geophys. Res. 4 (3), 319–340. https://doi.org/10.1007/BF00369106.
- Moore, G.F., Shipley, T., Stoffa, P., Karig, D., Taira, A., Kuramoto, S., Tokuyama, H., Suyehiro, K., 1990. Structure of the nankai trough accretionary zone from multichannel seismic reflection data. J. Geophys. Res. 95 (B6), 8753–8765.
- Moore, G.F., Bangs, N.L., Taira, A., Kuramoto, S., Pangborn, E., Tobin, H.J., 2007. Three-dimensional splay fault geometry and implications for tsunami generation. Science 318 (5853), 1128–1131. https://doi.org/10.1126/science.1147195.
- Moreno, M., Rosenau, M., Oncken, O., 2010. 2010 Maule earthquake slip correlates with pre-seismic locking of Andean subduction zone. Nature 467 (7312), 198–202. https://doi.org/10.1038/nature09349.
- Mountjoy, J.J., Barnes, P.M., 2011. Active upper plate thrust faulting in regions of low plate interface coupling, repeated slow slip events, and coastal uplift: Example from the Hikurangi Margin, New Zealand. Geochem. Geophys. Geosyst. 12 (1) https://doi. org/10.1029/2010GC003326.
- Nakamura, Y., Kodaira, S., Miura, S., Regalla, C., Takahashi, N., 2013. High-resolution seismic imaging in the Japan Trench axis area off Miyagi, northeastern Japan. Geophys. Res. Lett. 40 (9), 1713–1718. https://doi.org/10.1002/grl.50364.
- Nakano, M., et al., 2018. The 2016 Mw 5.9 earthquake off the southeastern coast of Mie Pre- fecture as an indicator of preparatory processes of the next Nankai Trough megathrust earthquake. Progr. Earth Planet. Sci. 5 (1), 30. https://doi.org/10.1186/ s40645-018-0188-3.
- Nanjundiah, P., Barbot, S., Wei, S., 2020. Static source properties of slow and fast earthquakes. J. Geophys. Res. 125 (12), e2019JB019,028 https://doi.org/10.1029/ 2019JB019028
- Natawidjaja, D.H., Sieh, K., Chlieh, M., Galetzka, J., Suwargadi, B.W., Cheng, H., Edwards, R.L., Avouac, J.-P., Ward, S.N., 2006. Source parameters of the great Sumatran megathrust earthquakes of 1797 and 1833 inferred from coral microatolls. J. Geophys. Res. 111 (B6), B06,403 https://doi.org/10.1029/2005JB004025.
- Nguyen, P.H., Bui, Q.C., Vu, P.H., Pham, T.T., 2014. Scenario-based tsunami hazard assessment for the coast of Vietnam from the manila trench source. Phys. Earth Planet. Inter. 236, 95–108.
- Nicol, A., Beavan, J., 2003. Shortening of an overriding plate and its implications for slip on a subduction thrust, central Hikurangi Margin, New Zealand. Tectonics 22 (6). https://doi.org/10.1029/2003TC001521.
- Noda, H., Lapusta, N., 2013. Stable creeping fault segments can become destructive as a result of dynamic weakening. Nature 493 (7433), 518–521. https://doi.org/ 10.1038/nature11703.
- Obana, K., Kodaira, S., 2009. Low-frequency tremors associated with reverse faults in a shallow accretionary prism. Earth Planet. Sci. Lett. 287 (1–2), 168–174. https://doi.org/10.1016/j.epsl.2009.08.005.

Obara, K., Kato, A., 2016. Connecting slow earthquakes to huge earthquakes. Science 353 (6296), 253–257. https://doi.org/10.1126/science.aaf1512.

- Okamura, Y., Tsujino, T., Arai, K., Sasaki, T., Satake, K., Joshima, M., 2008. Fore arc structure and plate boundary earthquake sources along the southwestern Kuril subduction zone. J. Geophys. Res. 113 (B6), B06,305 https://doi.org/10.1029/2007.JB005246.
- Park, J.-O., Tsuru, T., Kodaira, S., Nakanishi, A., Miura, S., Kaneda, Y., Kono, Y., Takahashi, N., 2000. Out-of-sequence thrust faults developed in the coseismic slip zone of the 1946 Nankai earthquake (Mw= 8.2) off Shikoku, Southwest Japan. Geophys. Res. Lett. 27 (7), 1033–1036.
- Park, J.O., Tsuru, T., Kodaira, S., Cummins, P.R., Kaneda, Y., 2002. Splay fault branching along the Nankai subduction zone. Science 297 (5584), 1157–1160. https://doi.org/ 10.1126/science.1074111.
- Pasyanos, M.E., Masters, T.G., Laske, G., Ma, Z., 2014. LITHO1. 0: an updated crust and lithospheric model of the Earth. J. Geophys. Res. 119 (3), 2153–2173. https://doi.org/10.1002/2013JB010626.
- Penney, C., et al., 2017. Megathrust and accretionary wedge properties and behaviour in the makran subduction zone. Geophys. J. Int. 209 (3), 1800–1830.
- Piatanesi, A., Tinti, S., Gavagni, I., 1996. The slip distribution of the 1992 Nicaragua earthquake from tsunami run-up data. Geophys. Res. Lett. 23 (1), 37–40.
- Polet, J., Kanamori, H., 2000. Shallow subduction zone earthquakes and their tsunamigenic potential. Geophys. J. Int. 142 (3), 684–702. https://doi.org/10.1046/j.1365-246X.2000.00205.x.
- Qin, Y., Singh, S.C., 2018. Insight into frontal seismogenic zone in the mentawai locked region from seismic full waveform inversion of ultralong offset streamer data. Geochem. Geophys. Geosyst. 19 (11), 4342–4365.
- Qiu, Q., Moore, J.D.P., Barbot, S., Feng, L., Hill, E., 2018. Transient viscosity in the sumatran mantle wedge from a decade of geodetic observations. Nat. Commun. 9 (995) https://doi.org/10.1038/s41467-018-03298-6.
- Qiu, Q., Feng, L., Hermawan, I., Hill, E.M., 2019a. Coseismic and postseismic slip of the 2005 Mw 8.6 Nias-Simeulue earthquake: spatial overlap and localized viscoelastic flow. J. Geophys. Res. Solid Earth 124 (7), 7445–7460. https://doi.org/10.1029/ 2018JB017263.
- Qiu, Q., Li, L., Hsu, Y.-J., Wang, Y., Chan, C.-H., Switzer, A.D., 2019b. Revised earthquake sources along manila trench for tsunami hazard assessment in the South China Sea. Nat. Hazards Earth Syst. Sci. 19 (7), 1565–1583.
- Ramos, N.T., Maxwell, K.V., Tsutsumi, H., Chou, Y.-G., Duan, F., Shen, C.-G., Satake, K., 2017. Occurrence of 1 ka-old corals on an uplifted reef terrace in west luzon, Philippines: Implications for a prehistoric extreme wave event in the South China Sea region. Geosci. Lett. 4 (1), 1–13.
- Ranero, C.R., von Huene, R., 2000. Subduction erosion along the Middle America convergent margin. Nature 404 (6779), 748–752. https://doi.org/10.1038/ 35008046
- Rashidi, A., Shomali, Z.H., Dutykh, D., Farajkhah, N.K., 2020. Tsunami hazard assessment in the makran subduction zone. Nat. Hazards 100 (2), 861–875.
- Rice, J.R., 2006. Heating and weakening of faults during earthquake slip. J. Geophys. Res. Solid Earth 111 (5). https://doi.org/10.1029/2005JB004006.
- Ryan, W.B., et al., 2009. Global multi-resolution topography synthesis. Geochem. Geophys. Geosyst. 10 (3).
- Saffer, D.M., Wallace, L.M., 2015. The frictional, hydrologic, metamorphic and thermal habitat of shallow slow earthquakes. Nat. Geosci. 8 (8), 594–600.
- Sallares, V., Ranero, C.R., 2019. Upper-plate rigidity determines depth-varying rupture behaviour of megathrust earthquakes. Nature 576 (7785), 96–101. https://doi.org/ 10.1038/s41586-019-1784-0.
- Sallares, V., Melendez, A., Prada, M., Ranero, C.R., McIntosh, K., Grevemeyer, I., 2013. Overriding plate structure of the Nicaragua convergent margin: relationship to the seismogenic zone of the 1992 tsunami earthquake. Geochem. Geophys. Geosyst. 14 (9), 3436–3461. https://doi.org/10.1002/ggge.20214.
- Satake, K., 1994. Mechanism of the 1992 Nicaragua tsunami earthquake. Geophys. Res. Lett. 21 (23), 2519–2522.
- Satake, K., Tanioka, Y., 1999. Sources of tsunami and tsunamigenic earthquakes in subduction zones. Pure Appl. Geophys. 154 (3–4), 467–483. https://doi.org/ 10.1007/s000240050240.
- Satake, K., Wang, K., Atwater, B.F., 2003. Fault slip and seismic moment of the 1700 cascadia earthquake inferred from japanese tsunami descriptions. J. Geophys. Res. Solid Earth 108 (B11).
- Satake, K., Fujii, Y., Yamaki, S., 2017. Different Depths of near-Trench Slips of the 1896 Sanriku and 2011 Tohoku Earthquakes. https://doi.org/10.1186/s40562-017-0099-
- Sathiakumar, S., Barbot, S.D., Agram, P., 2017. Extending resolution of fault slip with geodetic networks through optimal network design. J. Geophys. Res. 122 (12) https://doi.org/10.1002/2017JB014326.
- Sathiakumar, S., Barbot, S., Hubbard, J., 2020. Seismic cycles in fault-bend folds.
 J. Geophys. Res. 125 (8), e2019JB018,557 https://doi.org/10.1029/2019JB018557.
- Schlüter, H., Prexl, A., Gaedicke, C., Roeser, H., Reichert, C., Meyer, H., Von Daniels, C., 2002. The makran accretionary wedge: sediment thicknesses and ages and the origin of mud volcanoes. Mar. Geol. 185 (3–4), 219–232.
- Scholl, D.W., Kirby, S.H., von Huene, R., Ryan, H., Wells, R.E., Geist, E.L., 2015. Great (Mw8.0) megathrust earthquakes and the subduction of excess sediment and bathymetrically smooth seafl oor. Geosphere 11 (2), 236–265. https://doi.org/10.1130/ GES01079.1.
- Scholz, C.H., 1998. Earthquakes and friction laws. Nature 391, 37–42. https://doi.org/ 10.1038/34097.
- Seno, T., 2000. The 21 September, 1999 Chi-Chi earthquake in Taiwan: implications for Tsunami earthquakes. Terr. Atmos. Ocean. Sci. 11 (3), 701–708. https://doi.org/ 10.3319/TAO.2000.11.3.701(CCE).

- Seno, T., 2017. Subducted sediment thickness and mw 9 earthquakes. J. Geophys. Res. Solid Earth 122 (1), 470-491.
- Shi, Q., Barbot, S., Wei, S., Tapponnier, P., Matsuzawa, T., Shibazaki, B., 2020. Structural control and system-level behavior of the seismic cycle at the Nankai Trough. Earth Planets Space 72 (1), 343–353. https://doi.org/10.1186/s40623-020-1145-0.
- Sibson, R.H., 1977. Kinetic shear resistance, fluid pressures and radiation efficiency during seismic faulting. Pure Appl. Geophys. 115 (1–2), 387–400. https://doi.org/ 10.1007/BF01637116.
- Sieh, K., et al., 2008. Earthquake supercycles inferred from sea-level changes recorded in the corals of West Sumatra. Science 322 (5908), 1674–1678.
- Simons, M., et al., 2011. The 2011 magnitude 9.0 Tohoku-Oki earthquake: mosaicking the megathrust from seconds to centuries. Science 332 (6036), 1421–1425. https:// doi.org/10.1126/science.1206731.
- Singh, S.C., et al., 2008. Seismic evidence for broken oceanic crust in the 2004 Sumatra earthquake epicentral region. Nat. Geosci. 1 (11), 777–781. https://doi.org/ 10.1038/ngeo336.
- Sladen, A., Trevisan, J., 2018. Shallow megathrust earthquake ruptures betrayed by their outer-trench aftershocks signature. Earth Planet. Sci. Lett. 483, 105–113.
- Smith, G., McNeill, L., Henstock, T.J., Bull, J., 2012. The structure and fault activity of the makran accretionary prism. J. Geophys. Res. Solid Earth 117 (B7).
- Smith, G.L., McNeill, L.C., Wang, K., He, J., Henstock, T.J., 2013. Thermal structure and megathrust seismogenic potential of the makran subduction zone. Geophys. Res. Lett. 40 (8), 1528–1533.
- Song, T.-R.A., Simons, M., 2003. Large trench-parallel gravity variations predict seismogenic behavior in subduction zones. Science 301 (5633), 630–633. https:// doi.org/10.1126/science.1085557.
- Strasser, M., et al., 2013. A slump in the trench: Tracking the impact of the 2011 tohokuoki earthquake. Geology 41 (8), 935–938.
- Suleimani, E., Freymueller, J.T., 2020. Near-field modeling of the 1964 alaska tsunami: the role of splay faults and horizontal displacements. J. Geophys. Res. Solid Earth 125 (7), e2020JB019.620.
- Suleimani, E., Ruppert, N., Fisher, M., West, D., Hansen, R., 2008. The contribution of coseismic displacements due to splay faults into the local wavefield of the 1964 alaska tsunami. In: AGUFM, 2008. OS43D–1334.
- Sultan, M., Ahmed, K., 2017. Statistical analysis of earthquakes and tsunami of makran subduction zone (msz), and tsunami hazard assessment of Gwadar coast. J. Earth Sci. Clim. Change 8 (408), 2.
- Sun, L., et al., 2013. Preliminary evidence for a 1000-year-old tsunami in the South China Sea. Sci. Rep. 3 (1), 1–5.
- Takahashi, N., Kodaira, S., Park, J.-O., Diebold, J., 2003. Heterogeneous structure of western nankai seismogenic zone deduced by multichannel reflection data and wideangle seismic data. Tectonophysics 364 (3–4), 167–190.
- Tanaka, H., Chen, W.M., Wang, C.Y., Ma, K.F., Urata, N., Mori, J., Ando, M., 2006.
 Frictional heat from faulting of the 1999 Chi-Chi, Taiwan earthquake. Geophys. Res.
 Lett. 33 (16), L16,316 https://doi.org/10.1029/2006GL026673.
- Tanioka, Y., Sataka, K., 1996. Fault parameters of the 1896 sanriku tsunami earthquake estimated from tsunami numerical modeling. Geophys. Res. Lett. 23 (13), 1549–1552
- Tanioka, Y., Seno, T., 2001. Sediment effect on tsunami generation of the 1896 sanriku tsunami earthquake. Geophys. Res. Lett. 28 (17), 3389–3392.
- Thatcher, W., 1989. Earthquake recurrence and risk assessment in circum-pacific seismic gaps. Nature 341 (6241), 432–434.
- Todd, E.K., et al., 2018. Earthquakes and tremor linked to seamount subduction during shallow slow slip at the hikurangi margin, New Zealand. J. Geophys. Res. Solid Earth 123 (8), 6769–6783.
- Tsang, L.L.H., Hill, E.M., Barbot, S., Qiu, Q., Feng, L., Hermawan, I., Banerjee, P., Natawidjaja, D.H., 2016. Afterslip following the 2007 Mw 8.4 Bengkulu earthquake in Sumatra loaded the 2010 Mw 7.8 Mentawai tsunami earthquake rupture zone. J. Geophys. Res. Solid Earth 121, 9034–9049. https://doi.org/10.1002/2016.fB013432.
- Tsuji, T., Kawamura, K., Kanamatsu, T., Kasaya, T., Fujikura, K., Ito, Y., Tsuru, T., Kinoshita, M., 2013. Extension of continental crust by anelastic deformation during the 2011 Tohoku-oki earthquake: the role of extensional faulting in the generation of a great tsunami. Earth Planet. Sci. Lett. 364, 44–58. https://doi.org/10.1016/j.epsl.2012.12.038.
- Tsuji, T., Ashi, J., Strasser, M., Kimura, G., 2015. Identification of the static backstop and its influence on the evolution of the accretionary prism in the nankai trough. Earth Planet. Sci. Lett. 431, 15–25.
- Tsuru, T., Park, J.-O., Miura, S., Kodaira, S., Kido, Y., Hayashi, T., 2002. Along-arc structural variation of the plate boundary at the Japan trench margin: Implication of interplate coupling. J. Geophys. Res. Solid Earth 107 (B12). ESE–11.
- Tsutsumi, A., Fabbri, O., Karpoff, A.M., Ujiie, K., Tsujimoto, A., 2011. Friction velocity dependence of clay-rich fault material along a megasplay fault in the nankai subduction zone at intermediate to high velocities. Geophys. Res. Lett. 38 (19) https://doi.org/10.1029/2011GL049314.
- Ujiie, K., Tsutsumi, A., 2010. High-velocity frictional properties of clay-rich fault gouge in a megasplay fault zone, nankai subduction zone. Geophys. Res. Lett. 37 (24) https://doi.org/10.1029/2010GL046002.
- UTSU, T., 1994. Aftershock Activity of the 1896 Sanriku Earthquake, vol. 47(1), pp. 89–92.
- Wada, I., Wang, K., 2009. Common depth of slab-mantle decoupling: Reconciling diversity and uniformity of subduction zones. Geochem. Geophys. Geosyst. 10 (10) https://doi.org/10.1029/2009GC002570.
- Wallace, L.M., et al., 2009. Characterizing the seismogenic zone of a major plate boundary subduction thrust: Hikurangi Margin, New Zealand. Geochem. Geophys. Geosyst. 10 (10) https://doi.org/10.1029/2009GC002610.

- Wallace, L.M., Webb, S.C., Ito, Y., Mochizuki, K., Hino, R., Henrys, S., Schwartz, S.Y., Sheehan, A.F., 2016. Slow slip near the trench at the hikurangi subduction zone, New Zealand. Science 352 (6286), 701–704.
- Wang, K., Bilek, S.L., 2011. Do subducting seamounts generate or stop large earthquakes? Geology 39 (9), 819–822. https://doi.org/10.1130/G31856.1.
- Wang, K., Hu, Y., 2006. Accretionary prisms in subduction earthquake cycles: the theory of dynamic Coulomb wedge. J. Geophys. Res. Solid Earth 111 (B6). https://doi.org/ 10.1029/2005JB004094.
- Wang, K., He, J., Hu, Y., 2006. A note on pore fluid pressure ratios in the Coulomb wedge theory. Geophys. Res. Lett. 33 (19), L19,310 https://doi.org/10.1029/ 2006GL027233.
- Wang, K., Hu, Y., von Huene, R., Kukowski, N., 2010. Interplate earthquakes as a driver of shallow subduction erosion. Geology 38 (5), 431–434.
- Ward, S.N., 2001. Landslide tsunami. J. Geophys. Res. Solid Earth 106 (B6), 11.201–11.215.
- Watt, J.T., Brothers, D.S., 2020. Systematic characterization of morphotectonic variability along the cascadia convergent margin: Implications for shallow megathrust behavior and tsunami hazards. Geosphere 17 (1), 95–117. https://doi. org/10.1130/GES02178.1
- Wei, S., Graves, R., Helmberger, D., Avouac, J.-P., Jiang, J., 2012. Sources of shaking and flooding during the Tohoku-Oki earthquake: a mixture of rupture styles. Earth Planet. Sci. Lett. 333–334, 91–100. https://doi.org/10.1016/j.epsl.2012.04.006.

- Weiss, J.R., et al., 2019. Illuminating subduction zone rheological properties in the wake of a giant earthquake. Sci. Adv. https://doi.org/10.1126/sciadv.aax6720.
- Whittaker, J.M., Goncharov, A., Williams, S.E., Müller, R.D., Leitchenkov, G., 2013. Global sediment thickness data set updated for the Australian-Antarctic Southern Ocean. Geochem. Geophys. Geosyst. 14 (8), 3297–3305. https://doi.org/10.1002/ ggge_20181.
- Wibberley, C.A., Shimamoto, T., 2005. Earthquake slip weakening and asperities explained by thermal pressurization. Nature 436 (7051), 689–692.
- Witter, R.C., Zhang, Y.J., Wang, K., Priest, G.R., Goldfinger, C., Stimely, L., English, J.T., Ferro, P.A., 2013. Simulated tsunami inundation for a range of cascadia megathrust earthquake scenarios at Bandon, Oregon, USA. Geosphere 9 (6), 1783–1803.
- Yang, W., et al., 2018. Nan'ao, an archaeological site of song dynasty destroyed by tsunami. Chin. Sci. Bull. 64 (1), 107–120.
- Yu, K.-F., Zhao, J.-X., Shi, Q., Meng, Q.-S., 2009. Reconstruction of storm/tsunami records over the last 4000 years using transported coral blocks and lagoon sediments in the southern South China Sea. Quat. Int. 195 (1–2), 128–137.
- Yue, H., et al., 2014. Rupture process of the 2010 M_w 7.8 Mentawai tsunami earthquake from joint inversion of near-field hr-GPS and teleseismic body wave recordings constrained by tsunami observations. J. Geophys. Res. Solid Earth 119 (7), 5574–5593. https://doi.org/10.1002/2014JB011082.
- Zhu, J., Sun, Z., Kopp, H., Qiu, X., Xu, H., Li, S., Zhan, W., 2013. Segmentation of the manila subduction system from migrated multichannel seismics and wedge taper analysis. Mar. Geophys. Res. 34 (3), 379–391.